Luttinger liquid on a lattice
Zakharov, V.

Luttinger liquid on a lattice

Proefschrift

ter verkrijging van
de graad van doctor aan de Universiteit Leiden,
op gezag van rector magnificus prof.dr.ir. H. Bijl,
volgens besluit van het college voor promoties
te verdedigen op dinsdag 23 September 2025
klokke 10.00 uur

door

Vladimir Aleksandrovich Zakharov
geboren te Sint-Petersburg, Rusland
in 1997

Cover:
You see water – a universal metaphor for the physics of collective behavior presented in this thesis. Water is a liquid, a state of matter where interactions play a crucial role. The surface of water serves as a good example of a disordered landscape shaped by external random forces. Finally, this landscape naturally contains many different peaks and valleys, as well as various types of saddle points connecting them.
Cover design: Maria Zakharova, original photograph: Vladimir Zakharov.

To my mother
Моей маме

Contents

Chapter 1

Introduction

1.1 Preface

One of the difficult problems in condensed matter physics is treating systems with interactions. An interaction in a Hamiltonian is typically represented by terms that are non-quadratic in quasi-particle creation and annihilation operators. Standard methods based on solving the eigenvalue equation for a single particle then do not apply. The problem becomes intrinsically many-body and must be solved in the full Fock space. The size of the Fock space grows exponentially with the size of the physical system, and quite quickly the problem becomes unsolvable via a direct approach. This obstruction represents the main difficulty in solving many-body physics.

Nevertheless, the development of theoretical physics has produced several ways to deal with the problem of interactions [1]. One of the most well-known theories in this regard is the theory of the Landau liquid [2], whose essential idea is the concept of a quasiparticle. In many materials, the effect of interactions can be efficiently described as a "dressing" of the electron in a cloud of other electrons with which it interacts. The cloud changes the characteristics of the particle, such as its mass or velocity, and gives it a finite lifetime. But ultimately, the quasiparticle can still be described as a free particle.

As famous as the concept of the Fermi liquid is, equally well-known is the fact that it breaks down in one spatial dimension. In 1D, physics can no longer be described with the quasiparticle picture and becomes necessarily strongly correlated. This is why the 1D theory of interacting electrons requires a special name. It is known as the Luttinger or Tomonaga–Luttinger liquid [3, 4]. Despite being truly a many-body problem, the Luttinger liquid is, in the simplest case of
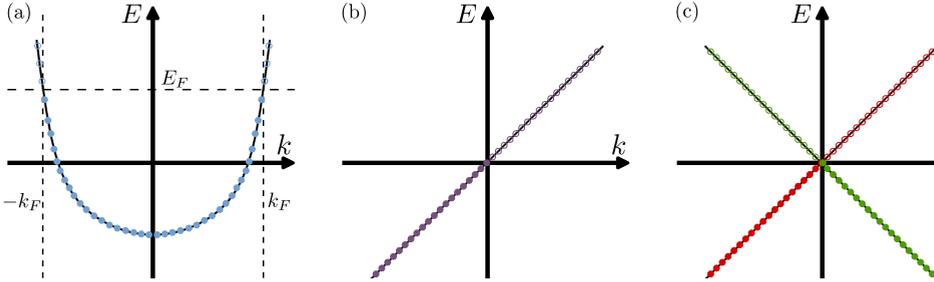
Figure 1.1. Dispersion of one-dimensional electrons for (a) topologically non-protected Luttinger liquid, (b) chiral Luttinger liquid, and (c) helical Luttinger liquid. For (b) and (c) we assume $E_F = 0$ and $k_F = 0$. Filled (empty) circles represent occupied (non-occupied) electron states.

on-site interactions, fully solvable via the bosonization technique. This technique, however, has its limits and cannot solve all variations of the problem — for example, more complicated interactions or the presence of disorder make the problem analytically unsolvable again. Therefore, one would like to have a numerical method capable of describing the physics of such systems.

At the same time, numerical methods for solving Luttinger liquid theory are complicated because of the Nielsen–Ninomiya theorem [5], which prohibits a straightforward discrete formulation of the problem.

These last two facts — the necessity of a numerical method and the simultaneous difficulty of creating one — are the main motivations for the major topic of this thesis. In the remainder of the introduction, I will formally define the Luttinger liquid and describe its main characteristics, as well as introduce the concept of the bosonization technique and briefly describe the lattice formulation of the problem and the no-go theorem.

1.2   Topologically protected Luttinger liquid

The standard image of a Luttinger liquid dispersion, i.e., the non-interacting part of the energy, is presented in Figure 1.1. Panel (a) represents a generic band with finite filling, far from the ends of the band. In one spatial dimension, such a band has two points where the Fermi energy E_F crosses the dispersion. In the vicinity of these crossings, one may approximate the dispersion as

$$E(k) \approx \pm v_F(\hat{k} \pm k_F) + E_F. \tag{1.1}$$

Calling the corresponding eigen-wavefunctions Ψ_R and Ψ_L, and making a matching transformation $\hat{k} \rightarrow \hat{k} \mp k_F$, one defines an effective one-dimensional problem of an electron with a quasi-spin:

$$H\Psi = E\Psi, \quad H = v_F \sigma_z \hat{k}. \tag{1.2}$$

This Hamiltonian describes a gapless (metallic) system in one dimension. But the gaplessness in this picture is not protected and results from fine-tuning. Since both Ψ_R and Ψ_L come from the same electronic band, nothing prevents a generic term in the initial Hamiltonian that would couple the k_F and $-k_F$ points — for instance, a random disorder. Coupling of these two points is a backscattering process that introduces an effective mass term $m\sigma_x$ to the Hamiltonian (1.2) and opens a gap in the spectrum.

To protect the metallic behavior, one needs to rely on topological protection. In other words, the quasi-spin of the electron must be a symmetry-protected quantum number. One such system is a chiral fermion with a dispersion shown in Figure 1.1 (b). In one dimension chiral fermion is defined by its velocity direction, it is strictly a right- or left-mover. The absence of a counter-propagating electron makes backscattering impossible and therefore topologically guarantees gaplessness. A one-dimensional interacting system with a single chiral electron mode is then called a chiral Luttinger liquid, whose Hamiltonian in the non-interacting limit is simply

$$H = v_F \hat{k}. \tag{1.3}$$

Obviously, adding any number of additional fermions with the same chirality cannot open a gap either, since backscattering remains impossible. A physical example of such a system in condensed matter is the edge of a quantum Hall system [6], schematically represented in Figure 1.2 (a), which is topologically equivalent to a one-dimensional ring with all electrons being chiral right- or left-movers.

Moreover, one may also include pairs of different fermions with opposite chiralities without spoiling the metallic behavior, as long as their chirality is protected. The minimal example of one right- and one left-mover is shown in Figure 1.1 (c) and described by the same Hamiltonian as in (1.2), but now with chirality as a well-defined quantum number fixed by the band. The absence of a backscattering process is typically guaranteed by time-reversal (TR) symmetry: the Hamiltonian must be invariant under the transformation $(\sigma, \hat{k}) \rightarrow (-\sigma, -\hat{k})$. This model is called a helical Luttinger liquid and is physically realized at the edge of a quantum spin Hall insulator [7, 8], illustrated in Figure 1.2 (b).
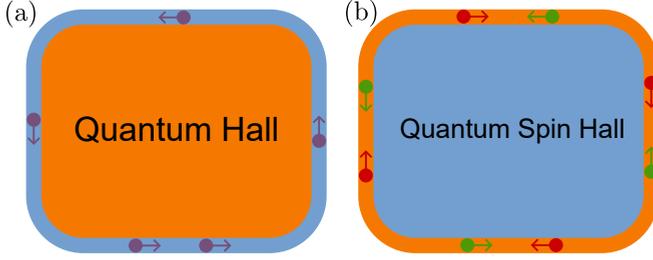
Figure 1.2. Schematic representation of (a) a Quantum Hall insulator and (b) a Quantum Spin Hall insulator. Both systems are insulating in the bulk and have conducting edges. Propagating electrons, represented by dots at the boundaries, are chiral; their velocity, illustrated by small arrow-vectors, is determined either by (a) the topology of the system or by (b) their (quasi-)spin depicted by different colors. The edges are quasi-one-dimensional, conducting, and topologically protected, and therefore represent a physical realization of a Luttinger liquid system.

Platforms that experimentally realize the physics of chiral or helical Luttinger liquids include the topological states of matter mentioned above, as well as composite systems such as Josephson junction chains and cold atoms [9].

1.3   Chiral fermions in QFT and SPT

Although the title of this thesis is "Luttinger liquid on a lattice," and most chapters focus on the specific example of a helical Luttinger liquid, the key ingredient in that physical picture is the concept of a one-dimensional chiral fermion, as discussed in Section 1.2. This concept plays a crucial role both in quantum field theories in (1+1)D and in symmetry-protected topological (SPT) phases of matter in 2D. Accordingly, the numerical methods developed in this thesis are also highly relevant to these broader areas. In this section, I briefly describe how the concept of chiral fermions arises in QFT and SPT phases.

Fermions in quantum field theory are spinors described by the Dirac equation,

$$S = \int d^2x \overline{\psi} \left(i\gamma^0 \partial_t + i\gamma^1 \partial_x + m \right) \psi, \tag{1.4}$$

where $\overline{\psi} = \psi^\dagger \gamma^0$, and the gamma matrices $\gamma^0 = \sigma_x$, $\gamma^1 = i\sigma_y$ satisfy the Clifford algebra $\{\gamma^\mu, \gamma^\nu\} = 2\eta^{\mu\nu}$ with $\eta^{\mu\nu} = \text{diag}(1, -1)$. When the fermion is massless ($m = 0$), the action simplifies to

$$S = \int d^2x i\psi^\dagger \left(\partial_t - \gamma^5 \partial_x \right) \psi, \tag{1.5}$$

where $\gamma^5 = -\gamma^0\gamma^1 = \sigma_z$. In this form, the massless Dirac fermion decouples into two independent chiral components $\psi_\pm = \frac{1}{2}(1 \pm \gamma^5)\psi$. Thus, the original vector ($\psi \to e^{i\alpha}\psi$) and axial ($\psi \to e^{i\alpha\gamma^5}\psi$) symmetries of the theory become two independent chiral symmetries: $\psi_\pm \to e^{i\alpha_\pm}\psi_\pm$.

An SPT phase of matter [10] is a type of topological insulator (TI), characterized by a gapped bulk and a gapless, symmetry-protected edge. In this sense, a quasi-1D edge of a 2D TI provides a natural platform to realize Luttinger liquid physics. TIs can exhibit either short-range or long-range entanglement. Here, we focus on short-range entangled TIs, known as SPT phases, which, in contrast to long-range entangled TIs, do not support intrinsic topological order such as fractional statistics (as seen, for instance, in the fractional quantum Hall effect).

SPT phases generalize the notion of topological band insulators (TBIs) to include interactions. Hence, examples like the integer quantum Hall state and the quantum spin Hall state discussed in the previous section are both fermionic SPT phases in two dimensions. Further, fermionic SPT phases include many-body interacting states that cannot be realized within a free-particle picture [11]. The boundaries of these more exotic phases can often be described by multicomponent Luttinger liquid theories [12].

1.4 Bosonization

The fundamental features of Luttinger liquid physics can be captured analytically using the method of bosonization [13]. Here we consider a helical system on a ring of length L, with the dispersion shown in Fig. 1.1(c), described by the Hamiltonian

$$H = \int_{-L/2}^{L/2} dx : \left[\psi_\uparrow^\dagger(-iv_F\partial_x)\psi_\uparrow - \psi_\downarrow^\dagger(-iv_F\partial_x)\psi_\downarrow + g_1\hat{\rho}_\uparrow(x)\hat{\rho}_\downarrow(x) + g_2\left(\hat{\rho}_\uparrow^2(x) + \hat{\rho}_\downarrow^2(x)\right)\right]:,$$

(1.6)

where $\psi_\sigma = \frac{1}{\sqrt{L}}\sum_k e^{-ikx}c_{k,\sigma}$ and $\rho_\sigma = \psi_\sigma^\dagger\psi_\sigma$. The terms with coefficients g_1 and g_2 represent density-density interactions between opposite and same chirality, respectively. Colons denote normal ordering. In this regime, the model becomes analytically solvable in the bosonic representation [14]. In this section I briefly describe how to do it.

We construct bosonic operators as bilinears of fermionic operators:

$$b_{q\sigma} = -\frac{i}{\sqrt{n_q}} \sum_k c^\dagger_{k-q,\sigma} c_{k,\sigma}, \quad q = \frac{2\pi}{L} \sigma n_q, \quad n_q > 0,$$

$$\phi_\sigma(x) = -\sum_{n_q} \frac{1}{\sqrt{n_q}} \left[e^{-iqx} b_{q\sigma} e^{-a\sigma q/2} + e^{iqx} b^\dagger_{q\sigma} e^{-a\sigma q/2} \right]. \tag{1.7}$$

where $b_{q\sigma}$ is a bosonic annihilation operator and $\phi_\sigma(x)$ is the bosonic field. The ultraviolet regularization parameter a is introduced to control divergences of the theory.

Now the fermionic fields and densities can now be expressed in terms of $\phi_\sigma(x)$ via the famous bosonization transformation:

$$\rho_\sigma(x) = \frac{1}{L} \hat{N}_\sigma + \frac{\sigma}{2\pi} \partial_x \phi_\sigma(x), \tag{1.8}$$

$$\psi(x)_\sigma = \frac{1}{\sqrt{2\pi a}} F_\sigma e^{-i\sigma \frac{2\pi}{L}(\hat{N}_\sigma - [1-\delta_b]/2)x} e^{-i\phi_\sigma(x)}. \tag{1.9}$$

Here, since by the construction the bosonic operators can not measure the total amount of fermions in the system, we introduced $\hat{N}_\sigma$ as the total number of electrons counted from the half-filling point. Correspondingly we define the $|N_\sigma\rangle$ states as the ground states of the non-interacting Hamiltonian with fixed amount of electrons. In other words $|N_\uparrow\rangle$ is a state with all $\left|(k < -\frac{2\pi n}{L}, \sigma = \uparrow)\right\rangle$ filled and respectively $|N_\downarrow\rangle$ is a state with all $\left|(k > \frac{2\pi n}{L}, \sigma = \downarrow)\right\rangle$ filled. Obviously the eigenvalue relation $\hat{N}_\sigma |N_\sigma\rangle = N_\sigma$ holds. Additionally, to be able to switch between different $|N_\sigma\rangle$ states, and to satisfy the fermionic statistic the Klein factors F_σ are being introduced as

$$F_\sigma |N_\sigma\rangle = T_\sigma |N_\sigma - 1\rangle, \quad T_\downarrow = (-1)^{N_\uparrow}, \quad T_\uparrow = 1. \tag{1.10}$$

Substituting the bosonization relation (1.8) into Eq. (1.6), the Hamiltonian becomes [14]

$$H = \frac{\pi v}{L} \left[\sum_\sigma (\frac{1}{g} + g) \left(\frac{1}{2} \hat{N}_\sigma^2 + \sum_{n_q} n_q b^\dagger_{q\sigma} b_{q\sigma} \right) \right.$$

$$\left. + (\frac{1}{g} - g) \left(\hat{N}_\uparrow \hat{N}_\downarrow - \sum_{n_q} n_q \left[b^\dagger_{q\uparrow} b^\dagger_{q\downarrow} + b_{q\uparrow} b_{q\downarrow} \right] \right) \right] + \delta_b \sum_\sigma \frac{\pi v_F}{L} N_\sigma, \tag{1.11}$$

where the renormalized velocity v and dimensionless electron-electron interaction parameter g ($g = 1$ for the free case) are given by

$$v = v_F \sqrt{\left(1 + \frac{g_2}{\pi v_F}\right)^2 - \frac{g_1^2}{4\pi^2 v_F^2}}, \quad g = \sqrt{\frac{v_F + g_2/\pi - g_1/(2\pi)}{v_F + g_2/\pi + g_1/(2\pi)}}. \qquad (1.12)$$

In Eq.(1.11) the term with coefficient $(\frac{1}{g} + g)$ corresponds to the kinematic part of the initial Hamiltonian, the $(\frac{1}{g} - g)$ term comes from the interacting part, and the last term originates from the finite size formulation with $\delta_b = 1$ for periodic boundary conditions and $\delta_b = 0$ if it is antiperiodic.

Finally, the beauty of the bosonization idea becomes visible: the interaction terms, originally quartic in the fermionic formulation, become quadratic in the bosonic representation. This bosonic Hamiltonian can be diagonalized via a Bogoliubov transformation:

$$B_{q\pm} = \frac{1}{\sqrt{8}} \left[\left(\frac{1}{\sqrt{g}} + \sqrt{g}\right) (b_{q\uparrow} \mp b_{q\downarrow}) \pm \left(\frac{1}{\sqrt{g}} - \sqrt{g}\right) (b_{q\uparrow}^\dagger \mp b_{q\downarrow}^\dagger) \right],$$

$$H = \frac{2\pi v}{L} \sum_\sigma \sum_{n_q} n_q B_{q\sigma}^\dagger B_{q\sigma} + \sum_\sigma \frac{\pi v_F}{L} N_\sigma \left[N_\sigma + \delta_b\right] + \frac{g_1}{L} N_\uparrow N_\downarrow + \sum_\sigma \frac{g_2}{L} N_\sigma^2.$$

$$(1.13)$$

Thus, the Luttinger liquid model defined in Eq. (1.6) is solved analytically. With access to the full eigenspectrum and eigenfunctions, one can compute various observables such as Green's functions or spin correlators, which exhibit power-law behavior characteristic of gapless one-dimensional systems. In Chapter 2, we calculate these correlators, carefully taking finite-size and finite-temperature effects into account, to compare the analytical predictions with our numerical simulations.

1.5 Lattice formulation and no-go theorem

In the previous sections, we described the fundamentals of the helical Luttinger liquid and showed that, in its simplest form, it is fully analytically solvable. Bosonization is a powerful tool that provides deep insights into the physics of chiral fermions in one dimension. Nevertheless, not all scenarios can be solved analytically. Breaking translational symmetry, via disorder or scalar potentials, or introducing more complex interactions, such as spatially dependent terms or higher-order fermionic operators, makes the model analytically intractable.
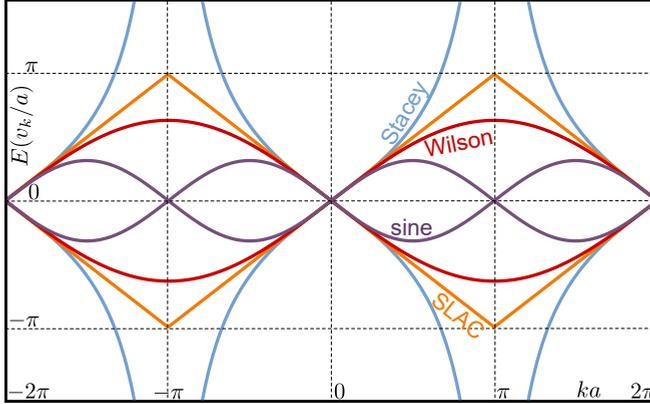
Figure 1.3. Dispersion relations of free electrons resulting from different discretization schemes of the Dirac Hamiltonian in one dimension, shown over two Brillouin zones. Only the Stacey derivative simultaneously preserves chiral symmetry, avoids doublers, and supports efficient numerical simulations due to hidden locality.

Therefore, one would like to simulate Luttinger liquid physics *in silico*, ideally in a numerically efficient manner. Or, in other words, to put the *Luttinger liquid on a lattice*. However, one immediately encounters the nontrivial problem of discretizing the momentum operator:

$$\hat{k} = -i\partial_x. \tag{1.14}$$

This obstacle is known as the fermion-doubling problem, formalized in the no-go theorem by Nielsen and Ninomiya [5]:

Any hermitian and local in real space Hamiltonian
that preserves the chirality of the Dirac fermions
must have an even number of left- and right-movers in the Brillouin zone.

Here we illustrate this phenomenon (see also Fig. 1.3) with several examples that implement different discretization schemes of the Dirac Hamiltonian:

$$H_D = -iv_F\sigma_z\partial_x = v_F\sigma_z\hat{k}. \tag{1.15}$$

Sine derivative

The most straightforward discretization of the derivative is the central finite difference:

$$\partial_x f(x) \rightarrow (2a)^{-1}(f(x+a) - f(x-a)). \tag{1.16}$$

In momentum space, this leads to a sine dispersion:

$$H_D \rightarrow H_{sin} = v_F/a\sigma_z \sin(\hat{k}a). \tag{1.17}$$

This formulation is local and chiral symmetric ($H_{sin} \propto \sigma_z$), but, consistent with the no-go theorem, it results in a doubler with opposite chirality at the Brillouin zone (BZ) edge (see Figure 1.3). As discussed in Section 1.2, the presence of doublers results in the theory unstable to disorder or generic inter-cone coupling, making it incapable for simulating Luttinger liquid physics.

Wilson derivative

To resolve the doubling problem in Eq. (1.17), one can add a momentum-dependent mass term to gap out the unwanted cone:

$$H_D \rightarrow H_{Wilson} = v_F/a \left[\sigma_z \sin(\hat{k}a) + \left(1 - \cos(\hat{k}a)\right)\sigma_x\right]. \tag{1.18}$$

This formulation of discretized Dirac Hamiltonian has a name of Wilson fermion. Certainly it is still local ($\cos(\hat{k}a)$ is a sparce matrix in real space) and eliminates the doubler. However, it explicitly breaks chirality by introducing a σ_x mass term that mixes the chiralities, violating a key assumption of the Nielsen-Ninomiya theorem. This term needs to be fine-tuned in order to vanish at $k = 0$ and therefore it is unstable to disorder. Furthermore, it reintroduces chirality mixing away from $k = 0$ (see how at Figure 1.3 dispersions of left- and right-mover of Wilson discretization smoothly merge at the edge of the BZ), resulting in backscattering and undermining the chiral nature of the system.

SLAC derivative

From the previous schemes, we see that either explicit chirality breaking (Wilson) or the presence of doublers (sine) obstructs the topological protection of the chiral fermion on a lattice. Therefore the only remaining assumption of the no-go theorem that can be relaxed is the locality of the derivative operator in real space. One of the formulation exploiting this idea is called SLAC derivative

$$\partial_x f(x) \rightarrow \sum_{n=1}^{\infty} (-1)^n (an)^{-1} (f(x + na) - f(x - na)). \tag{1.19}$$

As depicted at the Figure 1.3 it produces a Hamiltonian that is strictly linear in momentum

$$H_D \rightarrow H_{SLAC} = v_F/(ia)\sigma_z \ln e^{i\hat{k}a}. \tag{1.20}$$

Ultimately, SLAC lattice formulation produces a strictly chiral fermion without a doubler by the cost of being non-local, making it a reasonable candidate for simulating chiral physics. However, attempts of reproducing the Luttinger liquid behavior within SLAC framework seem to fail [15] presumably due to the utter non-locality of SLAC fermion.

Stacey derivative

An alternative non-local discretization is provided by the Stacey derivative [16]:

$$\partial_x f(x) \to 2(a)^{-1} \sum_{n=1}^{\infty} (-1)^n (f(x + na) - f(x - na)). \qquad (1.21)$$

This leads to the tangent dispersion (see Figure 1.3) in momentum space:

$$H_D \to H_{tan} = 2v_F/a\sigma_z \tan\left(\hat{k}a/2\right). \qquad (1.22)$$

This discretization scheme, called the *tangent fermion* [17], plays a central role in this thesis and lays in the foundation of the numerical methods developed herein.

Tangent fermion is highly non-local in its' original formulation. Namely, Eq. (1.21) contains all-to-all hoppings of the same, not-decaying amplitude. Remarkably, tangent fermion, as it explained in the Chapter 3, possess hidden locality, which allows for various efficient local formulations. Furthermore, it accomplishes the task of reproducing Luttinger liquid physics faithfully, a success we attribute to its' unique combination of chirality preservation and hidden locality.

1.5.1   Domain wall fermion

Finally it is worth to mention here another approach to circumvent the fermion doubling. It has the name of domain wall fermion and exploits the idea of reproducing the physics of one-dimensional chiral fermions as the edge state of a two-dimensional topological system, thereby lifting the dimensionality of the system from 1D to 2D. While being rigorous, this formulation is consequentially more demanding numerically since one needs to simulate a system of a greater dimensionality. Further, it introduces an unavoidable bulk-edge coupling, which compromises the intrinsic one-dimensional character of the model.

1.6 This thesis

During my PhD journey I encountered and worked on several different topics in theory of condensed matter. The physics of strongly correlated chiral fermions in one dimension became the main focus of my PhD, two chapters of this thesis represent it. In Chapter 2 we implement the idea of tangent fermions to simulate the helical Luttinger liquid using quantum Monte Carlo (QMC) approach, and then we extend the idea further to tensor network methods in Chapter 3. The remaining two chapters of this thesis focus on two-dimensional single-particle physics. In Chapter 4 we study the Majorana metal transition as a percolation of topological edge modes. Finally, Chapter 5 investigates the phenomenon of Landau quantization in systems with generalized Van Hove singularities. Below, I summarize the main results of each chapter.

1.6.1 Chapter 2

In this chapter we tackle the significant challenge in simulating strongly correlated one-dimensional systems for the first time. We choose helical Luttinger liquid as a test ground, an ideal candidate to do the benchmark of our method due to its analytical solvability. We introduce a novel approach using tangent fermions on a space-time lattice. This method possess the hidden locality that makes numerical simulations feasible, while preserving the chirality of the fermions and removing the doublers. Namely the approach has a local Euclidean action formulation which is applicable in Quantum Monte Carlo (QMC) simulations.
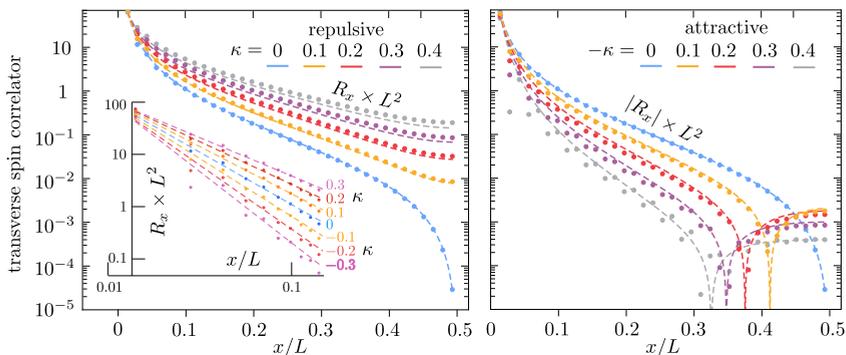
Figure 1.4. Quantum Monte Carlo results (data points) for the spin correlator of a helical Luttinger liquid on a space-time lattice, showing excellent agreement with analytical bosonization theory (dashed curves) for both repulsive and attractive interactions. This validates the tangent fermion approach for simulating correlated systems.

Crucially, our fermionic auxiliary-field QMC simulations for the helical Luttinger liquid at half-filling are shown to be sign-problem-free, a common challenge in fermionic simulations. The results from our simulations accurately reproduce the expected Luttinger liquid continuum physics without needing any adjustable parameters. We validate our findings by comparing them with analytical bosonization theory, even deriving finite-size and finite-temperature corrections for precise comparisons. This work represents a significant step as the first successful lattice simulation of the helical Luttinger liquid.

1.6.2 Chapter 3

Following the successful validation of the tangent fermion approach using QMC in Chapter 2, this chapter pushes the boundaries further by employing powerful tensor network methods, specifically the Density Matrix Renormalization Group (DMRG). While QMC proved the concept, it was limited by the sign problem to specific conditions like helical systems at half-filling without external potentials. Tensor networks offer a way to overcome these limitations.

We demonstrate that the hidden locality inherent in the tangent fermion formulation allows for an efficient representation using tensor networks. This finding, coupled with the non-locality required by the Nielsen-Ninomiya theorem to avoid fermion doubling and the necessity of preserving well-defined chirality, provides strong support for the uniqueness of the tangent fermion approach.
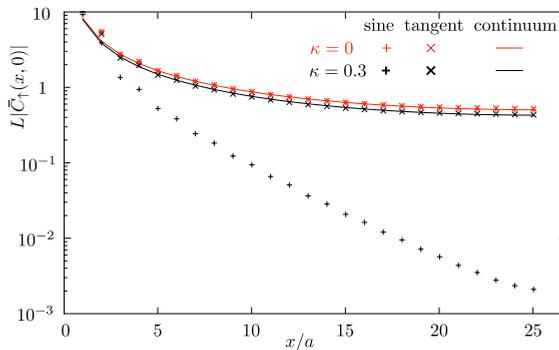
Figure 1.5. Absolute value of the propagator calculated using tensor networks for the tangent (dots) and sine (plusses) discretizations of the Luttinger Hamiltonian. The tangent discretization agrees well with the continuum analytical results (curves), while the sine discretization shows an unphysical gap. This highlights the advantage of the tangent fermion approach.

Using DMRG, we achieve excellent agreement between our results and

bosonization theory. We also perform a critical comparison with a straight-forward sine discretization formulation, which, in contrast, results in a gapped spectrum, highlighting the instability of lattice formulations burdened by fermion doublers. This work establishes tensor networks as a viable and versatile tool for simulating strongly correlated chiral fermions on a lattice using the tangent fermion framework.

1.6.3 Chapter 4

This chapter delves into the behavior of disordered chiral p-wave superconductors, a type of topological material classified by the Chern number. While conventional superconductors are typically thermal insulators, disorder can transform these topological superconductors into a thermal metal phase, where heat is transported by Majorana fermions. The transition to this Majorana metal phase has been observed in computer simulations but not yet experimentally.
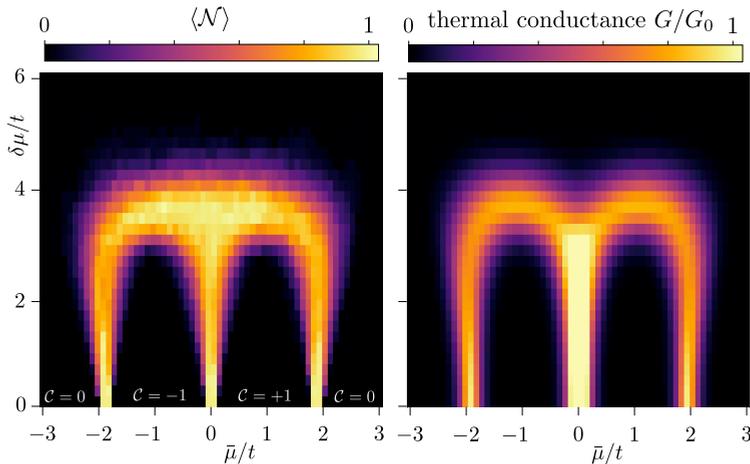
Figure 1.6. Left panel shows the average number of percolating domain walls as a function of disorder parameters, clearly distinguishing the region where the Majorana metal phase emerges. Right panel shows the corresponding thermal conductance, confirming the transition. This demonstrates that the thermal metal-insulator transition is driven by the percolation of topological domain walls.

Our research provides compelling numerical evidence that this thermal metal – insulator transition occurs via the percolation of boundaries separating regions with different topological properties (specifically, different Chern numbers). In a clean system, the Chern number is uniform, making the bulk insulating. How-

ever, disorder creates a "topological landscape" of domains with varying Chern numbers.

To study this process in real space, we employ the innovative concept of the spectral localizer, which acts as a "topological landscape function" capable of determining local Chern numbers. This allows us to visualize the formation of a network of domain walls between these topologically distinct domains. As disorder increases, these domains grow and eventually connect, forming a percolating cluster that spans the system, providing a channel for Majorana fermions and enabling thermal conduction. By analyzing this percolation transition, we successfully determine the thermal metal–insulator phase diagram.

1.6.4 Chapter 5

This chapter explores the phenomenon of magnetic breakdown in 2D materials, particularly focusing on regions with generalized Van Hove singularities (vHs). Magnetic breakdown occurs when electron trajectories in a magnetic field come close together, allowing quantum tunneling. While well-studied at usual vHs, newer 2D materials feature "high-order" vHs with flatter dispersions, leading to richer magnetic breakdown behavior and new challenges.
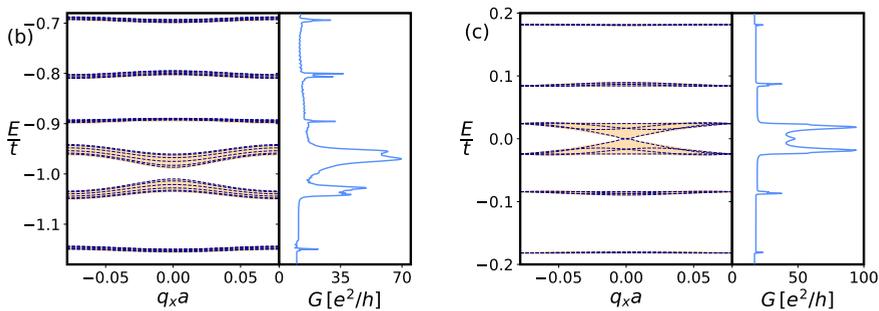
Figure 1.7. Longitudinal conductance (right panels, blue lines) calculated for finite systems with (b) square lattice and A_3 saddle point and (c) triangular lattice and Monkey saddle point, compared with the spectral structure of Landau minibands (left panels, orange solid lines (tight-binding simulations) and blue dashed lines (analytically via our approach)) arising from coherent orbit networks connected via magnetic breakdown at different types of Van Hove singularities. The conductance peaks correspond to the minibands, demonstrating the possibility of bulk conduction mediated by these networks.

We develop a general method to calculate the precise magnetic breakdown scattering matrix (s-matrix) for any type of saddle point, including these high-

order cases. Our approach maps the problem onto a 1D scattering problem in a quantum chain derived from the Landau level basis.

A key consequence of magnetic breakdown, especially when saddle points are at the edge of the Brillouin zone, is the formation of coherent orbit networks. These networks delocalize the Landau level states, forming dispersive Landau mini-bands that can support bulk electrical conduction in the presence of a magnetic field. We calculate the longitudinal bulk conductance in a quantum Hall bar geometry and show that this conduction, enabled by the orbit networks, can strongly exceed the standard edge conductance. The energy-dependent width of these mini-bands (and thus the conductance peaks) is uniquely tied to the type of vHs, offering a potential experimental signature to distinguish between different types of saddle points through conductance measurements.

Chapter 2

Helical Luttinger liquid on a space-time lattice

2.1 Introduction

A quantum spin Hall insulator [7] supports a one-dimensional (1D) helical edge mode of counterpropagating massless electrons (Dirac fermions, see Fig. 2.1), with a linear dispersion $E = \pm\hbar v_F k$. The crossing at momentum $k = 0$ (the Dirac point) is protected from gap-opening [8] — provided that there is only a single species of low-energy excitations and provided that fundamental symmetries (time-reversal symmetry, chiral symmetry) are preserved. This topological protection is broken on a lattice by fermion doubling [18]: Any local and symmetry-preserving discretization of the momentum operator $k = -i\hbar d/dx$ must introduce a spurious second Dirac point [5, 19].

Fermion doubling is problematic if one wishes to study interaction effects of 1D massless electrons (a Luttinger liquid [3, 20, 13, 21]) by means of a lattice fermion method such as quantum Monte Carlo [22, 23, 24, 25, 26]. A way to preserve the time-reversal and chiral symmetries on a lattice is to increase the
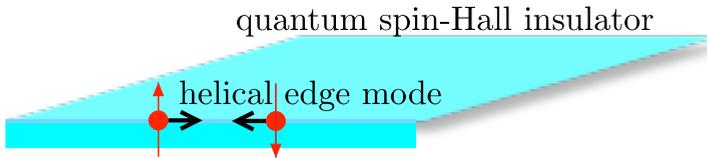
Figure 2.1. Helical edge mode, consisting of counter-propagating spin-up and spin-down electrons on the 1D boundary of a 2D quantum spin Hall insulator.

dimensionality of the system [27, 28]. One can simulate a 2D system in a ribbon geometry, so that the two fermion species are spatially separated on opposite edges [29, 30, 31, 32, 33]. The 2D simulation is computationally more expensive than a fully 1D simulation, but more fundamentally, the presence of states in the bulk may obscure the intrinsically 1D physics of a Luttinger liquid [34]. A 1D simulation using a nonlocal spatial discretization [35] that avoids fermion doubling was studied recently [15], without success: The nonlocality gaps the Dirac point [15, 36].

Here we show that it can be done: A 1D helical Luttinger liquid can be simulated on a lattice if both space *and time* are discretized in a way that preserves the locality of the Lagrangian. The time discretization (in units of τ) pushes the second Dirac point up to energies of order $\hbar/\tau$, where it does not affect the low-energy physics — as we demonstrate by comparing quantum Monte Carlo simulations with results from bosonization [20, 13, 21, 14].

The lattice fermion approach which we will now describe refers specifically to the massless Dirac fermions that appear in topological insulators. Other approaches exist that exploit the boson-fermion correspondence. One can first bosonize the fermion formulation of the problem [37] and then put it on a lattice [38]. Luttinger liquid physics may also govern the low-energy properties of bosonic systems such as spin chains [39], where fermion doubling does not apply and a lattice formulation poses no difficulties [40, 41].

2.2   Locally discretized Lagrangian

We construct the space-time lattice using the tangent fermion discretization approach [16, 42, 43, 44, 45, 17]. We first outline that approach for the noninteracting case, in a Lagrangian formulation that is a suitable starting point for the interacting problem.

Consider a 1D free massless fermion field $\psi_\sigma(x, t)$ with Lagrangian density given by

$$\mathcal{L}_{\text{continuum}} = \sum_\sigma \psi_\sigma^\dagger (i\partial_t + i\sigma v_{\text{F}}\partial_x)\psi_\sigma. \tag{2.1}$$

The spin degree of freedom σ, equal to $\uparrow\downarrow$ or ± 1, distinguishes right-movers from left-movers, both propagating with velocity v_{F} along the x-axis. We set $\hbar = 1$ and denote partial derivatives by ∂_x, ∂_t. The chemical potential is set to to zero (the Dirac point, corresponding to a half-filled band).

We discretize space x and time t, in units of a and τ, respectively. The naive discretization of space replaces $\partial_x \mapsto (2a)^{-1}(e^{a\partial_x} - e^{-a\partial_x})$, which amounts to
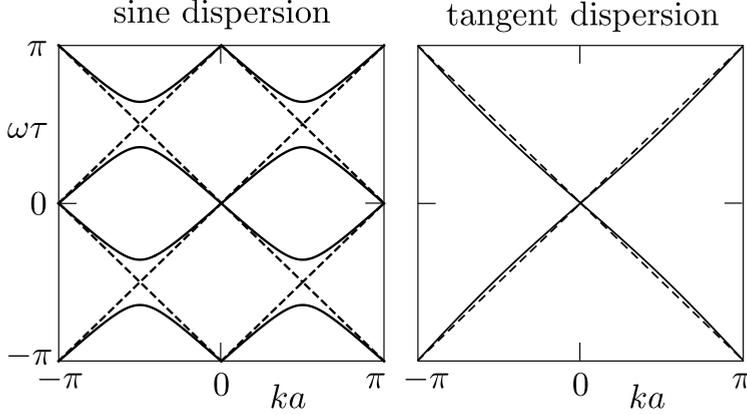
Figure 2.2. Dispersion relation of a massless fermion on a 1+1-dimensional space-time lattice. The two panels compare the sine and tangent discretization schemes, for $\gamma = v_F\tau/a$ equal to 1 (dashed curves) or 0.9 (solid curves). The sawtooth discretization has the γ-independent dispersion $\omega = \pm v_F\tau$ in the Brillouin zone $|\omega\tau|, |ka| < \pi$. Only the tangent discretization gives a local Lagrangian with a single Dirac point at $\omega = 0$.

$\partial_x f(x) \mapsto (2a)^{-1}[f(x+a) - f(x-a)]$. Similarly, $\partial_t \mapsto (2\tau)^{-1}(e^{\tau\partial_t} - e^{-\tau\partial_t})$, producing a Lagrangian with a sine kernel,

$$\mathcal{L}_{\text{sine}} = (a\tau)^{-1}\sum_\sigma \psi_\sigma^\dagger(\sin\hat{\omega}\tau - \sigma\gamma\sin\hat{k}a)\psi_\sigma. \tag{2.2}$$

We defined the frequency and momentum operators $\hat{\omega} = i\partial_t$ and $\hat{k} = -i\partial_x$ and denote $\gamma = v_F\tau/a$. The discretized ψ's are dimensionless.

The naive discretization is a local discretization, in the sense that the Lagrangian only couples nearby sites on the space-time lattice. However, it suffers from fermion doubling: The dispersion relation $\sin\omega\tau = \sigma\gamma\sin ka$ has branches of right-movers and left-movers which intersect at a Dirac point (see Fig. 2.2, left panel). Kramers degeneracy protects the crossings at time-reversally invariant points $\omega\tau, ka = 0$ modulo π. In the Brillouin zone $|ka|, |\omega\tau| < \pi$ there are 4 inequivalent Dirac points, two of which are at $\omega = 0$: one at $k = 0$, the other at $|k| = \pi$. Low-energy scattering processes can couple these two Dirac points and open a gap without violating Kramers degeneracy. To avoid this we need to ensure that there is only a single Dirac point at $\omega = 0$.

One way to remove the spurious second species of low-energy excitations goes by the name of SLAC fermions in the particle physics context [35], or Floquet fermions in the context of periodically driven atomic lattices [46, 47]. In that approach one truncates the continuum linear dispersion at the Brillouin zone

boundaries, and then repeats sawtooth-wise[1] with 2π-periodicity:

$$\mathcal{L}_{\text{sawtooth}} = -i(a\tau)^{-1}\sum_\sigma \psi_\sigma^\dagger (\ln e^{i\hat{\omega}\tau} - \sigma\gamma \ln e^{i\hat{k}a})\psi_\sigma. \qquad (2.3)$$

The sawtooth dispersion relation $\ln e^{i\omega\tau} = \sigma\gamma \ln e^{ika}$ is strictly linear in the Brillouin zone, with a single Dirac point at $\omega = 0$, however the Lagrangian is nonlocal:

$$(\ln e^{i\hat{k}a})f(x) = \sum_{n=1}^{\infty}(-1)^n n^{-1}[f(x - na) - f(x + na)], \qquad (2.4)$$

so distant points on the space-time lattice are coupled.

To obtain a local Lagrangian with a single Dirac point at $\omega = 0$ we take two steps: First we replace the sine in $\mathcal{L}_{\text{sine}}$ by a tangent with the same 2π periodicity:

$$\mathcal{L}_{\text{tangent}} = \frac{2}{a\tau}\sum_\sigma \psi_\sigma^\dagger \left[\tan(\hat{\omega}\tau/2) - \sigma\gamma \tan\left(\hat{k}a/2\right)\right]\psi_\sigma. \qquad (2.5)$$

The resulting tangent dispersion $\tan(\omega\tau/2) = \sigma\gamma \tan(ka/2)$ removes the spurious Dirac point (see Fig. 2.2, right panel), but it creates a non-local coupling. The locality is restored by the substitution

$$\psi_\sigma = \hat{D}\phi_\sigma, \quad \hat{D} = \tfrac{1}{4}(1 + e^{i\hat{k}a})(1 + e^{i\hat{\omega}\tau}), \qquad (2.6)$$

which produces the Lagrangian

$$\mathcal{L}_{\text{tangent}} = \tfrac{1}{2}(a\tau)^{-1}\sum_\sigma \phi_\sigma^\dagger \big[(1 + \cos \hat{k}a)\sin \hat{\omega}\tau$$
$$- \sigma\gamma(1 + \cos \hat{\omega}\tau)\sin \hat{k}a\big]\phi_\sigma. \qquad (2.7)$$

Product terms $\cos \hat{k}a \times \sin \hat{\omega}\tau$ and $\cos \hat{\omega}\tau \times \sin \hat{k}a$ couple $\phi_\sigma(x,t)$ to $\phi_\sigma(x \pm a, t \pm \tau)$, so the coupling is off-diagonal on the space-time lattice but local.

This recovery of a local Lagrangian from a nonlocal Hamiltonian can be understood intuitively [17]: While the tangent discretization of the differential operator is nonlocal, its functional inverse, which is the trapezoidal integration rule, is local — allowing for a local path integral formulation of the quantum dynamics.

The next step is to introduce the on-site Hubbard interaction (strength U, repulsive for $U > 0$, attractive for $U < 0$) by adding to $\mathcal{L}_{\text{tangent}}$ the term

$$\mathcal{L}_{\text{Hubbard}} = -(U/a)n_\uparrow(x,t)n_\downarrow(x,t), \quad n_\sigma = :\psi_\sigma^\dagger \psi_\sigma: \qquad (2.8)$$

---

[1]We set the branch cut of the logarithm along the negative real axis, so $\ln e^{ika}$ is a sawtooth that jumps at $ka = \pi + 2n\pi$.

The density n_σ is normal ordered (Fermi sea expectation value is subtracted). Substitution of Eq. (2.6) expresses the density n_σ at point (x,t) in terms of the average of the field ϕ_σ over the four corners of the adjacent space-time unit cell.

This completes the lattice formulation of the Luttinger liquid. We characterize it by the functions

$$C_\sigma(x) = \langle \psi_\sigma^\dagger(x,0)\psi_\sigma(0,0)\rangle, \quad \boldsymbol\psi = (\psi_\uparrow, \psi_\downarrow), \tag{2.9}$$
$$R_x(x) = \langle \rho_x(x)\rho_x(0)\rangle, \quad \rho_x(x) = \tfrac{1}{2}\boldsymbol\psi^\dagger(x,0)\sigma_x\boldsymbol\psi(x,0).$$

Here $\langle \cdots \rangle = Z^{-1}\operatorname{Tr} e^{-\beta H} \cdots$ indicates the thermal average at inverse temperature $\beta = 1/k_B T$ (with $Z = \operatorname{Tr} e^{-\beta H}$ the partition function). We first focus on the propagator C_σ.

2.3 Discretized Euclidean action

The propagator can be rewritten as a fermionic path integral [48, 1] over anticommuting fields $\Psi = \{\Psi_+, \Psi_-\}$ and $\bar\Psi = \{\bar\Psi_+, \bar\Psi_-\}$,

$$C_\sigma(x) = Z^{-1}\int \mathcal{D}\bar\Psi \int \mathcal{D}\Psi\, e^{-S[\Psi,\bar\Psi]}\bar\Psi_\sigma(x,0)\Psi_\sigma(0,0), \tag{2.10}$$

with S the Euclidean action. For free fermions one has

$$S = \int_0^\beta dt \int_0^L dx \sum_\sigma \bar\Psi_\sigma(x,t)(\partial_t - i\sigma v_F\partial_x)\Psi_\sigma(x,t). \tag{2.11}$$

The Lagrangian (2.1) is integrated along the interval $0 < it < i\beta$ on the imaginary time axis, with antiperiodic boundary conditions: $\Psi_\sigma(x,\beta) = -\Psi_\sigma(x,0)$. On the real space axis the integral runs from 0 to L with periodic boundary conditions, $\Psi_\sigma(0,t) = \Psi_\sigma(L,t)$.

The tangent fermion discretization replaces $i\partial_t \mapsto (2/\tau)\tan(\hat\omega\tau/2)$ and $i\partial_x \mapsto -(2/a)\tan(\hat k a/2)$, resulting in the discretized Euclidean action

$$\begin{aligned}
S_{\text{tangent}} &= 2\textstyle\sum_{x,t,\sigma}\bar\Psi_\sigma(x,t)\big(-i\tan(\hat\omega\tau/2) \\
&\quad + \gamma\sigma\tan\big(\hat k a/2\big)\big)\Psi_\sigma(x,t) \tag{2.12a} \\
&= \tfrac{1}{2}\textstyle\sum_{x,t,\sigma}\bar\Phi_\sigma(x,t)\big(-i(1 + \cos\hat k a)\sin\hat\omega\tau \\
&\quad + \gamma\sigma(1 + \cos\hat\omega\tau)\sin\hat k a\big)\Phi_\sigma(x,t). \tag{2.12b}
\end{aligned}$$

In the second equality we substituted the locally coupled fields, $\Psi = \hat{D}\Phi$, $\bar{\Psi} = \bar{\Phi}\hat{D}^\dagger$, cf. Eq. (2.6). The Hubbard interaction is then included by adding to $\mathcal{S}_{\text{tangent}}$ the action

$$\mathcal{S}_{\text{Hubbard}} = U\tau\sum_{x,t}\bar{\Psi}_+(x,t)\Psi_+(x,t)\bar{\Psi}_-(x,t)\Psi_-(x,t). \tag{2.13}$$

We choose discretization units τ, a so that both β/τ and L/a are integer. The space-time lattice consists of the points $it_n = in\tau$, $n = 0, 1, 2\ldots\beta/\tau - 1$, on the imaginary time axis and $x_n = na$, $n = 0, 1, 2\ldots L/a - 1$ on the real space axis. Upon Fourier transformation the sum over t_n becomes a sum over the Matsubara frequencies $\omega_n = (2n+1)\pi/\beta$, while the sum over x_n becomes a sum over the momenta $k_n = 2n\pi/L$. These are odd versus even multiples of the discretization unit, to ensure the antiperiodic versus periodic boundary conditions in t and x, respectively. In order to avoid the pole in the tangent dispersion we choose β/τ even and L/a odd.

2.4 Free-fermion propagator

Without the interaction term the propagator (2.10) is given by a Gaussian path integral [48, 1], which evaluates to

$$C_\sigma(x) = \frac{\tau}{\beta L}\sum_{k,\omega}\frac{e^{-ikx}}{2i\tan(\omega\tau/2) - 2\gamma\sigma\tan(ka/2)}. \tag{2.14}$$

A simple closed-form answer follows for the Fourier transform $C_\sigma(k)$ in the zero-temperature ($\beta \to \infty$) limit,

$$\begin{aligned}
C_\sigma(k) &= \tau\int_{-\pi/\tau}^{\pi/\tau}\frac{d\omega}{2\pi}\frac{1}{2i\tan(\omega\tau/2) - 2\gamma\sigma\tan(ka/2)} \\
&= \frac{-1}{2\,\text{sign}(\sigma\tan(ka/2)) + 2\gamma\sigma\tan(ka/2)}.
\end{aligned} \tag{2.15}$$

For the sine dispersion we have instead

$$C_\sigma(k) = \frac{-\,\text{sign}(\sigma\sin ka)}{\sqrt{1 + 4\gamma^2\sin^2 ka}}, \tag{2.16}$$

while the sawtooth dispersion gives

$$C_\sigma(k) = -\frac{1}{\pi}\arctan\left(\frac{\pi}{\gamma\sigma ka}\right), \quad |ka| < \pi. \tag{2.17}$$
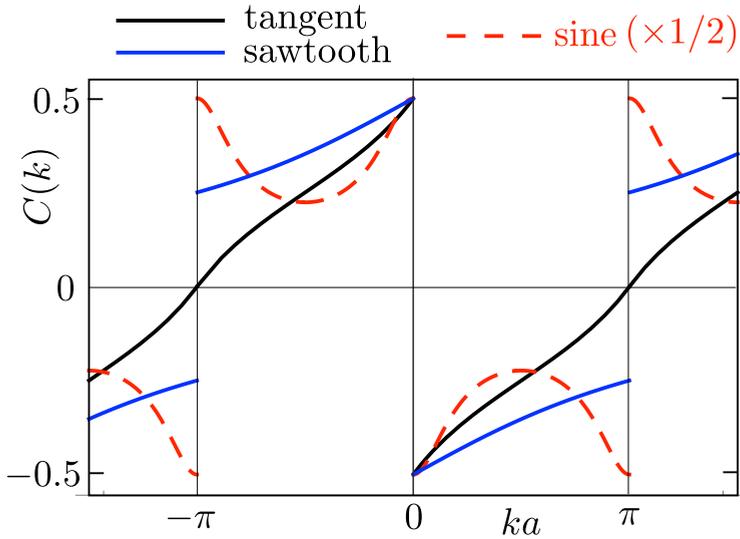
Figure 2.3. Free-fermion propagator in momentum space at zero temperature, calculated for three different discretization schemes. The plots follow from Eqs. (2.15), (2.16), and (2.17), for $\gamma = 1$, $\sigma = +1$. Only the tangent fermion discretization is continuous at the Brillouin zone boundary $ka = \pm\pi$.

Each dispersion has the expected continuum limit[2] $C_\sigma(k) \to -\frac{1}{2}\operatorname{sign}(\sigma k)$ for $|ka| \ll 1$, up to a factor of two for the sine dispersion due to fermion doubling. The difference appears near the boundary $|ka| = \pi/a$ of the Brillouin zone. As shown in Fig. 2.3, only the tangent dispersion gives a propagator that is continuous across the Brillouin zone boundary. In real space, the discontinuity shows up as an oscillation of $C_\sigma(x)$ for separations x that are even or odd multiples of a, see Fig. 2.4. This is a known artefact of a finite band width [49] which is avoided by tangent fermions: their $C_\sigma(x)$ is close to the continuum result $i/2\pi x$ for x larger than a few lattice spacings.

It is essential that the spatial discretization is accompanied by a discretization of (imaginary) time: If we would only discretize space, taking the limit $\tau \to 0$ at fixed a, then $\gamma \to 0$ and the propagator tends to the wrong limit,

$$\lim_{\tau \to 0} C_\sigma(x) = \tfrac{1}{2}i\sigma \int_0^{\pi/a} \sin kx \, dk = \frac{i\sigma \sin^2(\pi x/2a)}{\pi x}, \qquad (2.18)$$

---

[2]The continuum limit $C_\sigma(k) = -\frac{1}{2}\operatorname{sign}(\sigma k)$ differs from the zero-temperature Fermi function $\theta(-\sigma k)$ by a 1/2 offset. This offset corresponds to a delta function $\delta(x - x')$ contribution to the propagator (2.9), which is lost in the discretization.
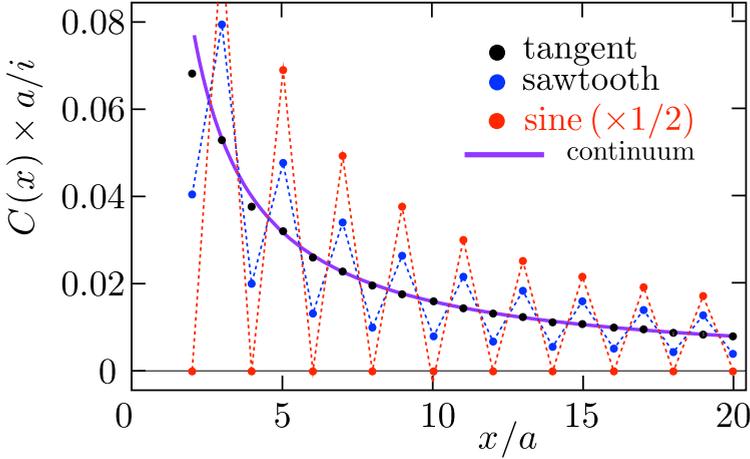
Figure 2.4. Same as Fig. 2.3, but now in real space. The continuum result at zero temperature is $C(x) = i/2\pi x$ (solid curve), close to the tangent fermion discretization (black dots). The dashed lines are guides to the eye, to highlight the oscillatory behavior of the sawtooth and sine discretizations.

irrespective of how space is discretized. This deficiency of the sawtooth (SLAC) approach was noted in Ref. [15].

   Luttinger liquid correlators – We now include the Hubbard interaction (2.13) in the discretized Euclidean action (2.12), and evaluate the path integral (2.10) numerically by the quantum Monte Carlo method [50]. In a Luttinger liquid the zero-temperature correlators decay as a power law [13],

$$C_\sigma^2 \propto x^{-K-1/K}, \quad R_x \propto x^{-2K}, \tag{2.19a}$$

$$K = \sqrt{(1-\kappa)/(1+\kappa)}, \quad \kappa = \frac{Ua}{2\pi v_F} \in (-1,1). \tag{2.19b}$$

For repulsive interactions, $U > 0 \Rightarrow K < 1$, the transverse spin-density correlator R_x decays more slowly than the $1/x^2$ decay expected from a Fermi liquid.

   Results for the interaction dependent decay are shown in Fig. 2.5. The data from the quantum Monte Carlo calculation of $R_x(x)$ is compared with the predictions from bosonization theory [14]. The power law decay (2.19) applies to an infinite 1D system. For a more reliable comparison with the numerics we include finite size effects in the bosonization calculations [50].

   The finite band width $1/\tau$ on the lattice requires that the dimensionless interaction strength κ is small compared to unity. As we see in Fig. 2.5 the agreement with the continuum results (dashed curves) remains quite satisfactory
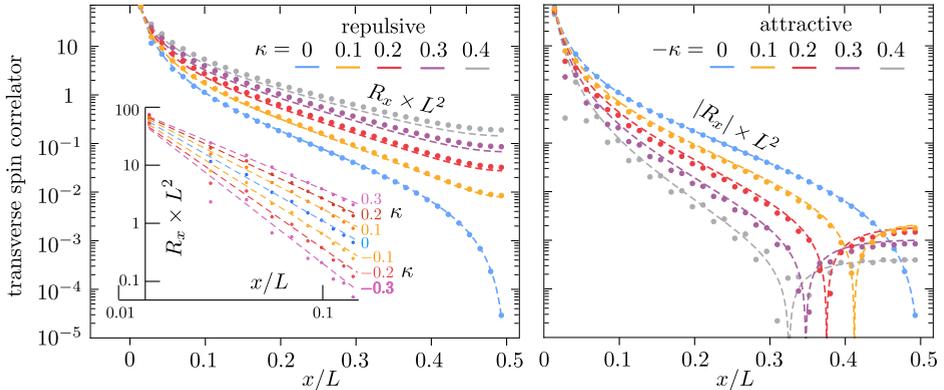
Figure 2.5. Main panels: The data points show the quantum Monte Carlo results for the correlator $R_x(x) = \frac{1}{4}\langle \boldsymbol{\psi}^\dagger(x)\boldsymbol{\sigma}_x\boldsymbol{\psi}(x)\boldsymbol{\psi}^\dagger(0)\boldsymbol{\sigma}_x\boldsymbol{\psi}(0)\rangle$ of the helical Luttinger liquid, on the space-time lattice with parameters $\beta/\tau = 34$, $L/a = 71$, $v_F = a/\tau$. The different colors refer to different Hubbard interaction strengths $\kappa = Ua/2\pi v_F$, repulsive on the left panel and attractive on the right panel. In the latter case the correlator R_x changes sign, the plot shows the absolute value on a log-linear scale. The x-dependence at x and $L - x$ is the same, because of the periodic boundary conditions, so only the range $0 < x < L/2$ is plotted. The numerical data on the lattice is compared with the analytical bosonization theory in the continuum (dashed curves [50]). Note that the lattice calculation slightly overestimates the interaction strength, for both the repulsive and attractive cases. The inset in the left panel combines data for both repulsive and attractive interactions on a log-log scale, to compare with the power law decay (2.19) (dashed lines).

for $|\kappa|$ up to about 0.4. We stress that this comparison does not involve any adjustable parameter.

2.5 Conclusion

We have shown that it is possible to faithfully represent an interacting Luttinger liquid on a lattice, without compromising the fundamental symmetries of massless fermions. The key step is a space-time discretization of the Lagrangian which is *local* but does not introduce a spurious second species of low-energy excitations. We have tested the validity of this "tangent fermion" approach in the simplest setting where we can compare with the known bosonization results in the continuum.

We anticipate that tangent fermions can become a powerful tool for the study of topological states of matter, where it is essential to maintain the topological protection of an unpaired Dirac cone. An application to the fermionic Casimir

effect was published in Ref. [51]. We have shown that the technique can be applied to quantum Monte Carlo calculations, but we expect it to be more generally applicable to fermionic lattices. Indeed, a second quantized formulation has very recently been used to avoid fermion doubling in the context of tensor networks [52].

Appendices

2.A Derivation of the Euclidean action in the tangent discretization

In this appendix, we explain how to arrive at the Euclidean action given in Eqs. (2.12) and (2.13). In particular, we show that the shift in chemical potential, originating from the normal ordering of the density operator in the Hubbard-interaction Lagrangian (2.8), is absent in the Euclidean action. We start from the continuum Hamiltonian $H = H_0 + H_{\text{Hubbard}}$, with

$$
\begin{aligned}
H_0 &= \sum_{\sigma,k} \sigma v_{\text{F}} k : \psi_\sigma^\dagger(k) \psi_\sigma(k): \\
&= \sum_{\sigma,k} \sigma v_{\text{F}} k \left[\psi_\sigma^\dagger(k) \psi_\sigma(k) - 1 + \theta(\sigma k) \right],
\end{aligned}
\tag{2.20}
$$

$$
H_{\text{Hubbard}} = U \int dx \, n_+(x) n_-(x),
\tag{2.21}
$$

$$
\begin{aligned}
n_\sigma(x) &= :\psi_\sigma(x)^\dagger \psi_\sigma(x): \\
&= \frac{1}{L} \sum_{k \neq k'} e^{i(k-k')x} [\psi_\sigma(k')^\dagger \psi_\sigma(k) + (\theta(\sigma k) - 1)\delta_{kk'}],
\end{aligned}
\tag{2.22}
$$

where the normal ordering $: \cdots :$ brings to the right operators $\psi_\sigma(k)$ with $\sigma k > 0$, and $\psi_\sigma^\dagger(k)$ with $\sigma k \leq 0$. Here θ is the unit step function, defined by $\theta(\sigma k) = 1$ for $\sigma k > 0$, and $\theta(\sigma k) = 0$ for $\sigma k \leq 0$.

We introduce fermionic coherent states $|\Psi\rangle$, which satisfy

$$
\psi_\sigma(k)|\Psi\rangle = \Psi_\sigma(k)|\Psi\rangle, \quad \langle\Psi|\psi_\sigma^\dagger(k) = \langle\Psi|\bar{\Psi}_\sigma(k).
\tag{2.23}
$$

Then, with $\tau = \beta/N$ and $|\Psi(0)\rangle = -|\Psi(N)\rangle$, where N is a positive integer, the

partition function is

$$Z = \operatorname{Tr} e^{-\beta H} = \lim_{N \to \infty} \int \prod_{t=1}^{N} \mathcal{D}\Psi(t)\mathcal{D}\bar{\Psi}(t) e^{-\bar{\Psi}(t)\Psi(t)} \langle \Psi(t)|e^{-\tau H}|\Psi(t-1)\rangle, \tag{2.24}$$

where $\Psi(0) = -\Psi(N)$.

We perform a Hubbard-Stratonovich transformation,

$$e^{-\tau H_{\text{Hubbard}}} = \int \mathcal{D}W(t)\mathcal{D}W^*(t) \exp\left\{ \int dx - \frac{\tau|W(x,t)|^2}{|U|} \right.$$
$$\left. + \tau W(x,t)n_+(x) - \tau \operatorname{sign}(U)W^*(x,t)n_-(x) \right\}, \tag{2.25}$$

which yields

$$Z = \lim_{N \to \infty} \int \left(\prod_{t=1}^{N} \mathcal{D}\Psi(t)\mathcal{D}\bar{\Psi}(t)\mathcal{D}W(t)\mathcal{D}W^*(t) \right) \exp\left\{ \sum_t \left[-\int dx \frac{\tau|W(x,t)|^2}{|U|} \right.\right.$$
$$- \bar{\Psi}(t)[\Psi(t) - \Psi(t-1)] - \tau \sum_{\sigma,k} \sigma v_F k [\bar{\Psi}_\sigma(k,t)\Psi_\sigma(k,t-1) - 1 + \theta(\sigma k)]$$
$$+ \frac{\tau}{L} \int dx\, W(x,t) \sum_{k,k'} e^{i(k-k')x} [\bar{\Psi}_+(k',t)\Psi_+(k,t-1) + (\theta(k)-1)\delta_{kk'}]$$
$$\left.\left. - \frac{\tau}{L} \operatorname{sign}(U) \int dx\, W^*(x,t) \sum_{kk'} e^{i(k-k')x} [\bar{\Psi}_-(k',t)\Psi_-(k,t-1) + (-1+\theta(-k))\delta_{kk'}] \right] \right\}. \tag{2.26}$$

We make the variable change

$$\Psi_\sigma(k,t) \mapsto \frac{1}{2}[\Psi_\sigma(k,t) + \Psi_\sigma(k,t+1)], \tag{2.27}$$

under which the partition function becomes

$$
Z = \lim_{N \to \infty} \int \left(\prod_{t=1}^{N} \mathcal{D}\Psi(t)\mathcal{D}\bar{\Psi}(t)\mathcal{D}W(t)\mathcal{D}W^*(t) \right) \exp \left\{ \sum_{t} \left[-\int dx \frac{\tau |W(x,t)|^2}{|U|} \right.\right.
$$
$$
- \frac{1}{2} \sum_{\sigma} \sum_{k,k'} (\delta_{kk'} + \tau \Lambda_{\sigma}(k,k')) \, \bar{\Psi}_{\sigma}(k',t) [\Psi_{\sigma}(k,t+1) - \Psi_{\sigma}(k,t-1)]
$$
$$
-\tau \sum_{\sigma} \sum_{k} \sigma v_{\mathrm{F}} k \left(\bar{\Psi}_{\sigma}(k,t) \frac{\Psi_{\sigma}(k,t-1) + 2\Psi_{\sigma}(k,t) + \Psi_{\sigma}(k,t+1)}{4} - 1 + \theta(\sigma k) \right)
$$
$$
+ \frac{\tau}{L} \int dx \, W(x,t) \sum_{k,k'} e^{i(k-k')x} \Big((\theta(k)-1)\delta_{kk'}
$$
$$
+ \bar{\Psi}_{+}(k',t) \frac{\Psi_{+}(k,t+1) + 2\Psi_{+}(k,t) + \Psi_{+}(k,t-1)}{4} \Big)
$$
$$
- \frac{\tau}{L} \mathrm{sign}(U) \int dx \, W^*(x,t) \sum_{k,k'} e^{i(k-k')x} \Big((\theta(-k)-1)\delta_{kk'}
$$
$$
\left.\left.+ \bar{\Psi}_{-}(k',t) \frac{\Psi_{-}(k,t+1) + 2\Psi_{-}(k,t) + \Psi_{-}(k,t-1)}{4} \Big) \right] \right\}, \quad (2.28)
$$

where

$$
\Lambda_{\sigma}(k,k') = -\frac{\sigma v_{\mathrm{F}} k}{2} \delta_{kk'} + \frac{1}{2L} \int dx \big[W(x,t) e^{i(k-k')x} \delta_{\sigma+}
$$
$$
- \mathrm{sign}(U) W^*(x,t) e^{i(k-k')x} \delta_{\sigma-} \big]. \quad (2.29)
$$

We next make the substitution

$$
\bar{\Psi}_{\sigma}(k') \mapsto \sum_{k''} [\delta_{k'k''} - \tau \Lambda_{\sigma}(k',k'')] \Psi_{\sigma}(k''). \quad (2.30)
$$

Ignoring the subleading terms, the Jacobian of the variable change is

$$
\det(\delta_{k'k''} - \tau \Lambda_{\sigma}(k',k'')) = \exp \left\{ -\tau \sum_{k} \left(-\sigma v_{\mathrm{F}} k + \frac{1}{2L} \int dx [W(x,t) \right.\right.
$$
$$
\left.\left. - \mathrm{sign}(U) W^*(x,t)] \right) \right\}. \quad (2.31)
$$

The change of measure of Grassmann variables produces the inverse of the Jacobian, which cancels the shift in chemical potential [the term $\theta(\sigma k) - 1$] from normal ordering. This yields the action

$$
\begin{aligned}
Z = \lim_{N \to \infty} \int & \left(\prod_{t=1}^{N} \mathcal{D}\Psi(t)\mathcal{D}\bar{\Psi}(t)\mathcal{D}W(t)\mathcal{D}W^*(t) \right) \exp \left\{ \sum_t \left[-\int dx \frac{\tau |W(x,t)|^2}{|U|} \right. \right. \\
& - \frac{1}{2} \sum_{\sigma,k} \bar{\Psi}_\sigma(k,t) [\Psi_\sigma(k,t+1) - \Psi_\sigma(k,t-1)] \\
& - \tau \sum_{\sigma,k} \sigma v_{\mathrm{F}} k \bar{\Psi}_\sigma(k,t) \frac{\Psi_\sigma(k,t-1) + 2\Psi_\sigma(k,t) + \Psi_\sigma(k,t+1)}{4} \\
& + \tau \int dx\, W(x,t)\bar{\Psi}_+(x,t) \frac{\Psi_+(x,t+1) + 2\Psi_+(x,t) + \Psi_+(x,t-1)}{4} \\
& \left. \left. - \tau \operatorname{sign}(U) \int dx W^*(x,t)\bar{\Psi}_-(x,t) \frac{\Psi_-(x,t+1) + 2\Psi_-(x,t) + \Psi_-(x,t-1)}{4} \right] \right\}.
\end{aligned}
$$
(2.32)

Finally we can integrate out the Hubbard-Stratonovich field, substitute $\Psi_\sigma \mapsto 2(1 + \cos\hat{\omega}\tau)^{-1}\Psi_\sigma$, and apply the tangent discretization $k \mapsto 2a^{-1}\tan(ak/2)$, which results in

$$
\begin{aligned}
Z = \lim_{N \to \infty} \int & \left(\prod_{t=1}^{N} \mathcal{D}\Psi(t)\mathcal{D}\bar{\Psi}(t) \right) \exp \left\{ -\sum_t \left[2 \sum_{\sigma,k} \bar{\Psi}_\sigma(k)(-i\tan(\hat{\omega}\tau/2)\Psi_\sigma(k) \right. \right. \\
& \left. \left. + \tau\sigma v_{\mathrm{F}} \tan(k/2))\Psi_\sigma(k,t) + \tau U \sum_x \bar{\Psi}_+(x,t)\Psi_+(x,t)\bar{\Psi}_-(x,t)\Psi_-(x,t) \right] \right\}.
\end{aligned}
$$
(2.33)

For finite N, this is the partition function corresponding to the tangent-discretized action given in Eqs. (2.12) and (2.13) in the main text.

2.B   Quantum Monte Carlo calculation

2.B.1   Hubbard-Stratonovich transformation of the Euclidean action

To evaluate the fermionic path integral representation of the partition function,

$$
Z = \int \mathcal{D}\bar{\Psi} \int \mathcal{D}\Psi\, e^{-\mathcal{S}[\Psi,\bar{\Psi}]}
$$
(2.34)

we follow the usual auxiliary field approach [22, 23, 24, 25, 26], by which the two-body Hubbard interaction is transformed into a sum of one-body terms coupled to a fluctuating Ising field $s(x, t) \in \{+1, -1\}$. In a Hamiltonian formulation this is accomplished by the discrete Hubbard-Stratonovich transformation of Ref. [23]. We cannot follow that route, because the tangent fermion Hamiltonian is nonlocal, instead we need to work with the Lagrangian formulation — which is local.

Starting from the discretized Euclidean action in Eqs. (2.12) and (2.13) we factor out the two-body term,

$$e^{-\mathcal{S}} = e^{-\mathcal{S}_{\text{tangent}}} \prod_{x,t} e^{-U\tau \bar{\Psi}_+(x,t)\Psi_+(x,t)\bar{\Psi}_-(x,t)\Psi_-(x,t)}. \tag{2.35}$$

This is allowed because all bilinears $\bar{\Psi}\Psi$ of the anticommuting Grassmann fields commute. (The approximate Trotter splitting [25, 26] from the Hamiltonian formulation does not appear here.)

Focusing on one factor, we have the sequence of identities (using $\Psi^2 = \bar{\Psi}^2 = 0$)

$$\begin{aligned}
e^{-U\tau \bar{\Psi}_+\Psi_+\bar{\Psi}_-\Psi_-} &= 1 - U\tau \bar{\Psi}_+\Psi_+\bar{\Psi}_-\Psi_- \\
&= \tfrac{1}{2}\sum_{s=\pm}\left[1 + s\sqrt{|U\tau|}(\bar{\Psi}_+\Psi_+ - \text{sign}(U\tau)\bar{\Psi}_-\Psi_-) - U\tau s^2 \bar{\Psi}_+\Psi_+\bar{\Psi}_-\Psi_-\right] \\
&= \tfrac{1}{2}\sum_{s=\pm}\exp\left[s\sqrt{|U\tau|}(\bar{\Psi}_+\Psi_+ - \text{sign}(U\tau)\bar{\Psi}_-\Psi_-)\right]. \tag{2.36}
\end{aligned}$$

Collecting all factors we thus arrive at the desired Hubbard-Stratonovich transformation of the Euclidean action,

$$e^{-\mathcal{S}} = e^{-\mathcal{S}_{\text{tangent}}} \frac{1}{2^{\frac{\beta L}{\tau a}}} \sum_{s(x,t)=\pm 1} \exp\left[|U\tau|^{1/2}\sum_{x,t} s(x,t)\left(\bar{\Psi}_+(x,t)\Psi_+(x,t)\right.\right.$$
$$\left.\left. - \text{sign}(U\tau)\bar{\Psi}_-(x,t)\Psi_-(x,t)\right)\right], \quad (2.37)$$

In the tangent fermion discretization the charge density $\bar{\Psi}\Psi$ is rewritten in

terms of the locally coupled fields $\Phi, \bar{\Phi}$, cf. Eq. (2.6),

$$
\begin{aligned}
\bar{\Psi}_\pm(x,t)\Psi_\pm(x,t) &= \bar{\Phi}_\pm \hat{D}^\dagger |x,t\rangle\langle x,t|\hat{D}\Phi_\pm \\
&= \tfrac{1}{16}\bar{\Phi}_\pm(1+e^{-i\hat{k}a})(1+e^{-i\hat{\omega}t})|x,t\rangle\langle x,t|(1+e^{i\hat{k}a})(1+e^{i\hat{\omega}t})\Phi_\pm, \\
&= \tfrac{1}{16}\big[\bar{\Phi}_\pm(x,t)+\bar{\Phi}_\pm(x-a,t)+\bar{\Phi}_\pm(x,t+\tau)+\bar{\Phi}_\pm(x-a,t+\tau)\big] \\
&\quad \times \big[\Phi_\pm(x,t)+\Phi_\pm(x-a,t)+\Phi_\pm(x,t+\tau)+\Phi_\pm(x-a,t+\tau)\big].
\end{aligned}
\tag{2.38}
$$

The Jacobian $J = \det \hat{D}^\dagger \hat{D}$ of the transformation is independent of the Ising field.

For any given Ising field configuration $s(x,t)$ the action is now quadratic in the Grassmann fields $\Phi, \bar{\Phi}$,

$$
\mathcal{S}[\Phi,\bar{\Phi},s] = \sum_{\sigma,x,x',t,t'} \bar{\Phi}_\sigma(x',t') M_\sigma(x,x',t,t')[s]\Phi_\sigma(x,t), \tag{2.39}
$$

with a *local* kernel

$$
M_\sigma(x,x',t,t')[s] = \tfrac{1}{2}\big(-i(1+\cos\hat{k}a)\sin\hat{\omega}\tau + \sigma\gamma(1+\cos\hat{\omega}\tau)\sin\hat{k}a\big)
$$

$$
+ \delta_{x,x'}\delta_{t,t'}|U\tau|^{1/2}s(x,t)D^\dagger|x,t\rangle\langle x,t|D \times
\begin{cases}
\sigma & \text{if } U>0, \\
1 & \text{if } U<0.
\end{cases}
\tag{2.40}
$$

The Gaussian path integral over the fields $\Phi, \bar{\Phi}$ produces a weight functional

$$
P[s] = \int \mathcal{D}\bar{\Phi}\int \mathcal{D}\Phi \, e^{-\mathcal{S}[\Phi,\bar{\Phi},s]} = \det M_+[s]M_-[s] \tag{2.41}
$$

for the average over the Ising field. This final average is carried out by means of the Monte Carlo importance sampling algorithm.

2.B.2 Absence of a sign problem

For the Monte Carlo averaging we need to ascertain the absence of a sign problem: The weight functional $P[s]$ should be non-negative for any Ising field configuration. This is indeed the case: From Eq. (2.40) one sees that for the attractive interaction ($U<0$)

$$
M_-^*[s] = M_+[s] \Rightarrow P[s] = |\det M_+[s]|^2. \tag{2.42}
$$

(Note that $\hat{k} = -i\partial_x$ and $\hat{\omega} = i\partial_t$ changes sign upon complex conjugation.) For the repulsive interaction ($U>0$)

$$
M_-^\dagger[s] = -M_+[s] \Rightarrow P[s] = (-1)^{\beta L/\tau a}|\det M_+[s]|^2 = |\det M_+[s]|^2, \tag{2.43}
$$

because $\beta L/\tau a$ is an even integer.

2.B.3 Correlators

We apply the quantum Monte Carlo calculation to equal-time correlators of the form

$$
\begin{aligned}
\langle \psi_\sigma^\dagger(x_1)\psi_\sigma(x_2)\psi_{\sigma'}^\dagger(x_3)\psi_{\sigma'}(x_4)\rangle &= \langle (\hat{D}\phi_\sigma)^\dagger(x_1)(\hat{D}\phi_\sigma)(x_2)(\hat{D}\phi_{\sigma'})^\dagger(x_3)(\hat{D}\phi)_{\sigma'}(x_4)\rangle \\
&= \int \mathcal{D}\bar{\Phi}\int \mathcal{D}\Phi\,\langle e^{-S[\Phi,\bar{\Phi},s]}\rangle_s (\bar{\Phi}_\sigma \hat{D}^\dagger)(x_1)(\hat{D}\Phi_\sigma)(x_2)(\bar{\Phi}_{\sigma'}\hat{D}^\dagger)(x_3)(\hat{D}\Phi)_{\sigma'}(x_4) \\
&= \frac{1}{Z}\sum_{s(x,t)=\pm 1} P[s]\Big(\hat{A}_\sigma(x_2,x_1)[s]\hat{A}_{\sigma'}(x_4,x_3)[s]-\delta_{\sigma\sigma'}\hat{A}_\sigma(x_4,x_1)[s]\hat{A}_\sigma(x_2,x_3)[s]\Big).
\end{aligned}
$$
$$(2.44)$$

In the final equality we defined $\hat{A}_\sigma[s] = \hat{D}M_\sigma^{-1}[s]\hat{D}^\dagger$ and we have used the integration formula (Wick's theorem)

$$
\int \mathcal{D}\bar{\Phi}\int \mathcal{D}\Phi\, e^{-\bar{\Phi}M\Phi}\Phi_k\Phi_l\bar{\Phi}_m\bar{\Phi}_n = (\det M)\big[(M^{-1})_{kn}(M^{-1})_{lm}-(M^{-1})_{km}(M^{-1})_{ln}\big].
$$
$$(2.45)$$

We consider the spin correlator

$$
\begin{aligned}
R_x(x) &= \tfrac{1}{4}\langle \boldsymbol{\psi}^\dagger(x)\sigma_x\boldsymbol{\psi}(x)\boldsymbol{\psi}^\dagger(0)\sigma_x\boldsymbol{\psi}(0)\rangle \\
&= -\tfrac{1}{4}\big(\langle \psi_\uparrow^\dagger(x)\psi_\uparrow(0)\psi_\downarrow^\dagger(y)\psi_\downarrow(x)\rangle + \langle \psi_\downarrow^\dagger(x)\psi_\downarrow(0)\psi_\uparrow^\dagger(0)\psi_\uparrow(x)\rangle\big).
\end{aligned}
$$
$$(2.46)$$

In the second equality we used spin conservation symmetry,

$$
\langle \psi_\uparrow^\dagger(x)\psi_\downarrow(x)\psi_\uparrow^\dagger(0)\psi_\downarrow(0)\rangle = 0, \quad \langle \psi_\downarrow^\dagger(x)\psi_\uparrow(x)\psi_\downarrow^\dagger(0)\psi_\uparrow(0)\rangle = 0.
$$
$$(2.47)$$

We substitute Eq. (2.44) into to Eq. (2.46),

$$
R_x(x) = -\tfrac{1}{4}\big\langle \hat{A}_\uparrow(0,x)[s]\hat{A}_\downarrow(x,0)[s] + \hat{A}_\downarrow(0,x)[s]\hat{A}_\uparrow(x,0)[s]\big\rangle_s.
$$
$$(2.48)$$

Using the symmetries (2.42) and (2.43) of the M-matrix we simplify it to

$$
R_x(x) = \begin{cases} \tfrac{1}{4}\big\langle \big|A_\uparrow(x,0)[s]\big|^2 + \big|A_\uparrow(0,x)[s]\big|^2\big\rangle_s & \text{if } U > 0, \\ -\tfrac{1}{2}\,\text{Re}\big\langle \{A_\uparrow(x,0)[s]A_\uparrow^*(0,x)[s]\}\big\rangle_s & \text{if } U < 0, \end{cases}
$$
$$(2.49)$$

with $\{\cdots\}$ the anticommutator.

The average in Eq. (2.49) is over the Ising field s. To improve the statistics we make use of translational invariance in space and imaginary time, by additionally averaging the correlator over the initial position (replacing $(x,0)\mapsto(x+y,y)$ with $0 < y < L$), as well as over $0 < t < \beta$.

2.B.4   Monte Carlo averaging

For the Monte Carlo averaging we perform local updates of the auxiliary Ising field, one spin-flip at the time. An operator average is then sampled at each Monte Carlo iteration, which includes $\beta L/\tau a$ local spin-flip steps.

We have tried out three alternative numerical methods:

1. The first method is a simple dense matrix calculation, where we recalculate $P[s]$ after each spin-flip and $A_\uparrow[s]$ after each Monte Carlo step, using neither the sparsity of the M-matrix nor the locality of the update. This is optimal for systems of small sizes ($L/a \lesssim 11$, $\beta/\tau \lesssim 6$).

2. In the second method we use the locality of the update of the Ising field, by employing the Woodbury formula for the update of $P[s]$ and $A_\uparrow[s]$. This is favorable for systems of medium sizes ($L/a \approx 41$, $\beta/\tau \approx 20$).

3. In the third method we use the sparsity of the M-matrix, with the help of the SuperLU library.[3] This gives the best performance for large systems ($L/a \gtrsim 61$, $\beta/\tau \gtrsim 30$).

In Fig. 2.6 we compare results for three system sizes. We fix the ratio $a/\tau = v_\mathrm{F}$ of the discretization units of space and (imaginary) time and for each choice of a, τ we ensure that L/a is an odd integer and β/τ is an even integer (to avoid the pole in the tangent dispersion). The size dependence is relatively weak for the repulsive interaction, and more significant for the attractive interaction near values of x where the correlator changes sign.

2.C   Bosonization results

The curves in Fig. 2.5 are the bosonization results for the spin correlator $R_x(x)$ of the helical Luttinger liquid on a ring of length L. We describe that calculation.

---

[3]X. S. Li, *An overview of SuperLU: Algorithms, implementation, and user interface, ACM Transactions on Mathematical Software*, **31**, 302 (2005).
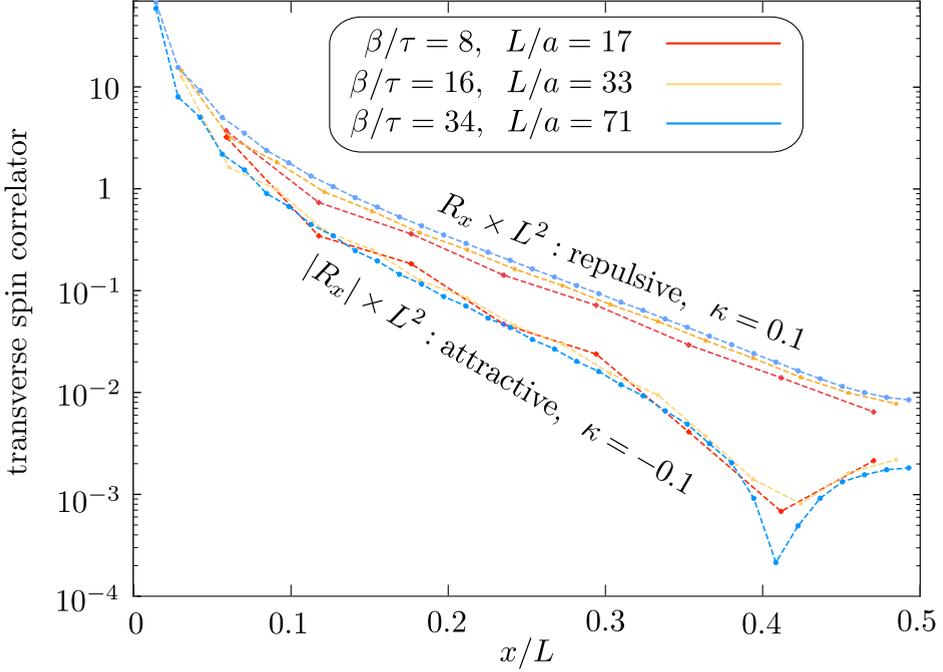
Figure 2.6. Quantum Monte Carlo results for the correlator $R_x(x) = \langle \psi^\dagger(x)\sigma_x\psi(x)\psi^\dagger(0)\sigma_x\psi(0)\rangle$ of the helical Luttinger liquid (interaction strength $|\kappa| = 0.1$), on the space-time lattice for three different lattice sizes (at fixed $a/\tau = v_F$). The data for the largest system corresponds to Fig. 2.5 from the main text. The dotted line connecting the data points is a guide to the eye.

2.C.1 Bosonic form of the Hamiltonian

We start directly from the bosonic form of the Luttinger Hamiltonian [14],

$$H = \frac{2\pi v_F}{L}\left[\sum_{n_q=1}^{\infty} n_q \left(b_{q\uparrow}^\dagger b_{q\uparrow} + b_{q\downarrow}^\dagger b_{q\downarrow}\right) - \kappa \sum_{n_q=1}^{\infty} n_q \left(b_{q\uparrow}^\dagger b_{q\downarrow}^\dagger + b_{q\uparrow} b_{q\downarrow}\right)\right.$$

$$\left. + \tfrac{1}{2}N_\uparrow(N_\uparrow + 1) + \tfrac{1}{2}N_\downarrow(N_\downarrow + 1) + \kappa N_\uparrow N_\downarrow \right]. \quad (2.50)$$

The bosonic creation and annihilation operators $b^\dagger, b$ are constructed from the fermionic operators $c^\dagger, c$ by

$$b_{q\sigma}^\dagger = \frac{i}{\sqrt{n_q}} \sum_k c_{(k+q)\sigma}^\dagger c_{k\sigma}, \quad q = \frac{2\pi}{L}\sigma n_q. \quad (2.51)$$

We impose periodic boundary conditions, quantizing $k = 2\pi n/L$, $n \in \mathbb{Z}$. The bosonic wave number $q = 2\pi\sigma n_q/L$ is defined such that $n_q > 0$ and the sign of q is fixed by the spin index.

The normally ordered fermionic number operator

$$N_\sigma = \sum_k :c_{k\sigma}^\dagger c_{k\sigma}: \ = \sum_k \left(c_{k\sigma}^\dagger c_{k\sigma} - \langle 0|c_{k\sigma}^\dagger c_{k\sigma}|0\rangle \right) \qquad (2.52)$$

commutes with the bosonic operators. The Fermi sea expectation value $\langle 0|c_{k\sigma}^\dagger c_{k\sigma}|0\rangle$ is defined such that wave numbers $\sigma k \leq 0$ contribute, so all states with energy $E \leq 0$, including the spin-up and spin-down states at $k = 0$. For later use we note that this implies that

$$\langle N_\sigma \rangle = 1/2 - 1 = -1/2 \qquad (2.53)$$

at zero temperature in a half-filled band (the state at $k = 0$ only contributes $1/2$ per spin direction to the ground state).

The Hamiltonian can be diagonalised by a Bogoliubov transformation [14],

$$B_{q\pm} = 2^{-3/2}(K^{-1/2} + K^{1/2})(b_{q\uparrow} \mp b_{q\downarrow}) \pm 2^{-3/2}(K^{-1/2} - K^{1/2})(b_{q\uparrow}^\dagger \mp b_{q\downarrow}^\dagger),$$
$$(2.54)$$

with $K = \sqrt{1-\kappa}/\sqrt{1+\kappa}$, resulting in

$$H = \frac{2\pi v_F}{L}\left[\sqrt{1-\kappa^2} \sum_{n_q=1}^\infty n_q(B_{q+}^\dagger B_{q+} + B_{q-}^\dagger B_{q-}) \right.$$
$$\left. + \tfrac{1}{2}N_\uparrow(N_\uparrow + 1) + \tfrac{1}{2}N_\downarrow(N_\downarrow + 1) + \kappa N_\uparrow N_\downarrow \right]. \qquad (2.55)$$

2.C.2 Spin correlator in terms of the bosonic fields

We wish to compute the (equal-time) spin correlator

$$R_x(x) = \tfrac{1}{4}\langle \psi^\dagger(x)\sigma_x\psi(x)\psi^\dagger(0)\sigma_x\psi(0)\rangle - \tfrac{1}{2}\,\mathrm{Re}\,\langle \psi_\uparrow^\dagger(x)\psi_\uparrow(0)\psi_\downarrow^\dagger(0)\psi_\downarrow(x)\rangle. \qquad (2.56)$$

In the second equality we used spin conservation symmetry (2.47) and translational symmetry,

$$\langle \psi_\uparrow^\dagger(x)\psi_\downarrow(x)\psi_\downarrow^\dagger(0)\psi_\uparrow(0)\rangle = \langle \psi_\uparrow^\dagger(0)\psi_\downarrow(0)\psi_\downarrow^\dagger(-x)\psi_\uparrow(-x)\rangle$$
$$= \langle \psi_\uparrow^\dagger(0)\psi_\downarrow(0)\psi_\downarrow^\dagger(x)\psi_\uparrow(x)\rangle^*. \qquad (2.57)$$

The correlator diverges when $x \to 0$, we regularize this ultraviolet divergence with cutoff length a_0.

The fermion field is related to the bosonic operators by the "refermionization" relation [14]

$$\psi_\sigma(x) = \frac{1}{\sqrt{2\pi a_0}} F_\sigma e^{-i\sigma 2\pi N_\sigma x/L} e^{-i\phi_\sigma(x)}, \tag{2.58}$$

where F_σ is a Klein factor and

$$\phi_\sigma(x) = -\sum_{n_q=1}^{\infty} \frac{1}{\sqrt{n_q}} e^{-\pi n_q a_0/L} \left(e^{-iqx} b_{q\sigma} + e^{iqx} b_{q\sigma}^\dagger \right). \tag{2.59}$$

The correlator then takes the form

$$R_x(x) = -\tfrac{1}{2} \operatorname{Re} \frac{1}{(2\pi a_0)^2} \langle e^{i\phi_\uparrow(x)} e^{i2\pi N_\uparrow x/L} F_\uparrow^\dagger F_\uparrow e^{-i\phi_\uparrow(0)} e^{i\phi_\downarrow(0)} F_\downarrow^\dagger F_\downarrow e^{i2\pi N_\downarrow x/L} e^{-i\phi_\downarrow(x)} \rangle$$

$$= -\tfrac{1}{2} \operatorname{Re} \frac{1}{(2\pi a_0)^2} \langle e^{i2\pi (N_\downarrow + N_\uparrow)x/L} \rangle \langle e^{i\phi_\uparrow(x)} e^{-i\phi_\uparrow(0)} e^{i\phi_\downarrow(0)} e^{-i\phi_\downarrow(x)} \rangle, \tag{2.60}$$

where we used the identity $F_\sigma^\dagger F_{\sigma'} = \delta_{\sigma\sigma'}$. In the second equality the expectation value has been factored into a product of two expectation values, which is allowed because every state can be completely and uniquely described by the number of fermions N_σ and bosonic excitations $b_{q\sigma}^\dagger b_{q\sigma}$, implying the independence of their expectation values.

The next step is to transform to the eigenbasis of the B-operators,

$$\Phi_\sigma(x) = -\sum_{n_q=1}^{\infty} \frac{1}{\sqrt{n_q}} e^{-\pi n_q a_0/L} \left(e^{-iqx} B_{q\sigma} + e^{iqx} B_{q\sigma}^\dagger \right), \tag{2.61}$$

by means of the relations

$$\begin{aligned}
\phi_\uparrow = {}& -2^{-3/2}(K^{-1/2} + K^{1/2})[\Phi_+(x) + \Phi_-(-x)] \\
& -2^{-3/2}(K^{-1/2} - K^{1/2})[\Phi_+(-x) - \Phi_-(x)], \tag{2.62a}
\end{aligned}$$

$$\begin{aligned}
\phi_\downarrow = {}& -2^{-3/2}(K^{-1/2} + K^{1/2})[\Phi_-(x) - \Phi_+(-x)] \\
& +2^{-3/2}(K^{-1/2} - K^{1/2})[\Phi_-(-x) + \Phi_+(x)]. \tag{2.62b}
\end{aligned}$$

We thus evaluate the expectation value

$$
\begin{aligned}
&\langle e^{i\phi_\uparrow(x)} e^{-i\phi_\uparrow(0)} e^{i\phi_\downarrow(0)} e^{-i\phi_\downarrow(x)} \rangle \\
&= \left\langle e^{-i\sqrt{\frac{K}{2}}(\Phi_+(x)+\Phi_+(-x)-2\Phi_+(0))} \right\rangle \left\langle e^{-i\sqrt{\frac{K}{2}}(\Phi_-(x)-\Phi_-(-x))} \right\rangle \\
&\quad \times e^{[\Phi_+(x),\Phi_+(0)]} e^{-\frac{1}{4}[\Phi_+(x),\Phi_+(-x)]} e^{-\frac{1}{4}[\Phi_-(x),\Phi_-(-x)]},
\end{aligned}
\tag{2.63}
$$

where we used the Baker-Campbell-Hausdorff formula and the fact that the commutator $[\Phi_\sigma(x),\Phi_\sigma(y)]$ is a c-number.

Because of inversion symmetry,

$$
[\Phi_+(x),\Phi_+(-x)] = [\Phi_-(-x),\Phi_-(x)] = -[\Phi_-(x),\Phi_-(-x)],
\tag{2.64}
$$

the last two exponentials in Eq. (2.63) cancel each other. The identity for the thermal average $\langle e^B \rangle = e^{\langle B^2 \rangle/2}$ of an operator B that is linear in free bosonic operators then gives

$$
\left\langle e^{-i\sqrt{\frac{K}{2}}(\Phi_+(x)+\Phi_+(-x)-2\Phi_+(0))} \right\rangle = e^{-\frac{K}{4}\langle 6\Phi_+^2(0)+\{\Phi_+(x),\Phi_+(-x)\}-4\{\Phi_+(x),\Phi_+(0)\}\rangle},
\tag{2.65a}
$$

$$
\left\langle e^{-i\sqrt{\frac{K}{2}}(\Phi_-(x)-\Phi_-(-x))} \right\rangle = e^{-\frac{K}{4}\langle 2\Phi_-^2(0)-\{\Phi_-(x),\Phi_-(-x)\}\rangle},
\tag{2.65b}
$$

where we also used the translational symmetry $\langle \Phi_+(0)\Phi_+(x) \rangle = \langle \Phi_+(-x)\Phi_+(0) \rangle$. We need one more identity,

$$
e^{\langle\{\Phi_-(x),\Phi_-(-x)\}\rangle - \langle\{\Phi_+(x),\Phi_+(-x)\}\rangle} = 1,
\tag{2.66}
$$

again because of inversion symmetry, to finally arrive at

$$
R_x(x) = -\tfrac{1}{2}\,\mathrm{Re}\,\frac{1}{(2\pi a_0)^2}\langle e^{i2\pi N_{\text{tot}}x/L}\rangle e^{K\langle\{\Phi_+(x),\Phi_+(0)\}-2\Phi_+^2(0)\rangle} e^{[\Phi_+(x),\Phi_+(0)]},
\tag{2.67}
$$

with $N_{\text{tot}} = N_\uparrow + N_\downarrow$.

2.C.3   Evaluation of the thermal averages

It remains to thermally average the bosonic field correlators and the exponential of the fermionic number operators. We do the latter average first.

The number operators $N_\uparrow, N_\downarrow$ commute with each other and with the bosonic fields, so the average is a classical ensemble average with the Gibbs measure at

inverse temperature β and chemical potential μ,

$$G_N(x) \equiv \langle e^{i2\pi N_{\text{tot}} x/L} \rangle = \frac{\sum_{N_\uparrow, N_\downarrow = -\infty}^{\infty} e^{i2\pi N_{\text{tot}} x/L} e^{-\beta E + \beta \mu N_{\text{tot}}}}{\sum_{N_\uparrow, N_\downarrow = -\infty}^{\infty} e^{-\beta E + \beta \mu N_{\text{tot}}}}, \qquad (2.68a)$$

$$E = \frac{2\pi v_F}{L} \left[\tfrac{1}{2} N_\uparrow (N_\uparrow + 1) + \tfrac{1}{2} N_\downarrow (N_\downarrow + 1) + \kappa N_\uparrow N_\downarrow \right]. \qquad (2.68b)$$

The chemical potential $\mu = 0$ without interactions, corresponding to a half-filled band at zero temperature. To keep the half-filled band also for nonzero κ we adjust

$$\mu = -\tfrac{1}{2} \kappa \frac{2\pi v_F}{L}. \qquad (2.69)$$

Then $\lim_{\beta \to \infty} \langle N_\sigma \rangle = -1/2$ independent of the interaction strength $\kappa \in (-1, 1)$, as required by Eq. (2.53).

We next turn to the average of the bosonic field correlators:

$$\langle \Phi_\sigma(x) \Phi_\sigma(0) \rangle = \sum_{n_q, n_q' = 1}^{\infty} \frac{1}{\sqrt{n_q n_q'}} e^{-2\pi n_q a_0/L} \langle \left(e^{-iqx} B_{q\sigma} + e^{iqx} B_{q\sigma}^\dagger \right) \left(B_{q'\sigma} + B_{q'\sigma}^\dagger \right) \rangle$$

$$= \sum_{n_q = 1}^{\infty} \frac{1}{n_q} e^{-2\pi n_q a_0/L} \langle e^{-iqx} B_{q\sigma} B_{q\sigma}^\dagger + e^{iqx} B_{q\sigma}^\dagger B_{q\sigma} \rangle$$

$$= \sum_{n_q = 1}^{\infty} \frac{1}{n_q} e^{-2\pi n_q a_0/L} \left(\frac{e^{-i\sigma 2\pi n_q x/L}}{1 - e^{-n_q 2\pi v \beta/L}} + \frac{e^{i\sigma 2\pi n_q x/L}}{e^{n_q 2\pi v \beta/L} - 1} \right)$$

$$= \sum_{n_q = 1}^{\infty} \frac{1}{n_q} e^{-n_q (2\pi/L)(a_0 + i\sigma x)} + \sum_{n_q = 1}^{\infty} \frac{1}{n_q} e^{-2\pi n_q a_0/L} \frac{2\cos\left(2\pi n_q x/L\right)}{e^{n_q 2\pi v \beta/L} - 1}$$

$$= -\ln\left(1 - e^{-(2\pi/L)(a_0 + i\sigma x)}\right) + \sum_{n_q = 1}^{\infty} \frac{1}{n_q} e^{-2\pi n_q a_0/L} \frac{2\cos\left(2\pi n_q x/L\right)}{e^{n_q 2\pi v \beta/L} - 1}. \quad (2.70)$$

We subtract $\langle \Phi_\sigma^2(0) \rangle$ and expand to first order in the cutoff length a_0,

$$\langle \Phi_\sigma(x) \Phi_\sigma(0) - \Phi_\sigma^2(0) \rangle = G_\sigma(x) + \ln(2\pi a_0/L) + O(a_0),$$

$$G_\sigma(x) = -\ln\left(1 - e^{-i\sigma 2\pi x/L}\right) + \sum_{n_q = 1}^{\infty} \frac{4}{n_q} \frac{\sin^2(\pi n_q x/L)}{e^{n_q 2\pi v \beta/L} - 1}. \qquad (2.71)$$

With the help of two further identities,

$$\langle \{\Phi_+(x), \Phi_+(0)\} - 2\Phi_+^2(0) \rangle = 2 \operatorname{Re}\langle \Phi_+(x) \Phi_+(0) - \Phi_+^2(0) \rangle, \qquad (2.72a)$$

$$[\Phi_+(x), \Phi_+(0)] = 2i \operatorname{Im}\langle \Phi_+(x) \Phi_+(0) - \Phi_+^2(0) \rangle = 2\pi i(x/L - 1/2), \quad (2.72b)$$

we conclude that

$$R_x(x) = \frac{e^{2K \, \mathrm{Re} \, G_+(x)} \, \mathrm{Re}\left[e^{i2\pi x/L} G_N(x)\right]}{2L^2 (2\pi a_0/L)^{2-2K}}. \tag{2.73}$$

The two functions $G_N(x)$ and $G_+(x)$ can be computed efficiently from Eqs. (2.68) and (2.71). For the comparison with the lattice theory we identify the cutoff length a_0 with the lattice constant a.

2.C.4 Propagator

For reference we also give the finite-size bosonization result for the propagator:

$$C_\sigma(x) = \langle \psi_\sigma^\dagger(x,0)\psi_\sigma(0,0)\rangle = \frac{1}{2\pi a_0}\langle e^{i\sigma 2\pi N_\sigma x/L}\rangle \langle e^{i\phi_\sigma(x)} e^{-i\phi_\sigma(0)}\rangle$$

$$= \frac{\sigma}{2\pi i a_0}\left(\frac{2\pi a_0}{L}\right)^{(1/2)(K+1/K)} \langle e^{i\sigma\pi(2N_\sigma+1)x/L}\rangle e^{(1/2)(K+1/K)\,\mathrm{Re}\,G_\sigma(x)}. \tag{2.74}$$

Chapter 3

Luttinger liquid tensor network: sine versus tangent dispersion of massless Dirac fermions

3.1 Introduction

The linear energy-momentum relation, $E = \pm\hbar v k$, of massless Dirac fermions remains gapless in the presence of disorder, provided that a pair of fundamental symmetries, chiral symmetry and time reversal symmetry, are not both broken [54]. To preserve this so-called topological protection on a lattice one needs to work around the fermion doubling obstruction [5]: if the Brillouin zone contains multiple Dirac cones they can hybridize and open a gap at $E = 0$. The nearest-neighbor finite difference discretization suffers from this problem: The resulting sine dispersion, $E = (\hbar v/a) \sin ak$, has a spurious second Dirac cone at the edge $k = \pi/a$ of the Brillouin zone.

It was shown recently [45, 17] that an alternative discretization of the differential operator, introduced in the 1980's by Stacey [16], preserves a gapless Dirac cone in a disordered system. The dispersion is a tangent, $E = (2\hbar v/a) \tan(ak/2)$, with a pole rather than a zero at the Brillouin zone edge. No other discretization scheme (staggered fermions, Wilson fermions, SLAC fermions [18]) has this topological protection. One fundamental consequence is that the Casimir effect for lattice fermions requires the tangent discretization [51].

All of this is for non-interacting particles. Interacting models of massless Dirac fermions need a lattice formulation for numerical studies [55, 56, 57, 58], which use methods such as quantum Monte Carlo or DMRG (density matrix renor-

malization group). The Luttinger liquid with Hubbard interaction, a paradigmatic non-Fermi liquid [13, 21], can be solved analytically in the continuum via bosonization [3, 20], providing a testing ground for lattice calculations. Such a test was reported for quantum Monte Carlo in Ref. [59]. Here we consider the DMRG implementation.

The two techniques require a different approach, each with its own challenges. For quantum Monte Carlo the discretization is at the level of the Lagrangian, and the challenge is to ensure a positive action determinant (avoiding the so-called sign problem). For DMRG the discretization involves the representation of the second quantized Hamiltonian by a tensor network [60, 61]: a product of matrices of operators acting locally on each site. The challenge is to ensure that the rank of each matrix (the bond dimension) is small and does not grow with the number of sites.

Tangent fermions have a hidden locality originating from the fact that — although the tangent discretization produces a Hamiltonian with a highly non-local, non-decaying, coupling of distant sites [16] — the ground state can be obtained from a *local* generalized eigenproblem [44]. Our key finding is that this allows for an exact matrix-product-operator (MPO) representation of low bond dimension. In an independent study [52], Haegeman *et al.* reached the same conclusion.

In what follows we will compare the sine and tangent discretizations of the Luttinger Hamiltonian, and test the correlators against the continuum results. We first construct the MPO explicitly in Sec. 3.2. The correlators are calculated via the DMRG approach and compared with bosonization in Sec. 3.3. We conclude in Sec. 3.4. Appendix 3.A contains the connection between a local generalized eigenproblem and a scale-independent MPO.

3.2   Matrix product operator

The starting point of a tensor network DMRG calculation [57] is the representation of the Hamiltonian by a matrix product operator (MPO), to ensure that the variational ground state energy can be computed efficiently for a matrix product state.

In this section we construct the MPO representation of the one-dimensional (1D) Dirac Hamiltonian

$$H = -i\hbar v \begin{pmatrix} \partial/\partial x & 0 \\ 0 & -\partial/\partial x \end{pmatrix}, \tag{3.1}$$

discretized on a lattice. (The matrix structure refers to the spin degree of freedom.) Once we have done that we will compute the correlators via DMRG in the presence of a Hubbard interaction (Luttinger model).

3.2.1 Free fermions

Consider noninteracting, spinless chiral fermions on a chain of N sites (unit spacing), with hopping matrix elements t_{nm} ($n > m \geq 1$). (We will include the spin degree of freedom and the electron-electron interaction later on.) For an infinite translationally invariant lattice, $t_{nm} = t(n - m)$ is a Fourier coefficient of the dispersion relation,

$$E(k) = 2\operatorname{Re}\sum_{n=1}^{\infty} t(n)e^{ink}. \tag{3.2}$$

The second quantized Hamiltonian

$$H = \sum_{n>m=1}^{N} \left(t_{nm}c_n^\dagger c_m + t_{nm}^* c_m^\dagger c_n\right) \tag{3.3}$$

can be rewritten as a product of matrices $M^{(n)}$ that act only on site n, but the dimension of each matrix (the bond dimension) will typically grow linearly with N.

An exact MPO representation with scale-independent bond dimension is possible in two cases [62, 63, 64, 65]: for a short-range hopping ($t_{nm} \equiv 0$ for $n - m > r$) and for a long-range hopping with a polynomial-times-exponential distance dependence:

$$t_{nm} = 2t_0 e^{i\phi}(n - m)^p e^{\beta(n-m)}, \quad \beta \in \mathbb{C}, \quad p \in \mathbb{N}, \tag{3.4}$$

and linear combinations of this functional form. While the exponent $\beta = \beta_1 + i\beta_2$ can be an arbitrary complex number, the power p must be a non-negative integer [65]. A decaying $t_{nm} \propto 1/(n - m)^p$ does not qualify.

The sine dispersion corresponds to a short-range, nearest-neighbor hopping,

$$t_{nm} = (t_0/2i)\delta_{n-m,1} \Leftrightarrow E(k) = t_0 \sin k. \tag{3.5}$$

The MPO Hamiltonian has bond dimension 4,

$$H_{\text{sine}} = \tfrac{1}{2} i t_0 [M^{(1)} M^{(2)} \cdots M^{(N)}]_{1,4}, \tag{3.6a}$$

$$M^{(n)} = \begin{pmatrix} 1 & c_n & c_n^\dagger & 0 \\ 0 & 0 & 0 & c_n^\dagger \\ 0 & 0 & 0 & c_n \\ 0 & 0 & 0 & 1 \end{pmatrix}. \tag{3.6b}$$

A no-go theorem [5] forbids short-range hopping if one wishes to avoid fermion doubling and preserve chiral symmetry. If we also require a scale-independent bond dimension we need the hopping (3.4). In the simplest case $p = 0$ of a purely exponential distance dependence[1], one has the dispersion

$$E(k) = 2t_0 \frac{e^{\beta_1} \cos \phi - \cos(\beta_2 + k + \phi)}{\cos(\beta_2 + k) - \cosh \beta_1}. \tag{3.7}$$

This should be a continuous function in the interval $(-\pi, \pi)$, crossing $E = 0$ at $k = 0$ but not at any other point in this interval. The only parameter choice consistent with these requirements is $\phi = \pi/2$, $\beta_1 = 0$, $\beta_2 = \pi$, when

$$t_{nm} = 2i t_0 (-1)^{n-m} \Leftrightarrow E(k) = 2t_0 \tan(k/2). \tag{3.8}$$

This is Stacey's tangent dispersion[2] [16].

The corresponding MPO Hamiltonian is

$$H_{\text{tangent}} = 2i t_0 [M^{(1)} M^{(2)} \cdots M^{(N)}]_{1,4}, \tag{3.9a}$$

$$M^{(n)} = \begin{pmatrix} 1 & c_n & c_n^\dagger & 0 \\ 0 & -1 & 0 & c_n^\dagger \\ 0 & 0 & -1 & c_n \\ 0 & 0 & 0 & 1 \end{pmatrix}, \tag{3.9b}$$

again with bond dimension 4, differing from the sine MPO (3.6) by the -1's on the diagonal.

---

[1] The tangent discretization (3.8) corresponds to Eq. (3.4) with $p = 0$ (purely exponential distance dependence). More generally, one can take $p = 1, 2, \ldots$ (polynomial-times-exponential distance dependence), in which case the dispersion contains terms $\propto \tan(k/2)(1 + \cos k)^{-p}$. The MPO representation of the discretized Hamiltonian remains scale independent, but the bond dimension is larger than for $p = 0$.

[2] The Fourier series $\tan(k/2) = -2 \sum_{n=1}^{\infty} (-1)^n \sin nk$ implied by the identification (3.8) should be understood in the sense of a distribution: $\int_0^\pi \tan(k/2) f(k)\, dk = -2 \sum_{n=1}^{\infty} (-1)^n \int_0^\pi f(k) \sin nk\, dk$, with $f(k)$ a test function that vanishes at π.

3.2.2 Helical Luttinger liquid

We next include the spin degree of freedom and consider helical instead of chiral fermions,

$$H = \sum_{n>m=1}^{N} \left[t_{nm} \left(c_{n\uparrow}^{\dagger} c_{m\uparrow} - c_{n\downarrow}^{\dagger} c_{m\downarrow} \right) + \text{H.c.} \right] + \sum_{n=1}^{N} U_n. \qquad (3.10)$$

(H.c. denotes the Hermitian conjugate.) We have added an on-site Hubbard interaction,

$$U_i = U\left(n_{i\uparrow} - \tfrac{1}{2}\right)\left(n_{i\downarrow} - \tfrac{1}{2}\right), \quad n_{i\sigma} = c_{i\sigma}^{\dagger} c_{i\sigma}. \qquad (3.11)$$

The MPO representation for the tangent discretization (3.8) is

$$H_{\text{tangent}} = 2it_0 \left[M^{(1)} M^{(2)} \cdots M^{(N)} \right]_{1,6}, \qquad (3.12a)$$

$$M^{(n)} = \begin{pmatrix} 1 & c_{n\uparrow} & c_{n\uparrow}^{\dagger} & c_{n\downarrow} & c_{n\downarrow}^{\dagger} & (2it_0)^{-1} U_n \\ 0 & -1 & 0 & 0 & 0 & c_{n\uparrow}^{\dagger} \\ 0 & 0 & -1 & 0 & 0 & c_{n\uparrow} \\ 0 & 0 & 0 & -1 & 0 & -c_{n\downarrow}^{\dagger} \\ 0 & 0 & 0 & 0 & -1 & -c_{n\downarrow} \\ 0 & 0 & 0 & 0 & 0 & 1 \end{pmatrix}, \qquad (3.12b)$$

with bond dimension 6. For the sine discretization the -1's on the diagonal are replaced by 0's,

$$H_{\text{sine}} = \tfrac{1}{2}it_0 \left[M^{(1)} M^{(2)} \cdots M^{(N)} \right]_{1,6}, \qquad (3.13a)$$

$$M^{(n)} = \begin{pmatrix} 1 & c_{n\uparrow} & c_{n\uparrow}^{\dagger} & c_{n\downarrow} & c_{n\downarrow}^{\dagger} & (\tfrac{1}{2}it_0)^{-1} U_n \\ 0 & 0 & 0 & 0 & 0 & c_{n\uparrow}^{\dagger} \\ 0 & 0 & 0 & 0 & 0 & c_{n\uparrow} \\ 0 & 0 & 0 & 0 & 0 & -c_{n\downarrow}^{\dagger} \\ 0 & 0 & 0 & 0 & 0 & -c_{n\downarrow} \\ 0 & 0 & 0 & 0 & 0 & 1 \end{pmatrix}. \qquad (3.13b)$$

To deal with fermionic statistics, we apply the Jordan-Wigner transformation to the MPOs (see App. 3.B).

The MPOs written down so far refer to an open chain of N sites. To minimize finite-size effects periodic boundary conditions are preferrable: the chain is wrapped around a circle, and sites n and $n + N$ are identified. A translationally invariant hopping, $t_{nm} = t(n - m)$, then requires

$$t(N - n) = t(n)^*, \quad 1 \leq n \leq N - 1. \qquad (3.14)$$

For N odd the Hamiltonian in the tangent discretization (3.8) satisfies this condition without further modification: because of the all-to-all hopping a closing of the chain on a circle makes no difference. (For N even one would have antiperiodic boundary conditions[3].) We can therefore still use the MPO (3.12).

The sine discretization (3.5) requires an additional hopping term between sites 1 and N. We construct this MPO explicitly in App. 3.C.

3.3 Correlators

3.3.1 Free fermions

The propagator

$$C_\sigma(x, x') = \langle c_\sigma^\dagger(x) c_\sigma(x') \rangle, \quad \sigma \in \{\uparrow, \downarrow\} \leftrightarrow \{1, -1\}, \qquad (3.15)$$

of a non-interacting 1D Dirac fermion with dispersion $E(k) = \pm \hbar v k$ can be readily evaluated:

$$C_\sigma(x, x') = \frac{1}{Z} \operatorname{Tr} e^{-\beta H} c_\sigma^\dagger(x) c_\sigma(x') = \int_{-\infty}^{\infty} \frac{dk}{2\pi} \frac{e^{ik(x-x')}}{1 + e^{\beta E(k)}}$$

$$= \frac{\sigma \hbar v}{2i\beta \sinh[\pi(\hbar v/\beta)(x - x')]}, \qquad (3.16)$$

for $x \neq x'$, with $Z = \operatorname{Tr} e^{-\beta H}$ the partition function at inverse temperature $\beta = 1/k_B T$. This reduces to

$$\lim_{\beta \to \infty} C_\sigma(x, x') = \frac{\sigma}{2\pi i (x - x')} \qquad (3.17)$$

in the zero-temperature limit.

On a lattice ($x/a = n \in \mathbb{Z}$, $c_\sigma(x = na) \equiv c_\sigma(n)$) the integration range of k is restricted to the interval $(-\pi/a, \pi/a)$. In the zero-temperature limit, with $\sigma E(k) < 0$ for $-\pi/a < k < 0$, one then finds

$$C_\sigma(n, m) = \sigma \int_{-\pi/a}^{0} \frac{dk}{2\pi} e^{ika(n-m)} = \begin{cases} \frac{2\sigma}{2\pi i a(n-m)} & \text{if } n-m \text{ is odd,} \\ 0 & \text{if } n-m \text{ is even,} \end{cases} \qquad (3.18)$$

---

[3]As a consistency check, we note that in real space the fact that an odd (even) number N of lattice sites corresponds to periodic (antiperiodic) boundary conditions, ensures in momentum space that the discrete wave numbers avoid the pole of the tangent dispersion relation at the Brillouin zone boundary.

irrespective of the functional form of the dispersion relation $E(k)$. The continuum result (3.17) is only recovered if one averages over even and odd lattice sites.

The even-odd oscillation also appears in the transverse spin correlator,

$$R(x, x') = \tfrac{1}{4} \langle \boldsymbol{c}^\dagger(x) \sigma_x \boldsymbol{c}(x) \; \boldsymbol{c}^\dagger(x') \sigma_x \boldsymbol{c}(x') \rangle, \tag{3.19}$$

defined in terms of the spinor $\boldsymbol{c} = (c_\uparrow, c_\downarrow)$ and Pauli matrix σ_x.

For free fermions Wick's theorem gives

$$R(x, x') = -\frac{1}{4} \Big(C_\uparrow(x, x') C_\downarrow(x', x) + C_\downarrow(x, x') C_\uparrow(x', x) \Big), \tag{3.20}$$

which at zero temperature results in

$$R(x, x') = \frac{1}{2} \left[2\pi(x - x') \right]^{-2}, \tag{3.21}$$

in the continuum and

$$R(n, m) = \begin{cases} 2[2\pi a(n - m)]^{-2} & \text{if } n - m \text{ is odd,} \\ 0 & \text{if } n - m \text{ is even.} \end{cases} \tag{3.22}$$

The even-odd oscillation [15] can be removed in a path integral formulation, by discretizing the Lagrangian in both space and (imaginary) time [59], but in the Hamiltonian formulation considered here it is unavoidable. In what follows we will consider smoothed lattice correlators, defined by averaging the fermionic operators $c_\sigma(n)$ over nearby lattice sites. The precise form of the smoothing profile will not matter in the continuum limit $a \to 0$, we take the simple form

$$\bar{c}_{n\sigma} = \tfrac{1}{2} c_{n\sigma} + \tfrac{1}{2} c_{n+1\sigma}, \tag{3.23}$$

so an equal-weight average over adjacent sites. The smoothed correlators are then defined by

$$\bar{C}_\sigma(n, m) = \langle \bar{c}^\dagger_{n\sigma} \bar{c}_{m\sigma} \rangle, \tag{3.24a}$$

$$\bar{R}(n, m) = \tfrac{1}{4} \langle \bar{\boldsymbol{c}}^\dagger_n \sigma_x \bar{\boldsymbol{c}}_n \; \bar{\boldsymbol{c}}^\dagger_m \sigma_x \bar{\boldsymbol{c}}_m \rangle. \tag{3.24b}$$

3.3.2 DMRG calculation with Hubbard interaction

We represent the ground state wave function Ψ of the Luttinger liquid Hamiltonian (3.10) by a matrix product state (MPS) and carry out the tensor network DMRG algorithm [57] to variationally minimize $\langle \Psi | H | \Psi \rangle / \langle \Psi | \Psi \rangle$. (We used the TeNPy

Library [66] for these calculations.) We compare the results for tangent and sine discretization. The MPOs for both are exact with small bond dimension (given explicitly in App. 3.B and App. 3.C). The bond dimension χ of the MPS is increased until convergence is reached (see App. 3.D).

The Luttinger liquid is simulated at zero temperature ($\beta \to \infty$) and at fixed particle number $N = N_\uparrow + N_\downarrow$ (canonical ensemble). We take $N = 51$ an odd integer, with periodic boundary conditions for the MPO. The periodicity of the MPS is not prescribed *a priori*, to simplify the DMRG code. By setting $N_\uparrow = (N + 1)/2$ and $N_\downarrow = (N - 1)/2$ we model a half-filled band.

The bosonization theory of an infinite Luttinger liquid gives a power law decay of the zero-temperature, zero-chemical-potential correlators [13],

$$C_\sigma(x, x') \propto |x - x'|^{-(1/2)(K+1/K)}, \tag{3.25a}$$

$$R(x, x') \propto |x - x'|^{-2K}, \tag{3.25b}$$

$$K = \sqrt{(1 - \kappa)/(1 + \kappa)}, \quad \kappa = \frac{U}{2\pi t_0} \in (-1, 1). \tag{3.25c}$$

For repulsive interactions, $U > 0 \Rightarrow K < 1$, the transverse spin correlator R decays more slowly than the $1/x^2$ decay expected from a Fermi liquid.

The numerical results are shown in Figs. 3.1 and 3.2 (data points). The curves are the continuum bosonization formulas (including finite-size corrections, see App. 3.E). The lattice calculations with the tangent dispersion (crosses) agree nicely with the continuum formulas, without any adjustable parameter. The sine dispersion (plusses), in contrast, only agrees for free fermions. With interactions the sine dispersion gives an exponential decay of the propagator, indicative of the opening of an excitation gap.

3.4   Conclusion

We have constructed a Hamiltonian-based tensor network formulation of a Luttinger liquid on a 1D lattice, complementing the Lagrangian-based path integral formulation of Ref. [59]. The key step is the Hermitian discretization of the momentum operator $-i\hbar d/dx$ in a way that preserves the fundamental symmetries (chiral symmetry and time reversal symmetry) of massless Dirac fermions. We have compared two discretizations, both allowing for a tensor network of low, scale-independent bond dimension. In this concluding section we also discuss a third.
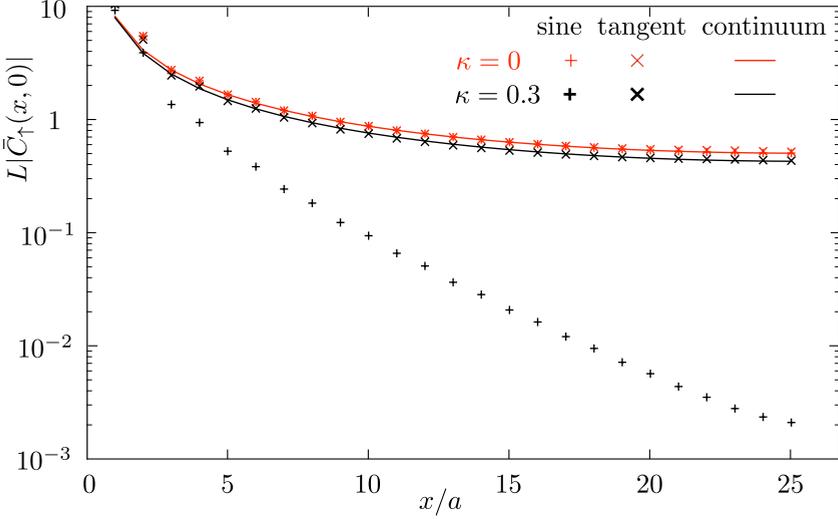
Figure 3.1. Data points: absolute value of the propagator $\bar{C}_\sigma(n, m)$, defined in Eq. (3.24a) for $\sigma = \uparrow$, $n = x/a$ and $m = 0$, calculated in the tensor network of $L/a = 51$ sites and bond dimension $\chi = 4096$ of the matrix-product state. Results are shown for the tangent and sine discretization of the Luttinger Hamiltonian, for free fermions and for a repulsive Hubbard interaction of strength $\kappa = U/2\pi t_0 = 0.3$. The curves are the analytical results in the continuum.

The three discretizations of the differential operator on a 1D lattice (unit lattice constant a) are the following:

$$\frac{df}{dx} \mapsto \tfrac{1}{2}[f(x + 1) - f(x - 1)] \quad \text{(sine dispersion)}, \tag{3.26a}$$

$$\frac{df}{dx} \mapsto 2\sum_{n=1}^{\infty}(-1)^n[f(x - n) - f(x + n)]$$

$$\text{(tangent dispersion)}, \tag{3.26b}$$

$$\frac{df}{dx} \mapsto \sum_{n=1}^{\infty}(-1)^n\frac{1}{n}[f(x - n) - f(x + n)]$$

$$\text{(sawtooth dispersion)}. \tag{3.26c}$$

The corresponding dispersion relations are shown in Fig. 3.3. The energy-momentum relation is a *sine* for the nearest-neighbor difference and a *tangent* for the long-range Stacey derivative [16]. The third dispersion is a (piecewise linear) *sawtooth*, produced by a nonlocal discretization known as the SLAC derivative in
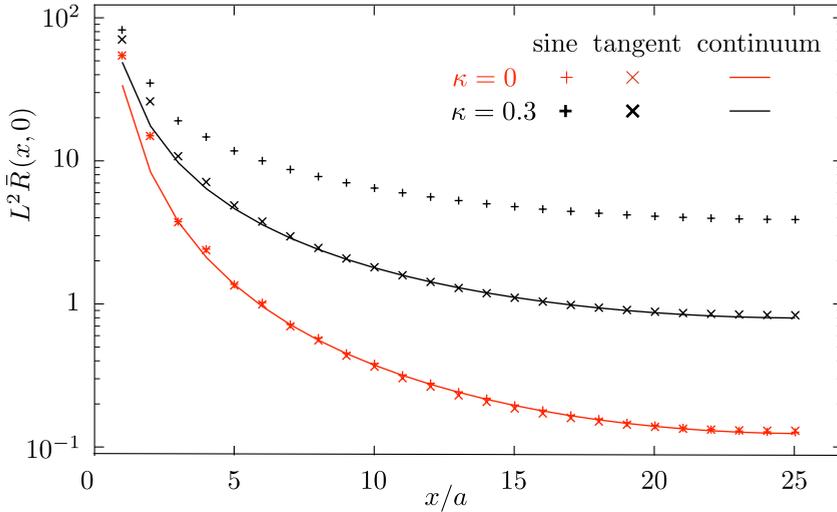
Figure 3.2. Same as Fig. 3.1, but now for the transverse spin correlator $\bar{R}(n, m)$ defined in Eq. (3.24b).

the particle physics literature [35].

The sine dispersion suffers from fermion doubling [18] — a second species of low-energy excitations appears at the Brillouin zone boundary. The tangent and sawtooth dispersion describe an unpaired chiral fermion, they rely on nonlocality to work around the theorem [5] that requires chiral fermions to come in pairs in any local theory on a lattice.

Both the Stacey derivative and the SLAC derivative couple arbitarily distant sites n, m, the former $\propto (-1)^{n-m}$ and the latter $\propto (-1)^{n-m} \times (n-m)^{-1}$. From the perspective of a tensor network there is an essential difference between the two: Because the MPO condition (3.4) allows for an exponential distance dependence but excludes a coupling that decays as a power law with distance, only the tangent dispersion has an exact MPO representation with scale-independent bond dimension — the sawtooth dispersion does not. Tangent fermions have a hidden locality, their spectrum is governed by a *local* generalized eigenproblem [44], which is at the origin of the efficient tensor network (see App. 3.A).

The method we developed here enables simulations of systems with various filling factors and scalar potentials, including those with disorder. By focusing on the impurity-free Luttinger liquid we could in this work test the numerical approach against analytical formulas. The close agreement gives us confidence that tangent fermion DMRG is a reliable method, which at least in 1D is highly
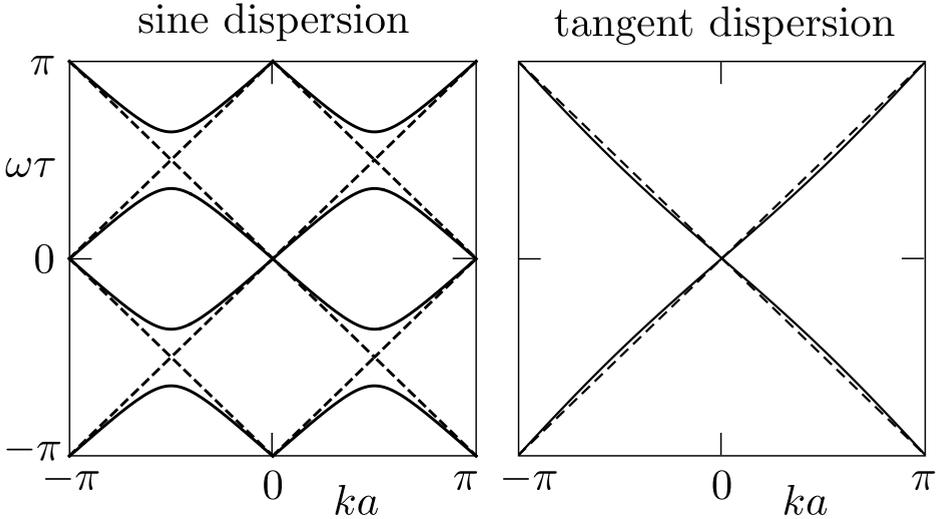
Figure 3.3. The three ways to discretize the derivative operator in Eq. (3.26) produce three different dispersion relations: sine (blue), tangent (red), and sawtooth (black). The energy-momentum relation of a chiral fermion is obtained from the discretized derivative by substituting $f(x + na) = e^{inka} f(x)$ and equating $-i\hbar v df/dx = E f$. The tangent and sawtooth dispersions are discontinuous at the Brillouin zone boundaries ($k = \pm\pi/a$), where the sine dispersion has a second root (fermion doubling). The three dispersion relations coincide near $k = 0$, so the corresponding discretized derivatives are equivalent if applied to functions that vary smoothly on the scale of the lattice spacing.

efficient.

The next step is to apply it to problems where no analytics exists, condensed matter and particle physics provide a variety of such problems. One class of applications is the stability of gapless chiral modes to the combination of disorder and interactions. Existing DMRG studies [67] work around the fermion doubling obstruction by studying a strip geometry with two edges — tangent fermions would allow for a single-edge implementation.

For such applications it would of interest to proceed from 1D to 2D. It is known that in two spatial dimensions the tangent discretization of $\sigma_x df/dx + \sigma_y df/dy$ still allows for a reformulation of $\mathcal{H}\psi = E\psi$ as a generalized eigenvalue problem [44]:

$$Q\psi = E\mathcal{P}\psi, \quad \mathcal{P} = \tfrac{1}{4}(1 + \cos k_x)(1 + \cos k_y), \qquad (3.27)$$
$$Q = \tfrac{1}{2}\sigma_x(1 + \cos k_y)\sin k_x + \tfrac{1}{2}\sigma_y(1 + \cos k_x)\sin k_y.$$

Therefore, we expect that an efficient 2D tensor network representation of the 2D

tangent Hamiltonian in the form of Projected Entangled Pair Operators (PEPO) [58] can be constructed similarly to the 1D MPO approach.

Appendices

3.A Local generalized eigenproblem allows for a scale-independent MPO

The DMRG approach described in the main text works because the tangent fermion Hamiltonian, while having a highly nonlocal long-range coupling, can still be described by an MPO with a low and scale-independent bond dimension. Ref. [44] attributes the "hidden locality" of tangent fermions to the fact that their spectrum is obtained from a *local* generalized eigenproblem. Here we make the connection to the scale-independent MPO explicit.

Consider 1D lattice fermions with a dispersion relation $E(k) = P(k)/Q(k)$ such that both $P(k)$ and $Q(k)$ are polynomials of finite degree in e^{ik},

$$P(k) = \sum_{n=0}^{N_P} p_n e^{ink}, \quad Q(k) = \sum_{n=0}^{N_Q} q_n e^{ink}. \tag{3.28}$$

For example, the tangent dispersion $E(k) = 2\tan(k/2)$ corresponds to $P(k) = 2i(1 - e^{ik})$, $Q(k) = 1 + e^{ik}$. In real space the operators P and Q couple sites separated by at most N_P or N_Q lattice spacings. The generalized eigenproblem $P\Psi = EQ\Psi$ is therefore local.

Consider first the case that

$$Q(k) = \prod_{n=1}^{N_Q}(\alpha_n - e^{ik}) \tag{3.29}$$

has *distinct* roots α_n. The partial fraction decomposition is

$$\frac{P(k)}{Q(k)} = D(k) + \sum_{n=1}^{N_Q} \frac{\beta_n}{\alpha_n - e^{ik}} \tag{3.30}$$

with $D(k)$ a polynomial of degree $N_P - N_Q$ (vanishing if $N_P < N_Q$). The sum over n corresponds in real space to a sum over coupling terms t_{ij} with an exponential spacing dependence $\propto (1/\alpha_n)^{i-j}$ for $i > j$. So in this case of distinct roots we are guaranteed to have an exact MPO representation with scale-independent bond dimension.

The situation is slightly more complicated if $Q(k)$ has repeated roots,

$$Q(k) = \prod_{n=1}^{L}(\alpha_n - e^{ik})^{\ell_n}, \quad \sum_{n=1}^{L} \ell_n = N_Q. \tag{3.31}$$

The partial fraction decomposition now reads

$$\frac{P(k)}{Q(k)} = D(k) + \sum_{n=1}^{L}\sum_{m=1}^{\ell_n} \frac{\beta_{nm}}{(\alpha_n - e^{ik})^m}. \tag{3.32}$$

A term $1/(\alpha_n - e^{ik})^m$ corresponds in real space to a coupling $t_{ij} \propto (1/\alpha_n)^{i-j} \times Z(i-j)$ that is an exponential times a polynomial Z in the spacing of degree $m-1$. This is still of the form (3.4) that allows for a scale-independent MPO [65].

3.B   Jordan-Wigner transformation

To enable the DMRG calculation, we need to convert the fermionic operators $c_{n\sigma}$ into bosonic operators $a_{n\sigma}$ (hard-core bosons, excluding double occupancy of a state). This is achieved by the Jordan-Wigner transformation,

$$\begin{aligned} c_{n\uparrow} &= F_1 F_2 \cdots F_{n-1} a_{n\uparrow}, \\ c_{n\downarrow} &= F_1 F_2 \cdots F_{n-1} F_n a_{n\downarrow}, \end{aligned} \tag{3.33}$$

with fermion parity operator

$$F_i = (1 - 2n_{i\uparrow})(1 - 2n_{i\downarrow}) = (-1)^{n_{i\uparrow}+n_{i\downarrow}}. \tag{3.34}$$

The transformation does not increase the bond dimension of the MPO, instead of Eq. (3.12) one now has

$$H_{\text{tangent}} = 2it_0 [M^{(1)}M^{(2)} \cdots M^{(N)}]_{1,6}, \tag{3.35a}$$

$$M^{(n)} = \begin{pmatrix} 1 & a_{n\uparrow}F_n & a_{n\uparrow}^{\dagger}F_n & a_{n\downarrow} & a_{n\downarrow}^{\dagger} & (2it_0)^{-1}U_n \\ 0 & -F_n & 0 & 0 & 0 & a_{n\uparrow}^{\dagger} \\ 0 & 0 & -F_n & 0 & 0 & a_{n\uparrow} \\ 0 & 0 & 0 & -F_n & 0 & -F_n a_{n\downarrow}^{\dagger} \\ 0 & 0 & 0 & 0 & -F_n & -F_n a_{n\downarrow} \\ 0 & 0 & 0 & 0 & 0 & 1 \end{pmatrix}. \tag{3.35b}$$

This is for the tangent discretization. For the sine discretization the $-F_n$ on the diagonal are replaced by 0,

$$H_{\text{sine}} = \tfrac{1}{2}it_0[M^{(1)}M^{(2)}\cdots M^{(N)}]_{1,6}, \tag{3.36a}$$

$$M^{(n)} = \begin{pmatrix} 1 & a_{n\uparrow}F_n & a_{n\uparrow}^\dagger F_n & a_{n\downarrow} & a_{n\downarrow}^\dagger & (\tfrac{1}{2}it_0)^{-1}U_n \\ 0 & 0 & 0 & 0 & 0 & a_{n\uparrow}^\dagger \\ 0 & 0 & 0 & 0 & 0 & a_{n\uparrow} \\ 0 & 0 & 0 & 0 & 0 & -F_n a_{n\downarrow}^\dagger \\ 0 & 0 & 0 & 0 & 0 & -F_n a_{n\downarrow} \\ 0 & 0 & 0 & 0 & 0 & 1 \end{pmatrix}. \tag{3.36b}$$

3.C Periodic boundary condition for MPO with sine discretization

The sine discretization (3.5) requires an additional hopping term between sites 1 and N. The modified MPO has bond dimension 10,

$$H_{\text{sine}} = \tfrac{1}{2}it_0[\tilde{M}^{(1)}\tilde{M}^{(2)}\cdots\tilde{M}^{(N)}]_{1,6}, \tag{3.37a}$$

$$\tilde{M}^{(n)} = \begin{pmatrix} M^{(n)} & \delta_{n,1}W^{(n)} \\ \delta_{n,N}W^{(n)} & (1-\delta_{n,1}-\delta_{n,N})W^{(n)} \end{pmatrix}, \tag{3.37b}$$

with $M^{(n)}$ as in Eq. (3.36) and

$$W^{(1)} = \begin{pmatrix} a_{1\uparrow}F_1 & a_{1\uparrow}^\dagger F_1 & a_{1\downarrow} & a_{1\downarrow}^\dagger \\ 0 & 0 & 0 & 0 \\ 0 & 0 & 0 & 0 \\ 0 & 0 & 0 & 0 \\ 0 & 0 & 0 & 0 \\ 0 & 0 & 0 & 0 \end{pmatrix}, \tag{3.37c}$$

$$W^{(1<n<N)} = \begin{pmatrix} F_n & 0 & 0 & 0 \\ 0 & F_n & 0 & 0 \\ 0 & 0 & F_n & 0 \\ 0 & 0 & 0 & F_n \end{pmatrix}, \tag{3.37d}$$

$$W^{(N)} = \begin{pmatrix} 0 & 0 & 0 & 0 & 0 & a_{N\uparrow}^\dagger \\ 0 & 0 & 0 & 0 & 0 & a_{N\uparrow} \\ 0 & 0 & 0 & 0 & 0 & -F_N a_{N\downarrow}^\dagger \\ 0 & 0 & 0 & 0 & 0 & -F_N a_{N\downarrow} \end{pmatrix} \tag{3.37e}$$
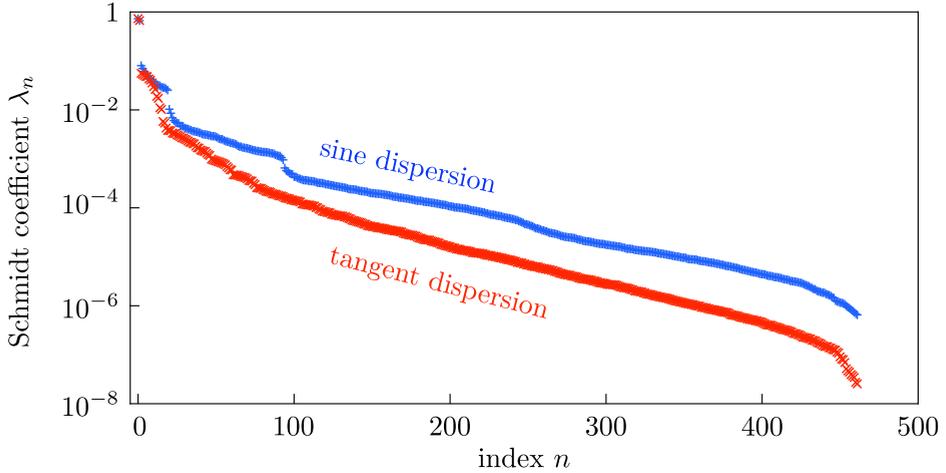
Figure 3.4. Log-linear plot of the Schmidt coefficients λ_n of the ground state wave function of the Luttinger liquid Hamiltonian (3.10) ($U = t_0$, $N = 11$ partitioned into $N_1 = 5$ and $N_2 = 6$), for the sine and tangent dispersions (3.5) and (3.8). The exponential decay allows for an MPS with bond dimension $\chi \ll 4^{N/2}$.

3.D   Convergence of the DMRG calculations

The tensor network formulation of the Luttinger liquid on an N-site chain is based on two matrix-product representations: of the operator H (MPO) and of the state Ψ (MPS). The MPO is exact, in terms of an N-fold product of 6×6 matrices of creation and annihilation operators.

The MPS is approximate: defined on N sites with physical dimensional d, it is an N-fold product of $\chi \times \chi \times d$ tensors that introduces an error of order $N \sum_{n>\chi} \lambda_n^2$, with $1 \geq \lambda_1 \geq \lambda_2 \geq \cdots \geq \lambda_{d^{N/2}} \geq 0$ the coefficients in the Schmidt decomposition of $\Psi \in \mathcal{H}_1 \otimes \mathcal{H}_2$ (describing the entanglement between the first and second half of the chain, with Hilbert spaces $\mathcal{H}_1$ and $\mathcal{H}_2$) [68].

The MPS is efficient at bond dimension $\chi \ll d^{N/2}$ if the Schmidt coefficients λ_n decrease exponentially with n. In Fig. 3.4 we check this for both the sine and tangent dispersions. In Fig. 3.5 we show the convergence of the DMRG calculation with increasing χ. We conclude that $\chi = 4^6 \ll 4^{25}$ (in our case $d = 4$) is sufficient for the results to converge to the expected behavior.
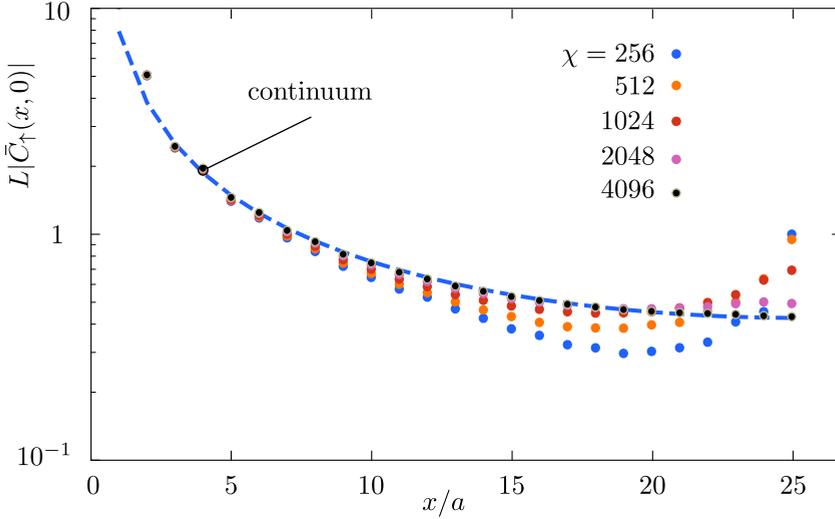
Figure 3.5. Dependence of the propagator on the bond dimension χ of the MPS in the tangent fermion Luttinger liquid ($L/a = 51$, $\kappa = 0.3$). The data in Fig. 3.1 (black crosses) corresponds to $\chi = 4096$.

3.E   Bosonization results with finite-size effects

The power law correlators (3.25) follow from bosonization of the helical Luttinger liquid in the limit of an infinite system [13]. To reliably compare with the numerical results on a lattice of length L we need to include finite size effects [14]. In Ref. [59] such a calculation was reported for the grand canonical ensemble (fixed chemical potential) at finite temperature, appropriate for quantum Monte Carlo. For the DMRG calculations we need the results at zero temperature in the canonical ensemble (fixed particle number $\mathcal{N} = \mathcal{N}_\uparrow + \mathcal{N}_\downarrow$).

The Hamiltonian of a helical Luttinger liquid with Hubbard interaction on a ring of length L (periodic boundary conditions) is given by

$$H = \int_{-L/2}^{L/2} dx \left(v\psi_\uparrow^\dagger(x) p_x \psi_\uparrow(x) - v\psi_\downarrow^\dagger(x) p_x \psi_\downarrow(x) + Ua\rho_\uparrow(x)\rho_\downarrow(x) \right). \quad (3.38)$$

The density $\rho_\sigma = \, : \psi_\sigma^\dagger \psi_\sigma :$ is normal ordered — the Fermi sea of a half-filled band (N particles) is subtracted.

The bosonization results in the canonical ensemble at zero temperature are

[59]

$$C_\sigma(x,0) = \frac{\sigma e^{i\pi(2N_\sigma - N)x/L}}{2\pi i a_* |(L/\pi a_*)\sin(\pi x/L)|^{(1/2)(K+1/K)}}, \tag{3.39a}$$

$$R(x,0) = \frac{\cos(2\pi(N - N)x/L)}{2(2\pi a_*)^2 |(L/\pi a_*)\sin(\pi x/L)|^{2K}}, \tag{3.39b}$$

$$K = \sqrt{(1-\kappa)/(1+\kappa)}, \quad \kappa = \frac{U}{2\pi t_0} \in (-1,1). \tag{3.39c}$$

The hopping energy is t_0 and a_* is a short-distance (UV) regularization constant. For the comparison with a lattice calculation we identify $t_0 = \hbar v/a$ and take $L/a = N$ an odd integer. The half-filled band corresponds to $N_\sigma = (N + \sigma)/2$. To relate the lattice constant a to the continuum regularization constant a_* we argue as follows.

In the continuum theory [14] large momentum transfers q are cut-off by the substitution

$$c^\dagger_{\sigma,q/2} c_{-q/2} \mapsto e^{-qa_*/2} c^\dagger_{\sigma,q/2} c_{-q/2}. \tag{3.40}$$

On the lattice the averaging (3.23) takes care of the UV regularization,

$$c^\dagger_{\sigma,q/2} c_{-q/2} \mapsto \bar{c}^\dagger_{\sigma,q/2} \bar{c}_{\sigma,-q/2} = f(q) c^\dagger_{\sigma,q/2} c_{\sigma,-q/2},$$
$$f(q) = \tfrac{1}{4}(1 + e^{-iqa/2})^2, \quad |f(q)| = \cos^2(qa/4). \tag{3.41}$$

We fix the ratio a/a_* by equating the integrated weight factors,

$$\int_0^{2\pi/a} e^{-qa_*/2}\,dq = \int_0^{2\pi/a} |f(q)|\,dq \Rightarrow a/a_* \approx 2. \tag{3.42}$$

The resulting correlators are plotted in Figs. 3.1 and 3.2.

3.F   Alternative tensor network representation of Ref. [52]

An alternative tensor network representation of the problem has been developed in Ref. [52], starting from the transformations

$$\boldsymbol{a} = D^\dagger \boldsymbol{c}, \quad \boldsymbol{b} = D^{-1}\boldsymbol{c}, \quad D_{nm} = \tfrac{1}{2}(\delta_{n,m} + \delta_{n,m-1}), \tag{3.43}$$

of the free fermion operators c_n. These are not canonical transformations, as a consequence the commutation relations of the a- and b-operators are nontrivial:

$$\{a_n, a^\dagger_m\} = (D^\dagger D)_{nm}, \quad \{b_n, b^\dagger_m\} = (D^\dagger D)^{-1}_{nm},$$
$$\{c_n, c^\dagger_m\} = \delta_{nm}, \quad \{b_n, a^\dagger_m\} = \delta_{nm}. \tag{3.44}$$

The corresponding N-fermion bases in Fock space are

$$|\psi\rangle = \sum_{n_i=0,1} \psi^\alpha_{n_1,...,n_N} |n_1, ..., n_N\rangle_\alpha,$$
$$|n_1, ..., n_N\rangle_\alpha = (\alpha_1^\dagger)^{n_1}...(\alpha_N^\dagger)^{n_N}, \tag{3.45}$$

with $\alpha \in \{a, b, c\}$. Only the c-basis is orthonormal, the two other bases produce non-diagonal norm matrices $\tilde{N}$,

$$_a\langle m_1, ..., m_N | n_1, ..., n_N\rangle_a = \tilde{N}^{m_1,...,m_N}_{n_1,...,n_N},$$
$$_b\langle m_1, ..., m_N | n_1, ..., n_N\rangle_b = (\tilde{N}^{-1})^{m_1,...,m_N}_{n_1,...,n_N},$$
$$_c\langle m_1, ..., m_N | n_1, ..., n_N\rangle_c = \delta_{m_1 n_1} \cdots \delta_{m_N n_N}. \tag{3.46}$$

The a and b bases are bi-orthogonal,

$$_a\langle m_1, ..., m_N | n_1, ..., n_N\rangle_b = \delta_{m_1 n_1} \cdots \delta_{m_N n_N}. \tag{3.47}$$

The motivation for these transformations is that the tangent fermion Hamiltonian becomes local in terms of the b-operators,

$$H_{\text{tangent}} = 2it_0 \sum_{n>m=1}^{N} (-1)^{n-m} \left(c_n^\dagger c_m - c_m^\dagger c_n \right) \tag{3.48a}$$

$$= \frac{t_0}{2i} \sum_{n=1}^{N} \left(b_{n+1}^\dagger b_n - b_n^\dagger b_{n+1} \right). \tag{3.48b}$$

Matrix elements of H_{tangent} in the a-basis, orthogonal to the b-basis, can therefore be evaluated efficiently.

The key step of Ref. [52] is to derive a scale-independent MPO representation of the norm matrix $\tilde{N}$ in the a-basis. We have followed a different route, we stay with the orthonormal c-basis and a nonlocal Hamiltonian, but we have found that it does not stand in the way of a scale-independent MPO representation.

Chapter 4

Majorana-metal transition in a disordered superconductor: percolation in a landscape of topological domain walls

4.1 Introduction

While a superconductor is a perfect conductor of electricity, it generally conducts heat poorly. Adding disorder is not expected to improve this, but in a two-dimensional (2D) superconductor with chiral p-wave pairing [69] the unexpected happens: If sufficiently many defects are added the thermal insulator becomes a thermal metal [70, 71, 72]. This unusual state is known as a Majorana metal, because the quasiparticles that conduct the heat are Majorana fermions (equal-weight superpositions of electrons and holes). Although the transition from a thermal insulator to a thermal metal has not yet been observed in experiments, it has been demonstrated in computer simulations [73, 74, 75, 76, 77, 78, 79, 80].

   The Majorana-metal transition is well understood if the defects consist of the Abrikosov vortices that appear when a perpendicular magnetic field is applied to a type-II superconductor. A vortex can bind sub-gap quasiparticles [81], but bound states in nearby vortices will not typically be aligned in energy, making them inefficient for heat transport. A special property of a chiral p-wave superconductor is that its vortices have a bound state exactly in the middle of the gap ($E = 0$, the Fermi level), a socalled Majorana zero-mode [82, 83, 84, 85, 86]. The energetic

alignment of Majorana zero-modes allows for resonant heat conduction when the density of Abrikosov vortices crosses a critical threshold [73, 74].

Electrostatic disorder in zero magnetic field can also produce a thermal metal phase [75]. The phase transition falls in the same universality class D as for vortex disorder [80], and one would expect the mechanism to be related in the same way to the appearance of Majorana zero-modes — even without any vortices to bind them. Can we demonstrate that in a computer simulation?

To address this question we use the spectral localizer approach pioneered by Loring and Schulz-Baldes [87, 88, 89, 90, 91, 92, 93, 94]. The spectral localizer embeds the Hamiltonian $\pm H$ on the diagonal of a 2×2 matrix, with the position operator $x \pm iy$ on the off-diagonal. Its spectrum quantifies whether Hamiltonian and position can be made commuting by a deformation that does not close the excitation gap [95, 96].

In a class D system the matrix signature of the spectral localizer (number of positive minus number of negative eigenvalues) identifies domains of different Chern number [90, 94]. As discussed by Volovik [97], the domain walls support low-lying states at energy $E \simeq \hbar v_F/\ell$ for a domain of linear dimension ℓ. These states become Majorana zero-modes in the limit $\ell \to \infty$ of a percolating domain wall. By identifying the metal-insulator transition with the percolation transition of the domain walls we construct the phase diagram in a closed system, and compare with calculations based on the thermal conduction in an open system [75, 80].

4.2 Topological landscape function

4.2.1 Lattice Hamiltonian

The Bogoliubov-De Gennes Hamiltonian for a chiral p-wave superconductor is

$$H_{\text{BdG}} = \begin{pmatrix} p^2/2m - E_F & v_\Delta(p_x - ip_y) \\ v_\Delta(p_x + ip_y) & E_F - p^2/2m \end{pmatrix}. \tag{4.1}$$

It acts on a two-component wave function $\Psi = (\psi_e, \psi_h)$, the pair potential $\propto v_\Delta$ couples the electron and hole components (filled states above the Fermi level E_F, respectively, empty states below E_F, with $E_F = \frac{1}{2}mv_F^2$ in terms of the effective mass m and Fermi velocity v_F). Because this is equal-spin pairing, we can omit the spin degree of freedom.

The particle-hole symmetry relation,

$$\sigma_x H_{\text{BdG}}^* \sigma_x = -H_{\text{BdG}}, \tag{4.2}$$
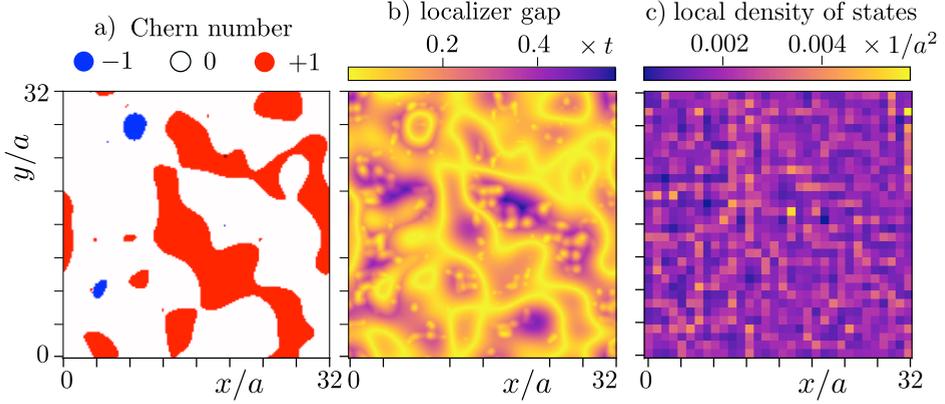
Figure 4.1. Panels a) and b) show the topological landscape function [Chern number $C(x, y)$ and localizer gap $\delta(x, y)$] in a disordered chiral p-wave superconductor (Hamiltonian (4.3), parameters $\Delta = 4t$, $\bar{\mu} = t$, $\delta\mu = 4t$, $L = 32a$, periodic boundary conditions). At these parameters the superconductor is in the thermal metal phase. Panel c) shows that the network of domain walls leaves no trace in the local density of states (integrated over the energy interval $|E| < 0.2\,t$).

places the system in symmetry class D [98]. Here σ_x is a Pauli matrix that acts on the electron-hole degree of freedom and the complex conjugation operation is taken in the real-space basis (so the momentum $\boldsymbol{p} = \hbar\boldsymbol{k} = -i\hbar\partial/\partial\boldsymbol{r}$ changes sign).

We discretize the Hamiltonian on a 2D square lattice (lattice constant a),

$$H = \begin{pmatrix} \varepsilon_k - \mu & \Delta(\sin ak_x - i\sin ak_y) \\ \Delta(\sin ak_x + i\sin ak_y) & \mu - \varepsilon_k \end{pmatrix},$$
$$\varepsilon_k = -t(\cos ak_x + \cos ak_y), \tag{4.3}$$

with the definitions $\Delta = (\hbar/a)v_\Delta$, $t = \hbar^2/ma^2$, $\mu = E_F - 2t$.

We introduce electrostatic disorder by letting the chemical potential $\mu(x, y)$ fluctuate randomly, uniformly distributed in the interval $(\bar{\mu} - \delta\mu, \bar{\mu} + \delta\mu)$. Our approach requires some degree of smoothness of the fluctuating potential on the scale of the lattice constant, in what follows we choose the same μ on the four neighboring sites $(2n, 2m)$, $(2n + 1, 2m)$, $(2n, 2m + 1)$, and $(2n + 1, 2m + 1)$.

4.2.2   Spectral localizer: open boundary conditions

The spectral localizer for a two-dimensional class D Hamiltonian with open boundary conditions is [90]

$$\mathcal{L}(x_0, y_0) = \begin{pmatrix} H & 0 \\ 0 & -H \end{pmatrix} + \kappa \Omega(x - x_0, y - y_0), \tag{4.4a}$$

$$\Omega(x, y) = \begin{pmatrix} 0 & \sigma_0(x - iy) \\ \sigma_0(x + iy) & 0 \end{pmatrix}. \tag{4.4b}$$

The Hermitian operators $\mathcal{L}$ and Ω are both 4×4 matrices, we have introduced the 2×2 unit matrix σ_0 to indicate that Ω is diagonal in the electron-hole degree of freedom. Note also that x and y are operators (which do not commute with H), while x_0 and y_0 are parameters. Our choice $\kappa = 2.5\, t$ for the scale parameter κ is explained in App. 4.A.

The operator Ω breaks the $\pm E$ symmetry of the spectrum of $\mathcal{L}$, allowing for a nonzero matrix signature: Sig $\mathcal{L}$ = number of positive eigenvalues minus number of negative eigenvalues. This even integer determines a topological invariant, the Chern number [90],

$$C(x_0, y_0) = \tfrac{1}{2} \operatorname{Sig} \mathcal{L}(x_0, y_0), \tag{4.5}$$

of a domain containing the point (x_0, y_0). Domain walls, contours across which $C(x_0, y_0)$ changes by ± 1, are contours along which $\det\{\mathcal{L}\}(x_0, y_0)$ vanishes. These can be visualized by plotting the *localizer gap*

$$\delta(x_0, y_0) = \min_n |\lambda_n|, \quad \lambda_n \text{ eigenvalue of } \mathcal{L}(x_0, y_0), \tag{4.6}$$

which vanishes along the domain walls.

4.2.3   Spectral localizer: periodic boundary conditions

Our system is a square of size $L \times L$ in the x- and y-directions. To avoid edge states and focus on bulk properties, we prefer to work with periodic boundary conditions, rather than open boundary conditions. For that purpose, following Ref. [94], the term $x \pm iy$ on the off-diagonal of Ω is replaced by the periodic combination $\sin(2\pi x/L) \pm i \sin(2\pi y/L)$. The eigenvalues of $\Omega(x - x_0, y - y_0)$ then cannot distinguish between points x_0 and $x_0 + L/2$, or between y_0 and $y_0 + L/2$. To remove this doubling, cosine terms are added on the diagonal of Ω [94],
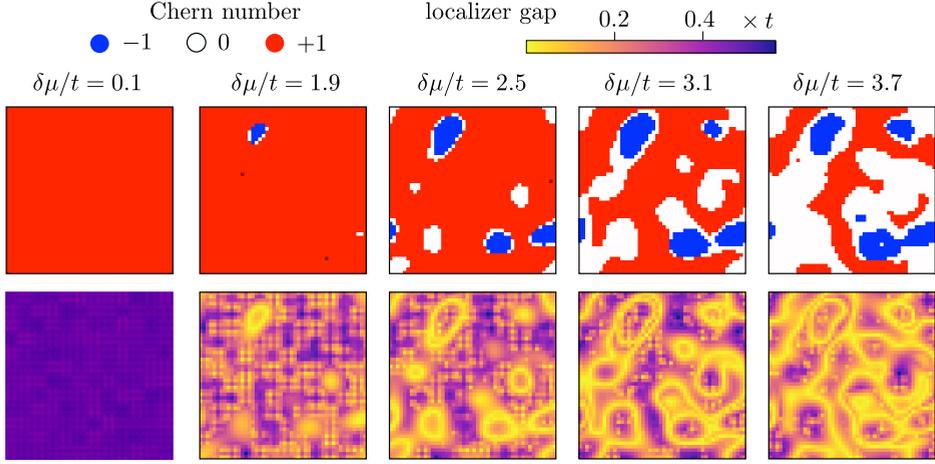
Figure 4.2. Topological landscape function (Chern number on top row, localizer gap on bottom row) for five different disorder strengths $\delta\mu$ at fixed $\bar{\mu} = 1.05\,t$ (and $\Delta = 4t$, $L = 24a$), to show the appearance of a percolating domain wall when $\delta\mu \gtrsim 3.1\,t$. These are results for a single realization of the random potential $\mu(x, y)$, only the amplitude is rescaled.

$$\mathcal{L}(x_0, y_0) = \begin{pmatrix} H & 0 \\ 0 & -H \end{pmatrix} + \kappa\Omega(x - x_0, y - y_0), \tag{4.7a}$$

$$\Omega(x, y) = \begin{pmatrix} \sigma_0[\cos(2\pi x/L) + \cos(2\pi y/L) - 2] & \sigma_0[\sin(2\pi x/L) - i\sin(2\pi y/L)] \\ \sigma_0[\sin(2\pi x/L) + i\sin(2\pi y/L)] & -\sigma_0[\cos(2\pi x/L) + \cos(2\pi y/L) - 2] \end{pmatrix}. \tag{4.7b}$$

For $|x|, |y| \ll L$ the localizers (4.4) and (4.7) coincide.

In Fig. 4.1 we show the resulting network of domain walls for a particular disorder realization (panels a and b). The topological information contained in the spectral localizer is essential: as shown in panel c, the domain walls do not show up in the local density of states near $E = 0$.

4.3   Phase diagram from percolation transition

4.3.1   Percolating domain walls

The clean system (without disorder, $\delta\mu = 0$) is a topologically trivial thermal insulator ($C = 0$) for $|\bar{\mu}| > 2t$ and a topologically nontrivial thermal insulator
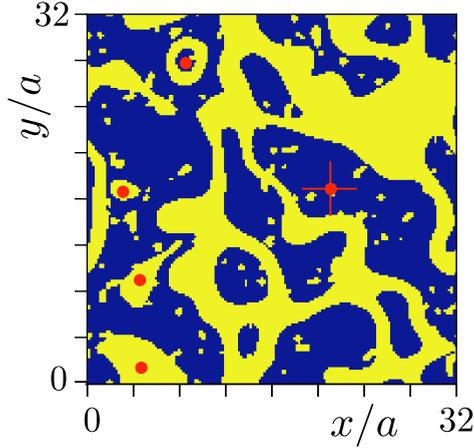
Figure 4.3. Same as Fig. 4.1b), but now the domain walls are highlighted in yellow, according to the criterion of localizer gap $\delta(\boldsymbol{r}) < 0.1\,t$. The location of the average $\bar{\boldsymbol{r}}$ ("center of mass") for each connected domain wall is indicated by a red dot. The extension ℓ of a domain wall is defined by $\ell^2 = 4\overline{|\boldsymbol{r} - \bar{\boldsymbol{r}}|^2}$. The red dot marked with a cross identifies the center of mass of a percolating domain wall ($\ell > L$).

($C = \pm 1$) for $|\bar{\mu}| < 2t$. At $\bar{\mu} = 0$ there is an insulator-to-insulator transition at which C changes sign [80]. Disorder introduces minority domains with a different Chern number than these clean values C_{clean}. See for example Fig. 4.1, where $\bar{\mu} = t$ and $C_{\text{clean}} = +1$.

The domain walls that separate regions of different Chern number support states close to the Fermi level, at energy $E \simeq \hbar v_{\text{F}}/\ell$ dictated by the requirement that the kinematic phase upon traveling once around the domain wall cancels the π Berry phase. When the extension ℓ of the largest domain wall reaches the system size L thermal conduction becomes possible near the Fermi level and the thermal insulator becomes a thermal metal. In Fig. 4.2 we show this percolation transition of topological domain walls for a single disorder realization, upon increasing the amplitude $\delta\mu$ of the potential fluctuations at fixed average $\bar{\mu}$.

To identify the percolation transition we need a computationally efficient way to measure the extension ℓ of a domain wall. We take localizer gap $\delta(x_0, y_0) < 0.1\,t$ as the criterion for a domain wall. All points $\boldsymbol{r} = (x_0, y_0)$ satisfying this criterion in a connected region belong to a single domain wall $\mathcal{D}$. We then compute the domain wall extension ℓ from the variance σ^2 of these points,

$$\ell = 2\sigma, \quad \sigma^2 = \overline{|\boldsymbol{r} - \bar{\boldsymbol{r}}|^2}, \tag{4.8}$$
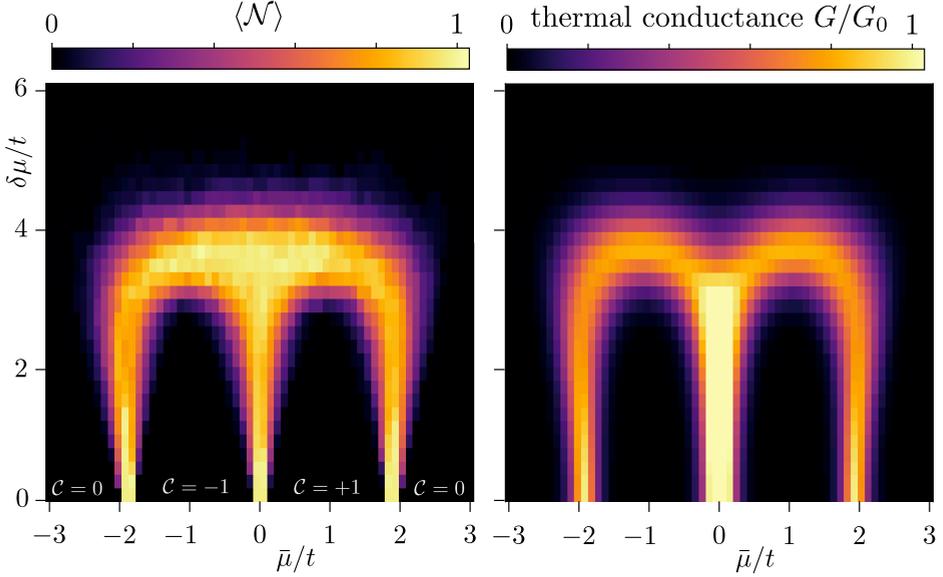
Figure 4.4. *Left panel:* Color scale plot of the average number $\langle \mathcal{N} \rangle$ of percolating domain walls, averaged over 100 disorder realizations in the chiral p-wave superconductor (parameters $\Delta = 4t$, $L = 24a$). The value of the Chern number $\mathcal{C}$ in the clean system ($\delta\mu = 0$) is indicated. *Right panel:* Dimensionless thermal conductance for the same system. The uniformly yellow bar at $\bar{\mu} = 0$ indicates $G/G_0 > 1$.

where $\overline{f(\boldsymbol{r})}$ averages a function $f(\boldsymbol{r})$ over all $\boldsymbol{r} \in \mathcal{D}$. The procedure is illustrated in Fig. 4.3. Our criterion for a *percolating* domain wall is $\ell > L$.

4.3.2   Phase diagram

The number $\mathcal{N}$ of percolating domain walls (with $\ell > L$) for a given disorder realization is averaged over the disorder. The resulting dependence of $\langle \mathcal{N} \rangle$ on the parameters $\bar{\mu}$ and $\delta\mu$ is shown in Fig. 4.4 (left panel). The region $\mathcal{N} \approx 1$ where the domain walls percolate is clearly distinguished.

The data in Fig. 4.4 is for a relatively small system ($L/a = 24$), in Fig. 4.5 we compare with a larger system. The critical disorder strength for the percolation transition is approximately scale invariant.
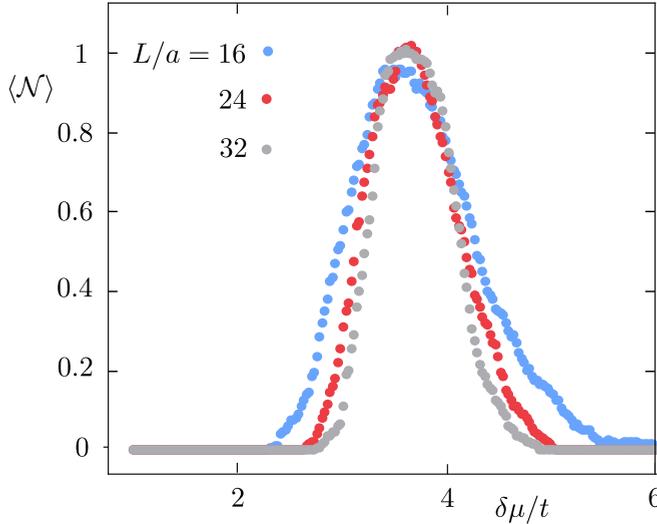
Figure 4.5. Comparison of the disorder strength dependence of the average number $\langle \mathcal{N} \rangle$ of percolating domain walls for different system sizes L. The data points are averaged over 200 disorder realizations (parameters $\Delta = 4t$, $\bar{\mu} = t$).

4.3.3   Comparison with thermal conductance

So far we have considered a closed system. If we connect leads at the two ends we can study the thermal conductance,

$$G = G_0 \operatorname{Tr} \boldsymbol{t t}^{\dagger}, \quad G_0 = \pi^2 k_{\mathrm{B}}^2 T/6h, \tag{4.9}$$

at temperature T, with $\boldsymbol{t}$ the transmission matrix at the Fermi level. The result of such a calculation, using the KWANT code [99], is also shown in Fig. 4.4 (right panel).

   If we compare with the percolation transition (left panel), we see a good quantitative agreement on the low-disorder side of the phase boundary. The high-disorder side misses a feature in the region near $\bar{\mu} = 0$, $\delta\mu = 4t$, where the thermal conductance localizes more quickly than inferred from the percolating domain walls. We are unsure about the origin of this difference. Apart from this region the agreement is quite satisfactory, without any adjustable parameters.

4.4   Conclusion

We have shown that the thermal metal phase in a model of a chiral p-wave super-conductor with electrostatic disorder has a precursor in the thermally insulating phase: The disorder produces domain walls that separate topologically distinct regions (different Chern number). The thermal metal–insulator transition is accompanied by a percolation of the domain walls across the system, providing a transport channel for Majorana fermions (charge-neutral, low-energy excitations).

To reveal the network of domains walls we have used the matrix signature of the spectral localizer [90, 94]. We turned to this topological invariant after we were not able to identify localized Majorana fermions using a variation [100, 101] of the landscape function approach that has been so succesful in the study of Anderson localization [102, 103, 104, 105]. In a sense, the matrix signature of the spectral localizer functions as a *topological* landscape function, sensitive to topological electronic properties that remain hidden in the local density of states.

It would be interesting to study the critical exponent ν for the percolation transition of the topological domain walls (the exponent that governs the divergence of the largest domain size). Classical 2D percolation has $\nu_{\text{classical}} = 4/3$. It is suggestive that a recent numerical study [80] of the divergence of the localization length at the thermal metal–insulator transition found $\nu \approx 1.35$, but the proximity to $\nu_{\text{classical}}$ may well be accidental.

Data and code availability

Our computer codes are provided in a Zenodo repository [106].

Appendices

4.A   Spectral localizer in a clean system

We have tested the ability of the spectral localizer (4.7) to identify the Chern number domains in a clean system, with a smoothly varying μ, where the boundaries are known analytically [80]:

$$
C = \begin{cases}
0 & \text{if } \mu < -2t, \\
-1 & \text{if } -2t < \mu < 0, \\
+1 & \text{if } 0 < \mu < 2t, \\
0 & \text{if } \mu > 2t.
\end{cases} \tag{4.10}
$$
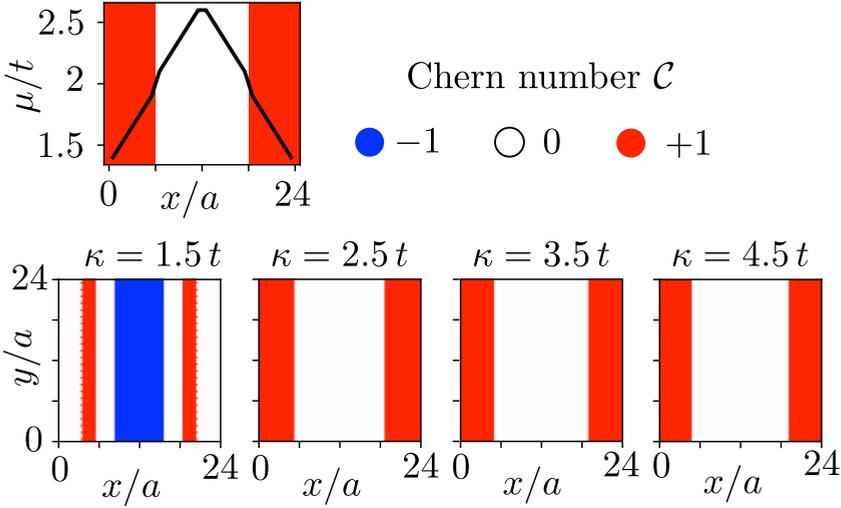
Figure 4.6. Top panel: linearly varying $\mu(x)$ (at constant $\Delta = 4t$), producing a central domain of Chern number $C = 0$, flanked by domains of $C = +1$. The domain walls are at $x/a = 6$ and $x/a = 12$. Bottom panels: Chern number domains produced by the spectral localizer, via Eq. (4.5), for different values of the scale parameter κ. We need $\kappa \gtrsim 2t$ for reliable results.

This test allows us to find a suitable value of the scale parameter κ.

Refs. [90, 94] argue that κ should be of the order of the norm of the Hamiltonian, which in our case is below $10^{-2}\,t$. We find a poor performance for such small κ, see Fig. 4.6, we need $\kappa \gtrsim 2t$ to reliably identify the domain walls. The results in the main text are for $\kappa = 2.5\,t$.

Chapter 5

Landau quantization near generalized Van Hove singularities: Magnetic breakdown and orbit networks

5.1 Introduction

Magnetic breakdown (MB) in a single Bloch band occurs when two semiclassical trajectories of quasiparticles come close to each other and quantum tunneling between them becomes possible. This situation naturally appears near usual saddle points that give rise to logarithmic van Hove singularities in the density of states [107]. In novel atomically-thin 2D materials a new family of saddle points arises, around which the dispersion is flatter than in the usual case. This leads to power-law divergences in the density of states known as high-order van Hove singularities [108, 109, 110]. In some cases, more than two trajectories approach the saddle point, creating a MB structure with a larger s-matrix size proportional to the number of trajectories. In this chapter, we present a method to calculate the precise MB s-matrix for any type of saddle point. It is based on rewriting the effective Hamiltonian in the Landau level basis, mapping the resulting algebraic problem to the 1D scattering in the quantum chain, and calculating the MB s-matrix by properly fixing semiclassical modes in the far-away region.

As was found in the 1960s in pioneering works by Pippard [111, 112, 113], and Chambers [114, 115, 116, 117], and summarized in Ref. [118], MB can
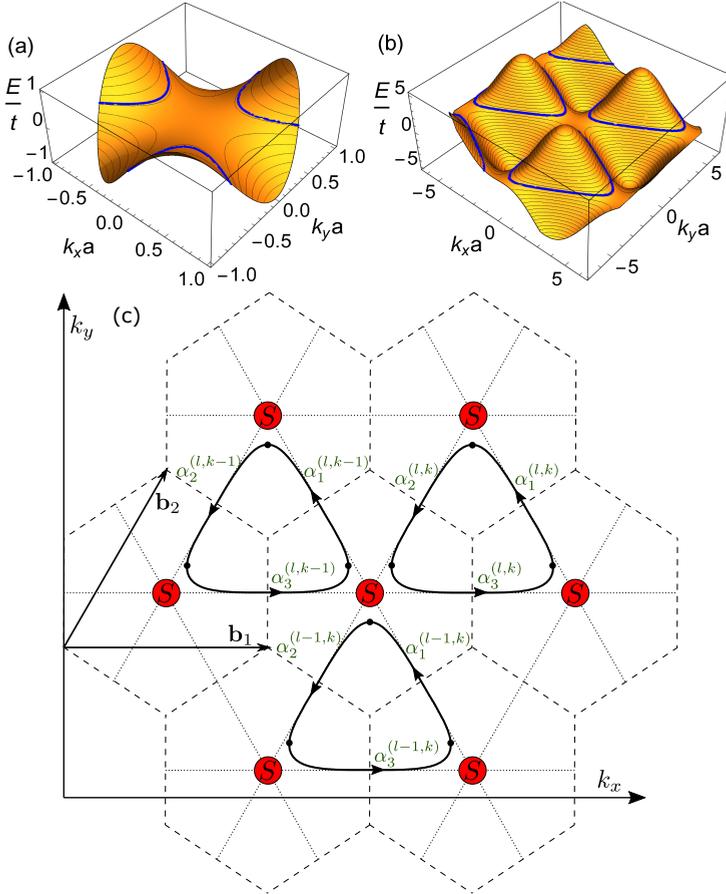
Figure 5.1. (a): Effective dispersion around Monkey saddle point in momentum space given by Eq. (5.3) with three trajectories on a single energy level coming close at the MB region (shown as blue lines). (b): Tight-binding dispersion of triangular lattice with imaginary hoppings (5.18) in which monkey saddle points connect cyclotron orbits into network. (c) Planar orbit network for dispersion (b) in rotated coordinate frame with semiclassical regions labeled by weight coefficients α [see Eq. (5.14)], and MB regions with s-matrix (red circles). Reciprocal lattice vectors $\boldsymbol{b}_i$ and highly-symmetric lines are shown.

lead to formation of coherent orbit networks composed of localized Landau level states (LLs) connected via tunneling between them. For 2D materials, the orbit network occurs in the vicinity of energy levels where the Bloch band in momentum space has saddle points located at the boundaries of the Brillouin zone (BZ). Then, tunneling between orbits in different cells of the extended BZ

scheme forms a network (see Fig.5.1). In the real space, this corresponds to a network of semiclassical cyclotron orbits, which makes LLs to be extended [111, 119, 118]. The discovery of novel 2D materials [120, 121, 122, 123] dramatically increased the number of lattice geometries in which orbit networks can be formed. Below we calculate the detailed structure of these states as well as their band dispersion. In addition, we show that such extended LLs allow for longitudinal bulk conductance in the quantum Hall bar, which strongly exceeds the standard edge conductance [124].

There are two regimes of transport that orbit networks can govern: coherent regime with quantum phase that is accumulated along the cyclotron orbits and defines the exact energy spectrum, and incoherent regime with quantum phase averaged by the presence of disorder. Below, we describe the coherent regime and corresponding observable signatures that allow us to distinguish between different types of MB that happens at saddle points that connect cyclotron orbits. In addition, we note that the mini band structure appearing due to coherent orbit networks can be linked with the topological Hall effect of electrons in skyrmion crystals [128].

Recent studies of coherent orbit networks in 1D geometry predicted a number of interesting effects such as magic zeros in Landau level spectra [129] and broadening of the Landau levels by the coupling of Fermi arcs on opposite surfaces in Kramers-Weyl semimetals [130]. Also, the predicted spectrum by 2D incoherent orbit network shows relatively good agreement with the Hofstadter butterfly for twisted bilayer graphene [131]. The scaling of miniband width appearing from orbit networks with magnetic field was obtained for square lattice [132, 133] and graphene [134].

The semiclassical equations of motion for the electron in crystal under external weak magnetic field are given by the Lorentz force [135, 136]

$$\hbar \partial_t \boldsymbol{k} = -c^{-1} e (\boldsymbol{v}_k \times \boldsymbol{B}). \tag{5.1}$$

with usual velocity replaced by group velocity found from the dispersion law $\boldsymbol{v}_k = \frac{1}{\hbar} \partial_{\boldsymbol{k}} E(\boldsymbol{k})$ that depends on wave vector $\boldsymbol{k}$. Here, we consider 2D crystals placed in perpendicular magnetic field along the z-direction $\boldsymbol{B} = (0, 0, B)$. Equation (5.1) restricts quasiparticles to move only along the lines of constant

---

[1]For the Hamiltonian written in gauge-invariant coordinates $H = A\Pi_x^n + B\Pi_x^s \Pi_y^m = Ak_x^n + Bk_x^s \left(-\frac{i}{l_B^2} \frac{\partial}{\partial k_x} \right)^m$ it is possible to introduce a change of variables $q_x = k_x l_B^{\frac{2m}{m+n-s}}$, that would convert it to $l_B = 1$ Hamiltonian with additional factor $H = l_B^{\frac{2mn}{m+n-s}} \left[Aq_x^n + Bq_x^s \left(-i \frac{\partial}{\partial q_x} \right)^m \right]$. This factor should be used to obtain energy dependence of S-matrix for any magnetic field value.
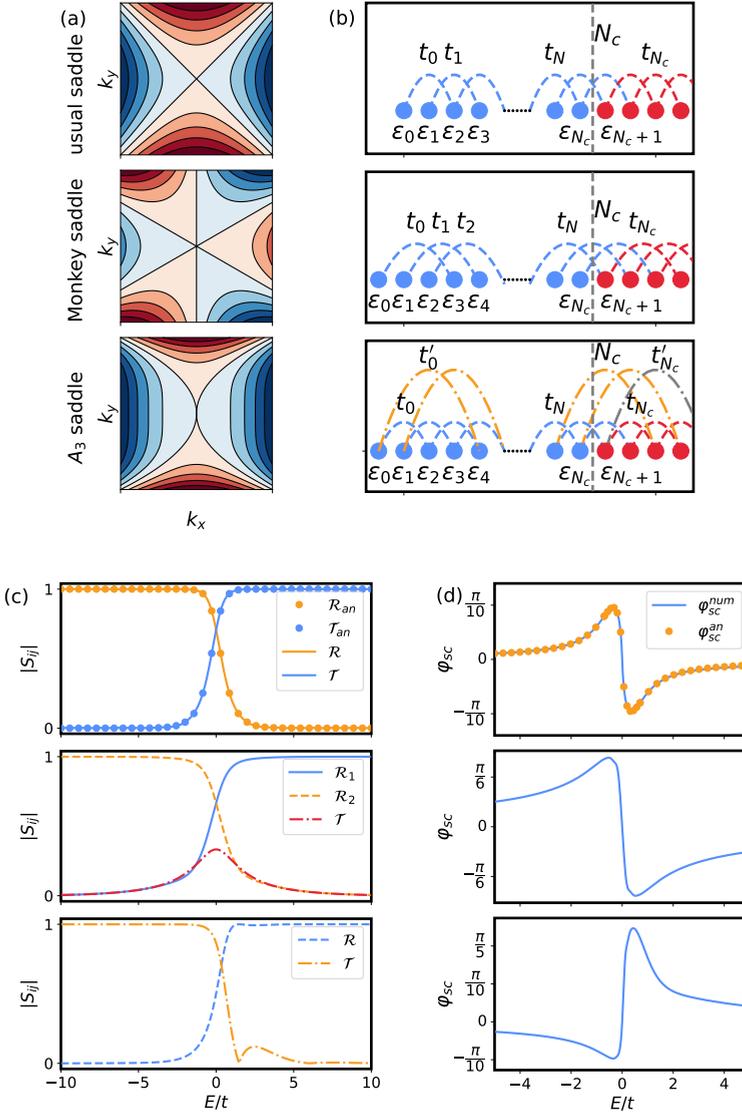
Figure 5.2. (a) The geometry of usual, Monkey and A_3 saddle points with equi-energy contours in k−space. (b): The corresponding 1D chains after mapping. The cut-off region with plane wave approximation is shown as a set of red sites with equal hopping parameters. (c) The absolute value of s-matrix elements (reflection - $\mathcal{R}_i$ and transmission - $\mathcal{T}$). (d): The basis-independent scattering phase calculated as $\arg(\det[S])$. For the usual saddle point (top panels in (c), (d)) we also show the comparison with exact analytic solution [125, 126, 127] marked by dots that perfectly agrees with the results obtained with our approach. In (c), (d) we set $l_B = 1$ and for any other magnetic field the results can be obtained by proper rescaling of energy.[1]

energy in momentum space. In Fig. 5.1 such lines are shown in the vicinity of the monkey saddle point and in the dispersion of the tight-binding model introduced below in Eq.(5.18). Before proceeding to MB, we note that after integration over time in Eq. (5.1) one finds that the trajectory in real space is rotated by angle $\pi/2$ compared to the $E(\boldsymbol{k}) = $ const line in k-space and its size is rescaled by squared magnetic length [136, 137]:

$$k_x = -\frac{y - y_0}{l_B^2}, \ \ k_y = \frac{x - x_0}{l_B^2}, \ \ l_B = \sqrt{\frac{\hbar c}{eB}}. \tag{5.2}$$

In what follows, we set $\hbar = c = 1$. Magnetic field is considered as weak if magnetic length is much larger than the lattice constant of the crystal, $l_b \gg a$.

5.2 Magnetic breakdown at generalized Van Hove singularity

We now focus on the detailed description of tunneling that takes place in the vicinity saddle point in dispersion due to magnetic breakdown. The saddle points are defined as points where the gradient of dispersion vanishes, $\nabla_{\boldsymbol{k}} E(\boldsymbol{k}) = 0$. As was shown in Ref. [108], they can be further classified as usual or high-order depending on the "flatness" of dispersion around that point. More formally, the usual type corresponds to non-vanishing determinant of Hessian matrix $\mathcal{D}_{ij} = \partial_{k_i} \partial_{k_j} E(\boldsymbol{k})$ for dispersion, while the high-order ones have zero determinant and optionally zero Hessian itself. They could be further classified into many types depending on the underlying symmetry point group, see Refs. [109, 110]. Below, we show that our approach works for all possible saddle points. The magnetic breakdown happens because several constant energy lines in k-space come close to each other near the saddle point, see Fig. 5.1(a). Thus, the tunneling probability between them becomes of order of one, and therefore we have to properly solve the scattering problem in the corresponding region. The complication arises due to the fact that typical dispersion around the saddle point has high powers of polynomials in $\boldsymbol{k}$, for example

$$E_M(\boldsymbol{k}) = -ta^3(k_x^3 - 3k_x k_y^2) \tag{5.3}$$

for the monkey saddle. Here t is a constant with dimension of energy. Generally, it is not possible to solve a Schrödinger equation for such a Hamiltonian analytically to match it with plane-wave solutions away from the MB region. The only

available closed form solution of such kind exists for the usual saddle point [125, 127], a partial case of A_{2n-1} points,

$$E_{log}(\boldsymbol{k}) = ta^2(k_x^2 - k_y^2), \ E_{A_{2n-1}}(\boldsymbol{k}) = t(a^2 k_x^2 - (ak_y)^{2n}), \qquad (5.4)$$

with $n = 1, 2, \dots$. But we show that our semi-numerical method efficiently solves the Schrödinger equation up to any precision and enables us to find the s-matrix.

To introduce our method, we use the cylindrical gauge for vector potential $A = \frac{B}{2}(-y, x, 0)$ and make use of the oscillator-type basis for Landau levels $|n\rangle$, with their coordinate representation given by:

$$\psi_n(x, y) = \left(\frac{\partial}{\partial w} - \frac{w^*}{4l_B^2}\right)^n w^n e^{-|w|^2/4l_B^2}, \quad w = x + iy. \qquad (5.5)$$

Using Landau level basis[2], the effective Hamiltonian of the saddle point in magnetic field that is written in terms of canonical momenta $\Pi_i = k_i + eA_i$ can be expressed in terms of ladder operators by using the replacement:

$$k_x \to \Pi_x = \frac{\hat{a} + \hat{a}^\dagger}{\sqrt{2}l_B}, \ k_y \to \Pi_y = \frac{i(\hat{a} - \hat{a}^\dagger)}{\sqrt{2}l_B}, \qquad (5.6)$$

with standard commutation relation $\left[\hat{a}, \hat{a}^\dagger\right] = 1$. In the simplest case of the usual saddle point, we find

$$H_{\log} = ta^2 l_B^{-2}[\hat{a}^2 + \left(\hat{a}^\dagger\right)^2]. \qquad (5.7)$$

Here, we rescaled energy by t and set $l_B = a = 1$, which can be later restored by rescaling energy dependence of the s-matrix. The more complicated example of monkey saddle (5.3) with mixed $k_x k_y^2$ product requires a symmetrization procedure to make the Hamiltonian Hermitian in terms of ladder operators. In the general case, different symmetrizations of particular polynomial Hamiltonian give different results for the lower order terms due to non-trivial commutation relations. To uniquely fix the symmetrization procedure, we expand the tight-binding Hamiltonian of the underlying lattice with assumption that momenta operators do not commute. For the Monkey saddle after simplification this reads [see Appx.5.A]

$$H_M = -\frac{ta^3 l_B^{-3}}{2\sqrt{2}} \left[\left(\hat{a} + \hat{a}^\dagger\right)^3 + 3\left(\hat{a} - \hat{a}^\dagger\right)\left(\hat{a} + \hat{a}^\dagger\right)\left(\hat{a} - \hat{a}^\dagger\right)\right]. \qquad (5.8)$$

---

[2]We note that we take Landau basis with $m_z = 0$. For the problems in empty space different m_z states are trivially degenerate. The problem at hand does not mix different m_z states.

We note that in more general case of higher polynomial Hamiltonians one might find different symmetrization results depending on the lattice. If the tight-binding Hamiltonian is not known exactly, all possible symmetrizations that give different expressions in terms of ladder operators should be analyzed.

Next, we explain how to obtain the scattering matrix that describes magnetic breakdown around a saddle point. We start by noting that the exact solution of the Schödinger equation $H\Psi = E\Psi$ with $\Psi = \sum_{n=0}^{\infty} \phi_n|n\rangle$ yields a set of recursive equations. For a usual van Hove singularity, we find

$$E\varphi_0 - \sqrt{2}\phi_2 = 0, \quad E\phi_1 - \sqrt{6}\phi_3 = 0,$$
$$E\phi_n - \sqrt{n(n-1)}\phi_{n-2} - \sqrt{(n+1)(n+2)}\phi_{n+2} = 0. \tag{5.9}$$

Recursive equations for other saddle points are derived in the Appendix 5.A. We note that a set of recursive equations can be mapped onto a 1D tight-binding problem: the term multiplying φ_n corresponds to an on-site potential for the site with index n, while the terms involving φ_m with $m \neq n$ represent the tight-binding hopping parameters that connect the n-th site to the m-th site. By imposing truncation at large index $n = N_c$ and replacing all remaining equation with those where $n = N_c$, we obtain a natural mapping to N_c-site 1D chain of atoms connected to a translationally invariant semi-infinite lead, shown in Fig.5.2(b). Then, we obtain the s-matrix using the propagating modes of the lead at energy E, with the number of scattering states corresponding to the number of semiclassical orbits coming close at the MB region.

However, the obtained s-matrix is in the LL basis. To transform the s-matrix into basis of modes with a definite angle in momentum space, we use the creation ladder operator

$$a^\dagger \sim k_x + ik_y \equiv ke^{i\phi_k}, \tag{5.10}$$

where ϕ_k is the angle in momentum space. Hence, performing a basis transformation on the propagating modes in semi-infinite leads to a basis where $a^\dagger$ is diagonal converts the obtained s-matrix into a physical one. The technical details of this procedure for the usual and Monkey saddle are discussed in the Appendix 5.A. The chirality and consequent absence of backscattering of the states with definite angle, that are spatially separated, ensures the unique definition of the physical s-matrix.

For some saddle points the asymptotic modes at large momenta are indistinguishable by their angle in momentum space. In this case, we cannot apply our procedure of transforming the s-matrix into a physical basis. An example of such

a saddle point is A_{2n-1} described by Eq. (5.4). For this saddle point, the angle of trajectory in momentum space with respect to the x-axis tends to zero as the wave number tends to infinity, see the bottom panel of Fig.5.2(a). We resolve this by introducing angle-fixing regularization, achieved through the inclusion of sufficient amount of sub-leading terms in the effective Hamiltonian

$$E'_{A_{2n-1}}(\boldsymbol{k}) = t \left(a^2 k_x^2 - a^{2n} (k_y^{2n} - \beta k_x^{2n}) \right), \ n \geq 2, \tag{5.11}$$

where we use the $\beta > 0$ constant as a regularization parameter and this parameter defines angles far away from the scattering region, not playing a role in the vicinity of the saddle point. We choose the truncation number N_c such that the leading terms strongly dominate in effective 1D tight-binding equations and the mode separation into the angle basis can be done with good precision: $t_{N_c+1}^{max} \gg E, \dots$. Physically, this corresponds to taking the region where the scattering between modes with different angles is absent.

To demonstrate our method, we numerically solve for the scattering matrix using Kwant code [99, 138]. We show our results for the absolute values of the transmission and reflection elements of the s-matrix and scattering phases in panels (c) and (d) of Fig.5.2. All these elements are gauge-invariant and independent of incoming and outgoing basis modes selection. In the case of usual van Hove singularity, it demonstrates perfect agreement with analytic expressions [see [127], Appx. 5.B]. For the A_3 saddle point, we find a nontrivial behavior of transmission coefficients shown in bottom row in Fig.5.2(c). The presence of zeros in the transmission coefficient signifies the complete reflection of a quasi-particle moving along a cyclotron trajectory at that specific energy. Consequently, this phenomenon results in the effective reduction of orbit network to a single cell. The manifestation of this effect is demonstrated below by the narrowing of the mini-band width in the spectrum and the corresponding reduction in bulk conductance.

5.3   Coherent orbit network

With the complete description of MB at hand, we now propose a transport setup which would probe the features of the high-order saddle points. Since our goal is to distinguish energy dependence of both scattering amplitude and phase of MB at different saddle points, we use the coherent orbit networks that appear when the saddle points are placed at the edge of the BZ. Such coherent orbit networks were widely discussed in literature in the late 1960s [111, 119, 118], but the
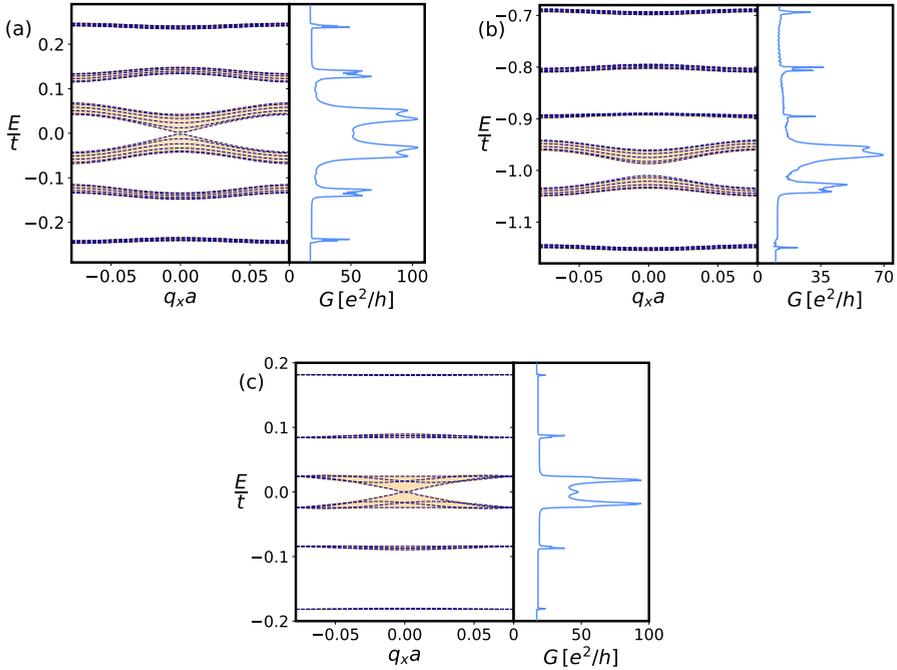
Figure 5.3. Comparison of Landau mini-band spectrum with longitudinal conductance in the quantum Hall bar for three systems: (a), (b) square lattice with usual (hopping $t_2 = 0$ in Eq. (5.16)) and A_3 ($t_2 = t/4$) saddle points, and (c) triangular lattice with imaginary hoppings that contain Monkey saddles. LL mini-bands (orange solid lines) obtained from tight-binding simulations are compared with solutions of spectral equations (5.17),(5.19) for a set of $q_y a$ (blue dashed lines). The flux value per unit cell was taken equal to $\Phi = 1/40 \, \Phi_0$ and the width of the Hall bar was $W = 320a$. For the spectrum calculation a periodic boundary condition was imposed. A single period of Landau mini-band oscillation is shown and corresponds to $\sqrt{\Phi/\Phi_0}$ part of BZ. The width of conductance peaks measures the Landau mini-band broadening. In panel (b) the miniband around $E \approx -0.8t$ is wider than the one at $E \approx -0.9t$ due to the first zero of transmission coefficient at the A_3 saddle point (see Fig. 5.2(c)).

absence of experiments with 2D atomically-thin crystals limited discussion to
the simplest geometries, such as weak perturbative potential with square lattice
geometry. Here, we use the same approach of magnetic translation symmetry
groups and describe the orbit networks that are connected via usual as well
as high-order saddle points. As it is clear from the constant energy curves in
the spectrum in the extended BZ scheme (see Fig. 5.1(b)), the orbits networks
in k space have perfect periodicity and thus should be periodic in r space.
However, in the presence of external magnetic field, the translation operators of
the lattice $\hat{T}_{\bm{R}_i} = \exp\{\bm{\nabla}_r \bm{R}_i\}$, with $\bm{R}_i$ being a basis vector, should be replaced
by magnetic translation operators [118], which up to phase factor are equal to
$\hat{T}^M_{\bm{R}_i} = \exp\{(\bm{\nabla}_r + ie(\bm{A}(\bm{R}_i) + \bm{R}_i \times \bm{B}))\,\bm{R}_i\}$. The corresponding operators define
a magnetic unit cell. To obtain a closed set of equations for the orbit network,
we should restrict the value of magnetic flux per unit cell of the lattice to be a
rational number

$$\Phi = B\,|\mathbf{R}_1 \times \mathbf{R}_2| = B\frac{(2\pi)^2}{|\mathbf{b}_1 \times \mathbf{b}_2|} = \frac{q}{p}\Phi_0, \ \ \Phi_0 = \frac{h}{e}. \tag{5.12}$$

Here, $\bm{b}_i$ are the basis vectors of reciprocal lattice. In the further calculations,
we restrict ourselves to the case of $q = 1$. This relation is equivalent to setting
magnetic unit cell to the integer number p of lattice unit cells. Now we are ready
to proceed with defining a basis of semi-classical wave functions on the links of
networks. These are Zilberman-Fischbeck (ZF) wave functions [139, 118, 127],
written using the WKB-type approximation far from scattering region. The ZF
functions are expressed in a gauge-invariant coordinate space with replacement
$\Pi_x \to k_x$ and $\Pi_y \to -il_B^{-2}\partial_{k_x}$. Since the scope of this chapter is limited by the
linear effects in magnetic field, we use the first order expansion of ZF functions
with $a^2/l_B^2 \ll 1$:

$$\Psi_{ZF}(k_x) = \left|\frac{\partial E(\bm{k})}{\partial k_y(k_x)}\right|^{-\frac{1}{2}} \exp\left[-il_B^2 \int_{k_{x,0}}^{k_x} k_y^E(k_x)\,dk_x\right]. \tag{5.13}$$

Here $k_y^E(k_x)$ stands for the solution of constant energy contour equation $E(k_x, k_y^E(k_x)) = E$. The full wave function of the orbit network state is composed as a weighted
superposition of the Ψ_{ZF} wave functions in different unit cells:

$$\Psi(k_x) = \sum_{k,l}^{\infty} e^{il_B^2[k_x l b_{2,y} - \frac{l^2}{2}b_{2,x}b_{2,y}]} \sum_j \alpha_j^{(l,k)} \Psi_{ZF}^j\left(k_x - kb_{1,x} - lb_{2,x}\right).$$

$$\tag{5.14}$$

In this expression, each weight coefficient $\alpha_j^{(l,k)}$ contains two cell indices l, k as well as a unique index j corresponding to the different parts of the orbit between scattering points inside single cell of the network. The example of this notation is shown in Fig. 5.1. Due to periodicity of the network, the solutions have the form of Bloch waves $\alpha_j^{(l,k)} = \alpha_j e^{i(p_k k + p_l l)}$. The magnetic translation group restricts the allowed values of $p_{l,k}$ to particular dependence on translation operator $\hat{T}_{\mathbf{R}_i}^M$ eigenvalues $\mathbf{q}$: $p_l = -l_B^2 \left(q_x b_{2,y} - q_y b_{2,x} \right)$, $p_k = l_B^2 q_y K_{1,x}$ [see Appx. 5.B]. Next, we use the S-matrices obtained above to couple the ZF solutions in the neighboring cells. By noting that ZF functions from Eq. (5.13) correspond to the modes with proper angles, we can straightforwardly insert parameters of the s-matrix into the system of equations, and write it in the form of a Ho-Chalker operator [140]:

$$\hat{S}_{HC}(E, \mathbf{q})\boldsymbol{\alpha} = 0. \tag{5.15}$$

While substituting the s-matrix, we subtracted the difference in dynamical phases of modes with defined angles and ZF functions (5.13) at given energy. Such a difference appears due to the fact that in geometry of the scattering problem one assumes semiclassical ZF solutions with the phase fixed at infinity, while in the orbit network ZF function phase is fixed at particular point inside the network unit cell.

5.4   Landau minibands

The nonlinear eigenvalue problem for the Ho-Chalker operator (5.15) can be rewritten in the form of spectral equation $\det \hat{S}_{HS}(E, \mathbf{q}) = 0$ for a given lattice model [see Appx. 5.B]. Below we demonstrate this for square and triangular lattice, and show that the MB s-matrix calculated above plays a key role in definition of the properties of coherent orbit network. In the case of square lattice with only first and third NN hoppings taken into account,

$$H_{sq}(\mathbf{k}) = -2 \sum_{i=x,y} (t \cos k_i a + t_3 \cos 2k_i a), \tag{5.16}$$

the spectral equation is:

$$\cos\left(\frac{l_B^2 \mathcal{A}(E)}{2} - \varphi_{sc}\right) = \pm \mathcal{T} \mathcal{R} \left[\cos\left(l_B^2 q_1 b_{2,y}\right) + \cos\left(l_B^2 q_2 b_{1,x}\right)\right]. \tag{5.17}$$

Here, $\mathcal{A}(E)$ is the area enclosed by the constant energy curve in momentum space. The elements of the s-matrix, denoted as $\mathcal{R}$-reflection, $\mathcal{T}$-transmission and $\varphi_{sc} = \arg(\det S)$ is the scattering phase, are shown in Fig. 5.2. For such a lattice Hamiltonian, the connection of orbits happens via usual van Hove singularity at the X-point of BZ for $t_3 = 0$ or via high-order van Hove singularity of A_3 type for $t_3 = t/4$. In the case of the triangular lattice with imaginary hoppings, the dispersion is

$$H_{tr}(\mathbf{k}) = 2t\left(\sin k_x a - \sin\frac{k_x - \sqrt{3}k_y}{2}a - \sin\frac{k_x + \sqrt{3}k_y}{2}a\right). \qquad (5.18)$$

The monkey saddle (see Fig. 5.1) connects orbits from different cells into a network. The corresponding spectral equation is

$$\cos\left(\frac{l_B^2 \mathcal{A}(E) - \varphi_{sc}}{2}\right) = \mathcal{T}\left[\cos\left(l_B^2\left[q_1 b_{2,y} + q_2\left(b_{1,x} - b_{2,x}\right)\right] - \frac{\pi p}{2}\right)\right.$$
$$\left. + \cos\left(l_B^2 q_2 b_{1,x} - \frac{\pi p}{2}\right) + \cos\left(l_B^2\left[q_1 b_{2,y} - q_2 b_{2,x}\right] - \frac{\pi p}{2}\right)\right]. \quad (5.19)$$

The left-hand side of each spectral equation, as defined in (5.17) and (5.19), yields the conventional flat Landau levels when equated to zero. On the other hand, the nonzero right-hand side converts Landau levels into minibands. The width of these minibands is determined by the van Hove singularity, the s-matrix transmission coefficient, and the lattice-specific dispersion. To explore this behavior, we numerically solve [138] the spectral equations for different values of q_x and for a small set of q_y. The resulting miniband structures are depicted by the blue dashed lines in Fig. 5.3, showing both the width and internal structure of analytic spectrum of a mini-bands. The spectrum obtained from a tight-binding simulations [138, 99] is shown as orange lines filling the corresponding regions and demonstrates excellent agreement with the semi-classical predictions. For our analysis, we utilized a narrow Hall bar geometry with periodic boundary conditions, having a width several times larger than the magnetic unit cell. That width is already enough to have many bulk conducting states inside the orbit network.

5.5   Conclusion

The appearance of oscillating dispersion and broadening of Landau levels due to orbit networks is expected to be manifested in the transport experiments such

as Shubnikov-de-Haas oscillations or high-frequency magnetic breakdown oscillations [141, 142, 143, 144, 145, 130]. As the most pronounced signature, we present a calculation of longitudinal conductance in two-terminal Hall bar geometry. Typically, such conductance is governed by edge states [124] and is strongly suppressed. As it is shown in the right part of each panel in Fig. 5.3, the dispersive Landau mini-bands induce bulk conductance that is much larger than background edge conductance. We compared the spectrum for the lattices with periodic boundary condition with the conductance shape in finite size systems for the same values of magnetic field. The width of the peaks in the conductance agrees with the broadening of Landau mini-bands, thus providing a tool for estimation of the tunneling probabilities $\mathcal{T}$ for MB s-matrix at the saddle point. In addition, we note that the specific property of the A_3 saddle point with zero transmission coefficient [see Fig.5.2(c)] leads to a much smaller conductance peak at corresponding chemical potential comparing to other peaks, shown in Fig.5.3(b).

To give an estimate of magnetic field required for the experiment, we use an estimate of magnetic length $l_B \approx 26\,\mathrm{nm}/\sqrt{B[\mathrm{T}]}$ with typical experimental values of magnetic field $B \sim 10\,T$ [146], which gives $l_B \approx 10\,\mathrm{nm}$. The broadening of Landau miniband becomes significant compared to the hopping parameter (see Fig. 5.3) and larger than disorder broadening for magnetic fluxes around $\Phi = 10^{-2}\Phi_0$ per lattice unit cell. Thus, it requires lattice constant to be of the order of $a \sim l_B\sqrt{2\pi\Phi/\Phi_0} \sim 2.5\mathrm{nm}$. Such an estimate shows that one requires extremely high magnetic field to measure such effects in conventional systems, such as highly doped monolayer graphene [147]. But, such lattice constants are typical for the modern artificial lattices [148] as well as for Moiré materials such as twisted bilayer graphene [149, 150, 151]. In addition, we point out that the method of solving the MB problem developed above can be applied for the systems with spin-orbit coupling such as Moiré bilayer transition-metal dichalcogenides [152]. The structure of the orbit network might be visualized by injecting the current at proper chemical potential level into the system via narrow lead. The picture of current density distribution is expected to follow the pattern of orbit network shown in Fig. 5.1 and might be probed by STM-type microscopy techniques [153, 154].

Appendices

5.A   Magnetic breakdown near usual and high-order saddle points

In this section, we describe in detail the way how we obtain the scattering matrix for the quasiclassical wave functions of WKB type that approach the saddle point of any topology in 2D dispersion. After introducing the key notation of Landau level basis in axial gauge and oscillator basis, we describe the full algorithm on example of usual saddle point that leads to logarithmic van Hove singularity (vHs). For such vHs the analytic S-matrix is known from exact solution of Schrödinger equation [125, 126, 127] and can be compared with the results of our calculation. Next, we extend this algorithm to a number of high-order saddle points that were discussed in classifications in Refs. [109, 110]. In addition to comparing technical subtleties of realizations and related physical effects, we also compare the results with the simplest quasiclassical calculations of tunneling probability.

5.A.1   Oscillator basis of Landau levels and formulation of problem in terms of ladder operators

We use the axial gauge for vector potential $A = \frac{B}{2}(-y, x, 0)$ and insert this into the effective model of quasiparticle with dispersion $\varepsilon(k_x, k_y)$, which is expressed in terms of canonical momenta with standard commutation relation

$$H = \varepsilon(\Pi_x, \Pi_y), \quad \Pi_i = k_i + eA_i, \quad [\Pi_x, \Pi_y] = -il_B^{-2}. \quad (5.20)$$

Next, we introduce the ladder operators,

$$\Pi_x = \frac{1}{\sqrt{2}l_B}\left(\hat{a} + \hat{a}^\dagger\right), \quad \Pi_y = \frac{i}{\sqrt{2}l_B}\left(\hat{a} - \hat{a}^\dagger\right), \quad [\hat{a}, \hat{a}^\dagger] = 1, \quad (5.21)$$

with $l_B = \sqrt{\frac{\hbar}{eB}}$ being the magnetic length. These operators are analogous to the ladder operators for the quantum harmonic oscillator. The basis of corresponding number operator $a^\dagger a|n\rangle = n|n\rangle$ with integer Landau level index $n \geq 0$ can be used to represent any polynomial Hamiltonian $H = \varepsilon(\Pi_x, \Pi_y)$ as a matrix. The eigenstates $|n\rangle$ in the coordinate basis are given by

$$|n\rangle = \psi_n(x, y) = \left(\frac{\partial}{\partial w} - \frac{w^*}{4l_B^2}\right)^n w^n e^{-|w|^2/4l_B^2}, \quad w = x + iy, \quad (5.22)$$

and the matrix elements of ladder operators are

$$\langle n|\hat{a}|m\rangle = \sqrt{m}\delta_{n,m-1}, \quad \langle n|\hat{a}^\dagger|m\rangle = \sqrt{m+1}\delta_{n,m+1}. \tag{5.23}$$

Next, we use this notation to obtain matrix representation of the effective Hamiltonians near different saddle points.

5.A.2 Magnetic breakdown S-matrix for the usual saddle point

The effective Hamiltonian in the vicinity of the usual saddle point in k-space of 2D band is given by

$$H_{\log} = \alpha k_x^2 - \beta k_y^2. \tag{5.24}$$

Below, we set $\alpha = \beta = 1$ for simplicity. Using the notation of ladder operators and oscillator basis, we rewrite this Hamiltonian in magnetic field as follows

$$H_{\log} = \frac{1}{2l_B^2}\left[\left(\hat{a}+\hat{a}^\dagger\right)^2 + \left(\hat{a}-\hat{a}^\dagger\right)^2\right] = \frac{\hat{a}^2 + \left(\hat{a}^\dagger\right)^2}{l_B^2}. \tag{5.25}$$

In the oscillator basis, this Hamiltonian is represented by the following matrix:

$$H_{log} = \frac{1}{l_B^2}\begin{pmatrix} 0 & 0 & \sqrt{2} & 0 & 0 & 0 & 0 & \dots \\ 0 & 0 & 0 & \sqrt{6} & 0 & 0 & 0 & \dots \\ \sqrt{2} & 0 & 0 & 0 & 2\sqrt{3} & 0 & 0 & \dots \\ 0 & \sqrt{6} & 0 & 0 & 0 & 2\sqrt{5} & 0 & \dots \\ 0 & 0 & 2\sqrt{3} & 0 & 0 & 0 & \sqrt{30} & \dots \\ 0 & 0 & 0 & 2\sqrt{5} & 0 & 0 & 0 & \sqrt{N(N+1)} \\ 0 & 0 & 0 & 0 & \sqrt{30} & 0 & 0 & \dots \\ \dots & \dots & \dots & \dots & \dots & \sqrt{N(N+1)} & \dots & \dots \end{pmatrix}.$$

$$\tag{5.26}$$

As a result, we transformed the problem into an eigenvalue equation, where the eigenstates are superpositions of oscillator basis states:

$$H\Psi = E\Psi, \quad \Psi = \sum_{n=0}^{\infty} \phi_n|n\rangle. \tag{5.27}$$
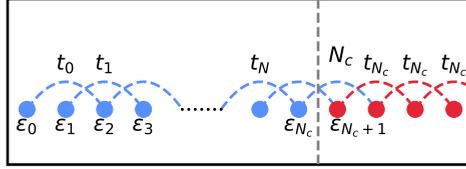
Figure 5.4. Effective 1D tight-binding model that represents the system of equations (5.28) with asymptotic truncation after Landau level index $n > N_c$.

We then reformulate this eigenvalue equation as a coupled set of recursive algebraic equations:

$$E\phi_0 - \sqrt{2}\phi_2 = 0,$$
$$E\phi_1 - \sqrt{6}\phi_3 = 0,$$
$$E\phi_2 - \sqrt{2}\phi_0 - 2\sqrt{3}\phi_4 = 0,$$
$$E\phi_3 - \sqrt{6}\phi_1 - 2\sqrt{5}\phi_5 = 0,$$
$$\cdots$$
$$E\phi_n - \sqrt{n(n-1)}\phi_{n-2} - \sqrt{(n+1)(n+2)}\phi_{n+2} = 0. \qquad (5.28)$$

The exact iterative solution of (5.28) quickly becomes very cumbersome because of the complexity of coefficients in the recursive relation. Thus, to solve this system of equations and those that shall appear for more complicated saddle points, we introduce a truncation scheme. After the large value of index $n > N_c$ we replace the index n by N_c in the coefficients of recursive relation. This procedure can be schematically illustrated by Fig. 5.4, where we represent solution coefficients φ_n as sites, coefficients of Hamiltonian that appear in recursive relations as hopping terms and onsite potentials, respectively. This correspondence allow us to solve the system of equations as an effective 1D tight-binding model of a chain. The introduced cut-off at large N_c separates the scattering region from the translationally-invariant region with simplified coefficients. We note that there are two disconnected sets of equations, and this fact manifests the presence of two linearly-independent solutions in the original problem.

After setting up the correspondence between effective Hamiltonian in the saddle point and 1D tight-binding model with two decoupled chains, we proceed with finding the S-matrix of magnetic breakdown. The procedure of truncation described above allows us to match the asymptotic solutions at high Landau level

indices $n > N_c$ with exact solution at lower indices $n \leq N_c$. We solve the scattering problem numerically using the Kwant package for tight-binding simulations [99]. However, the scattering modes, matched solutions and S-matrix obtained from numerical simulation are given in the oscillator basis. Thus, we perform an additonal procedure to link them with quasiclassical wave functions of cyclotron trajectories and corresponding magnetic breakdown S-matrix. To establish this link, we solve the problem analytically in the translationally-invariant region with $n > N_c$.

The eigenmodes of the infinite lead composed of two identical chains are given by two Bloch wave functions with identical degenerate band dispersions. These eigenmodes and their eigenenergies are given by the following expressions in the basis of two atoms per unit cells:

$$\Psi_1(l) = \frac{1}{M} \sum_{n=N_c+1}^{\infty} e^{-2iln}|2n\rangle, \quad \Psi_2(l) = \frac{1}{M} \sum_{n=N_c+1}^{\infty} e^{-2iln}|2n+1\rangle,$$

$$\varepsilon_{1,2}(l) = -E + 2t_{N_c} \cos 2l. \quad (5.29)$$

Here, the length of the unit cell is 2 because the coupling is between second neighbor oscillator basis states only. The normalization constant M can be omitted in next calculations as it does not alter the final result. We note that the modes defined above are in the basis of oscillator states, with corresponding indices depicted as sites, and the momentum l is defined in the corresponding reciprocal space. To obtain the S-matrix of physical modes, we have to establish connection between these modes and asymptotic modes far from the saddle point in k-space in the quasiclassical region (see Fig. 2(a) in the main text). To establish this connection, we notice that the modes in quasiclassical region are classified by their corresponding angle in momentum space: incoming modes correspond to angles $\pi/4$ and $5\pi/4$ for energies $E > 0$, while outgoin modes are at $3\pi/4$ and $7\pi/4$ angles. We find the modes in angle basis by diagonalizing the creation ladder operator by noting that

$$\hat{a}^\dagger = \frac{l_B}{\sqrt{2}}(\Pi_x + i\Pi_y) \underset{B\to 0}{\to} k_x + ik_y = ke^{i\phi_k}. \quad (5.30)$$

The limit of zero magnetic field is used only to point out that the ladder operator $\hat{a}^\dagger$ allows one to classify propagating modes in lead according to the asymptotic angles of scattering modes in MB region that follow constant energy curves in saddle point dispersion. In other words, in the basis of eigenmodes of $a^\dagger$ operator, the phase of eigenvalue of $a^\dagger$ gives the angle of direction of propagation for

incoming wave. Using the modes for the infinite lead defined in Eq. (5.29) as a basis and taking into account that action of $a^\dagger$ on oscillator state shifts this state (see Eq. (5.23)), we obtain another form of the operator $\hat{a}^\dagger$:

$$a^\dagger_{\Psi,in} = \begin{pmatrix} 0 & e^{2il} \\ 1 & 0 \end{pmatrix}. \tag{5.31}$$

This form of creation operator can be checked by direct action on basis states:

$$\hat{a}^\dagger \Psi_1(l) = \frac{\sqrt{N_c + 1}}{M} \sum_{N=N_c+1}^{\infty} e^{-2ilN} |2N + 1\rangle \sim \Psi_2(l),$$

$$\hat{a}^\dagger \Psi_2(l) = \frac{\sqrt{N_c + 1}}{M} \sum_{N=N_c+1}^{\infty} e^{-2ilN} |2N + 2\rangle \sim e^{2ikl} \Psi_1(l). \tag{5.32}$$

The eigenvalues and eigenvectors of $a^\dagger_\psi$ operator are given by

$$\lambda_{1,2} = \pm e^{il}, \quad \chi_1 = \frac{1}{\sqrt{2}} \begin{pmatrix} 1 \\ e^{-il} \end{pmatrix}, \quad \chi_2 = \frac{1}{\sqrt{2}} \begin{pmatrix} -e^{il} \\ 1 \end{pmatrix}. \tag{5.33}$$

Notably, for momenta l of the propagating modes close to Brillouin zone edge $l = \pm\pi/4$, we uncover the correspondence with asymptotic angles of the constant energy curves at large momenta that correspond to directions of incoming and outgoing modes in MB region. Now we have to convert the S_Ψ-matrix from the basis of the modes (5.29) to the modes with definite angle. The S-matrix itself has the form

$$S_\Psi = \begin{pmatrix} e^{i\alpha_1} & 0 \\ 0 & e^{i\alpha_2} \end{pmatrix} \tag{5.34}$$

with two phases calculated numerically by matching using Kwant code. The transformation is performed via rotation defined by eigenvectors in Eq. (5.33), while taking into account that outgoing modes have opposite momenta $-l$ and the sign of momenta changes in $a^\dagger_{\Psi,out}$. For example, $a^\dagger_{\Psi,out}(l) = a^\dagger_{\Psi,in}(-l)$ in this system because of dispersion relation (5.29). Then, the rotation to new basis of the S-matrix gives:

$$S = U_{out} S_\Psi U^\dagger_{in}, \quad U_{out} = \frac{1}{\sqrt{2}} \begin{pmatrix} 1 & -e^{-il} \\ e^{il} & 1 \end{pmatrix}, \quad U_{in} = \frac{1}{\sqrt{2}} \begin{pmatrix} 1 & -e^{il} \\ e^{-il} & 1 \end{pmatrix},$$

$$\tag{5.35}$$

which results in

$$S = \frac{1}{2} \begin{pmatrix} e^{i\alpha_1} + e^{i\alpha_2 - 2il} & e^{i(\alpha_1 + l)} - e^{-i(l - \alpha_2)} \\ e^{i(\alpha_1 + l)} - e^{-i(l - \alpha_2)} & e^{i\alpha_2} + e^{i(\alpha_1 + 2l)} \end{pmatrix}, \quad l = \frac{1}{2} \arccos \frac{E}{2t}.$$
(5.36)

This is the final form of S-matrix, which describes the magnetic breakdown near usual saddle point. By making the cut-off parameter N_c large enough, we calculate the S-matrix with arbitrary precision. The results of the calculation in comparison with exact expression as a function of energy are presented in Fig.2 of the main text. The figure demonstrates excellent agreement between exact analytic expression given by and numerical calculations with $N_c = 2000$.

5.A.3 Monkey saddle point

In this section, we extend the algorithm described above to the more complicated case of Monkey saddle point. The main complication arises due to the fact that the Hamiltonian is now third-order and we have to define 3×3 S-matrix between 3 incoming and 3 outgoing trajectories. Typically, the effective Hamiltonian in the vicinity of Monkey saddle point has the form [109, 110]:

$$H_M = \left(k_x^3 - 3k_x k_y^2 \right),$$
(5.37)

where we omit constants for simplicity. To obtain this operator in terms in ladder operators for a system under magnetic field, we perform symmetrization of the second term that makes the Hamiltonian Hermitian. The direct calculation shows that possible choices $\Pi_y \Pi_x \Pi_y$ and $\frac{1}{2} \left(\Pi_x \Pi_y^2 + \Pi_y^2 \Pi_x \right)$ give the same result. In other words, we find in terms of ladder operators that the following expressions are identical:

$$- 2\sqrt{2}\Pi_y \Pi_x \Pi_y = \left(\hat{a} - \hat{a}^\dagger \right) \left(\hat{a} + \hat{a}^\dagger \right) \left(a - a^\dagger \right)$$

$$= \hat{a}^3 - \hat{a}^2 \hat{a}^\dagger + \hat{a}\hat{a}^\dagger \hat{a} - \hat{a}\hat{a}^{\dagger,2} - \hat{a}^\dagger \hat{a}^2 + \hat{a}^\dagger \hat{a}\hat{a}^\dagger - \hat{a}^{\dagger,2}\hat{a} + \hat{a}^{\dagger,3}$$

(we use commutation relation $[\hat{a}, \hat{a}^\dagger] = 1$ and find

$$- \hat{a}^2 \hat{a}^\dagger - \hat{a}^\dagger \hat{a}^2 = -2\hat{a}\hat{a}^\dagger \hat{a}, \quad -\hat{a}^{\dagger,2}\hat{a} - \hat{a}\hat{a}^{\dagger,2} = -2\hat{a}^\dagger \hat{a}\hat{a}^\dagger)$$

$$= \hat{a}^3 - \hat{a}\hat{a}^\dagger \hat{a} - \hat{a}^\dagger \hat{a}\hat{a}^\dagger + \hat{a}^{\dagger,3},$$
(5.38)

$$- \sqrt{2} \left(\Pi_x \Pi_y^2 + \Pi_y^2 \Pi_x \right) = \hat{a}^3 - \hat{a}\hat{a}^\dagger \hat{a} - \hat{a}^\dagger \hat{a}\hat{a}^\dagger + \hat{a}^{\dagger,3}.$$
(5.39)

However, the ambiguity of choice of symmetrization should be formally resolved to apply the procedure for more complicated saddle point Hamiltonians. We do

this by starting from the tight-binding Hamiltonian, that has such saddle point, and introducing canonical momenta there. Using Eq.(18) from the main text, we find the following third-order term in expansion

$$H_{tr}(\mathbf{k}) = 2t \left(\sin \Pi_x a - \sin \frac{\Pi_x - \sqrt{3}\Pi_y}{2} a - \sin \frac{\Pi_x + \sqrt{3}\Pi_y}{2} a \right)$$

$$\sim -\frac{t}{4} \left(\Pi_x^3 - \Pi_x \Pi_y \Pi_y - \Pi_y \Pi_x \Pi_y - \Pi_y \Pi_y \Pi_x \right) a^3 + O(a^5). \quad (5.40)$$

Using above-written two relations, we simplified the symmetrized expression to Eq.(8) in the main text. However, in the general case one should keep full expression of symmetrized Hamiltonian for a particular lattice. Converting into matrix form, we find for Monkey saddle:

$$H_M = -\frac{1}{2\sqrt{2}} [\left(\hat{a} + \hat{a}^\dagger\right)^3 + 3 \left(\hat{a} - \hat{a}^\dagger\right) \left(\hat{a} + \hat{a}^\dagger\right) \left(a - a^\dagger\right)]$$

$$= \frac{1}{2\sqrt{2}} \begin{pmatrix} 0 & 0 & 0 & 4\sqrt{6} & 0 & 0 & \dots \\ 0 & 0 & 0 & 0 & 8\sqrt{6} & 0 & \dots \\ 0 & 0 & 0 & 0 & 0 & 8\sqrt{15} & \dots \\ 4\sqrt{6} & 0 & 0 & 0 & 0 & 0 & \dots \\ 0 & 8\sqrt{6} & 0 & 0 & 0 & 0 & 4\sqrt{n(n+1)(n+2)} \\ 0 & 0 & 8\sqrt{15} & 0 & 0 & 0 & \dots \\ \dots & \dots & \dots & \dots & 4\sqrt{n(n+1)(n+2)} & \dots & \dots \end{pmatrix}.$$

$$(5.41)$$

Searching the solution in the form (5.27) of decomposition of wave function in oscillator basis states, we find the following system of coupled equations:

$$2\sqrt{2}E\phi_0 - 4\sqrt{6}\phi_3 = 0,$$
$$2\sqrt{2}E\phi_1 - 8\sqrt{6}\phi_4 = 0,$$
$$2\sqrt{2}E\phi_2 - 8\sqrt{15}\phi_5 = 0,$$
$$2\sqrt{2}E\phi_3 - 4\sqrt{6}\phi_0 - 8\sqrt{30}\phi_6 = 0,$$
$$\dots$$
$$2\sqrt{2}E\phi_n - 4\sqrt{n(n-1)(n-2)}\phi_{n-3} - 4\sqrt{(n+1)(n+2)(n+3)}\phi_{n+3} = 0.$$
$$(5.42)$$

Following the procedure of mapping on 1D tight-binding model, we find that this system in turn converts into three decoupled chains with only nearest neighbor hoppings in each (see Fig. 5.5 and Fig. 2 from the main text).
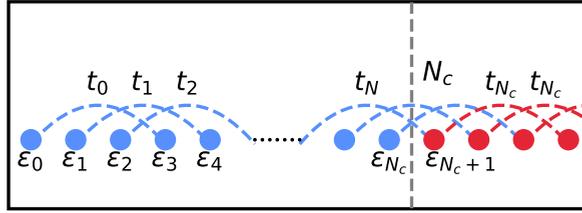
Figure 5.5. Effective 1D tight-binding model that represents the system of equations (5.42) for Monkey saddle with asymptotic truncation after Landau level index $n > N_c$.

Next steps require the introduction of the cut-off parameter N_c and classification of the modes appearing for higher indices $n > N_c$. In the case of the model with three decoupled chains the Bloch eigenstates are

$$\Psi_j(l) = \frac{1}{M} \sum_{n=N_c+1}^{\infty} e^{-3iln} |3n + i\rangle, \varepsilon_j(l) = -E + 2t_{N_c} \cos 3l, \quad j = 0, 1, 2.$$
(5.43)

In this case, the size of the unit cell is $3l$. Acting with the creation operator $\hat{a}^\dagger$, we find the following expression for the matrix in the basis of these states:

$$a^\dagger_{\Psi,in} = \begin{pmatrix} 0 & 0 & e^{3il} \\ 1 & 0 & 0 \\ 0 & 1 & 0 \end{pmatrix}.$$
(5.44)

Comparing to the matrix representation of $a^\dagger_{\Psi,in}$ for usual van Hove singularity (5.31), we see that it has similar structure with shift of nodes by one index in the unit cell until the period reached. The eigenvalues and eigenvectors of this matrix are

$$\lambda_{1,2,3} = e^{il}, \ e^{il \pm 2\pi i/3}, \quad \chi_1 = \frac{1}{\sqrt{3}} \begin{pmatrix} 1 \\ e^{-il} \\ e^{-2il} \end{pmatrix},$$

$$\chi_2 = \frac{1}{\sqrt{3}} \begin{pmatrix} e^{il+2\pi i/3} \\ 1 \\ e^{-il-2\pi i/3} \end{pmatrix} \chi_3 = \frac{1}{\sqrt{3}} \begin{pmatrix} e^{2il+2\pi i/3} \\ e^{il-2\pi i/3)} \\ 1 \end{pmatrix}$$
(5.45)

In the limit of $E \ll 2t_{N_c}$, we find that momenta of the modes are approximately
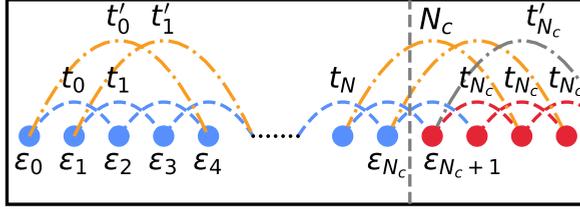
Figure 5.6. Effective 1D tight-binding model that represents the system of equations (5.51) for A_3 saddle with asymptotic truncation after Landau level index $n > N_c$. Note that now next nearest neighbor hoppings are added in each chain.

at the effective Brillouin zone edge,

$$l = \frac{1}{3} \arccos \frac{E}{2t_{N_c}} \approx \frac{\pi}{6}, \tag{5.46}$$

and the phases of eigenvalues $\lambda_{1,2,3}$ correspond to the angles at which scattering states come from the quasiclassical regions for a Monkey saddle (see Fig. 2(a) in the main text).

The eigenvectors in Eq. (5.45) define the rotation to the basis with definite angles. Combining these eigenvectors into unitary transformation matrix, we then apply the basis transformation to the diagonal scattering matrix obtained from the numerical calculation,

$$S_\Psi = \mathrm{diag}(e^{i\alpha_1}, e^{i\alpha_2}, e^{i\alpha_3}). \tag{5.47}$$

The diagonal structure of this matrix is a result of chain decoupling in the effective tight-binding model. We present the result of numerical calculation in Fig. 2 of the main text.

5.A.4   High-order saddle points with different powers in effective dispersion: A_3 saddle point and regularization

Finally, we discuss the case of A_3 saddle point, which has two trajectories coming close in the magnetic breakdown region, but the effective Hamiltonian has different powers in leading order for k_x and k_y. The analysis of this point requires several additional steps, that can be used together with algorithm from previous section to analyze every other saddle point. There are two complications that

appear for such system comparing to usual saddle point discussed in Sec. 5.A.2. The effective Hamiltonian of the model is given by

$$H_{A_3} = \alpha k_x^2 a^2 - k_y^4 a^4. \tag{5.48}$$

As we see, larger the deviation of momenta is from the center of saddle point, $k_x = k_y = 0$, the closer trajectory angles are to zero. In other words, the constant energy curve solution $k_y(k_x, E)$ behaves asymptotically as $\sqrt{k_x}$ and never reaches the k_x-independent derivative. This introduces a problem of classification of modes by angle of incoming quasiclassical particle, the central ingredient used in previous cases. In fact, such problem may lead to unexpected numerical artifacts appearing in the final scattering matrix. We resolve this problem by introducing sub-leading terms into the Hamiltonian to make the highest polynomial powers for k_x and k_y identical. In our case this would lead to the following modification of original Hamiltonian:

$$\tilde{H}_{A_3} = \alpha k_x^2 a^2 + \beta k_x^4 a^4 - k_y^4 a^4, \quad \beta > 0. \tag{5.49}$$

Here, the condition $\beta > 0$ enforces the trajectories to have different asymptotic angles, that are found from the equation $\tan^4 \phi_k = \beta$, and are equal to $\pm \arctan \beta^{1/4}$, $\pi \pm \arctan \beta^{1/4}$. The ladder operator version of this Hamiltonian is

$$\tilde{H}_{A_3} = \alpha \left(\hat{a} + \hat{a}^\dagger \right)^2 + \beta \left(\hat{a} + \hat{a}^\dagger \right)^4 - \left(\hat{a} - \hat{a}^\dagger \right)^4. \tag{5.50}$$

The main difference comparing to the previously discussed cases is that this Hamiltonian contains both second and fourth order terms, which implies the existence of two kinds of hopping terms. The system of recursive equations in this case is

$$E\phi_0 - (\phi_0(\alpha + 3\beta - 3) + \sqrt{2}\phi_2(\alpha + 6\beta + 6) + 2\sqrt{6}(\beta - 1)\phi_4) = 0,$$

$$E\phi_1 - (3\phi_1(\alpha + 5\beta - 5) + \sqrt{6}\phi_3(\alpha + 10\beta + 10) + 2\sqrt{30}(\beta - 1)\phi_5) = 0,$$

$$\dots$$

$$E\phi_n - \Big(\sqrt{(n-1)n}\phi_{n-2}(\alpha + 2(\beta + 1)(2n - 1))$$

$$+ \phi_n(2\alpha n + \alpha + 3(\beta - 1)(2n(n + 1) + 1))$$

$$+ \sqrt{(n+1)(n+2)}\phi_{n+2}(\beta + 2(\beta + 1)(2n + 3))$$

$$+ (\beta - 1)\sqrt{\prod_{j=0}^{3}(n - j)}\phi_{n-4} + (\beta - 1)\sqrt{\prod_{j=1}^{4}(n + j)}\phi_{n+4} \Big) = 0 \tag{5.51}$$

After mapping we obtain the system with two decoupled chains, see Fig. 5.6. Now each of these chains contains both nearest neighbor t_i and next nearest neighbor t'_i hopping terms as well as index-dependent on-site terms ε_n. In the case of more general saddle points one might obtain even more far-distanced next-next-...-nearest hoppings according to polynomial powers in the Hamiltonian. The basis of plane waves in the truncated region is built in the same way as before, thus rotation to the basis with proper angles is done via the same procedure of diagonalization of ladder operator $\hat{a}^\dagger$ acting on propagating modes. However, the dispersion relation of plane wave modes is more complicated, in this particular case it has the form:

$$\varepsilon_{1,2}(l) = -E + E_{N_c} + 2t_{N_c} \cos 2l + 2t'_{N_c} \cos 4l. \tag{5.52}$$

Expressing momentum from this equation for $\varepsilon(l) = 0$ condition, we obtain proper angles of the modes from $a^\dagger_\psi$ operator given by Eq. (5.33).

As a result of the regularization procedure, we have to introduce an additional parameter β into the lowest-order effective Hamiltonian. We check this by taking this parameter small enough the convergence of results is reachable. We compare the results for absolute value of the scattering matrix elements fixing $A = 1$ and taking different $\beta \ll 1$ in Eq. (5.49) The values of scattering matrix elements are shown in Fig. 5.7. For small enough β the results converge rapidly.

5.B   Magnetic translation operators and spectral equations for coherent networks

In this section of Supplemental material, we present the main technical steps that are required to describe the problem of two-dimensional Bloch electrons in presence of magnetic field applied perpendicularly to the system at energies in the vicinity of van Hove singularity, when a coherent orbit network is formed. We demonstrate our approach in cases of square and triangular lattices that exhibit three different types of van Hove singularities. Before proceeding to the derivation of spectral equations for particular systems, we briefly recall the translation symmetry group in the presence of magnetic field.

5.B.1   Magnetic translation group

The general aspects of the translation symmetry group theory in the presence of magnetic field were discussed in Ref. [118]. Here, we recall the key definitions and properties of Bloch electrons in the presence of magnetic field.
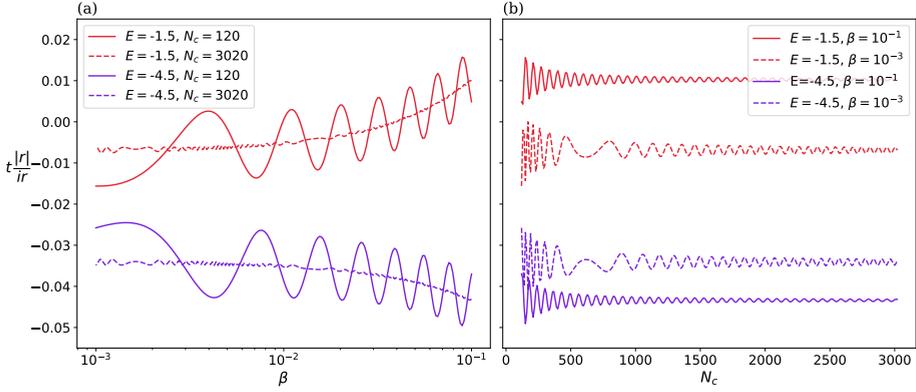
Figure 5.7. Convergence of absolute values of S-matrix elements (t-transmission, r-reflection) for A_3 saddle point with different values of regularization parameter β in Eq. (5.49). The coefficients $a = 1$ and $\alpha = 1$ are taken for simplicity. Two panels demonstrate convergence with different (a) N_c cutoff parameters as function of β, (b) β regularizing coefficients as function of N_c.

The key operator that commutes with a Hamiltonian and therefore identifies the eigenstates and corresponding eigenvalues is the magnetic translation operator

$$\hat{T}_{\boldsymbol{R}}^M = \exp\{\frac{i}{\hbar} \left(\boldsymbol{p} + \frac{e}{c}\overline{\boldsymbol{A}}(\boldsymbol{R}) \right) \boldsymbol{R}\}, \quad \overline{\boldsymbol{A}}(\boldsymbol{R}) = \boldsymbol{A}(\boldsymbol{R}) + \boldsymbol{R} \times \boldsymbol{B}, \qquad (5.53)$$

with $\boldsymbol{p}$ being a momenta operator. To find an analytical solution of the problem, commensurability between lattice and magnetic translation periods is required. This condition, expressed in terms of the magnetic translation operators, reads $\hat{T}_{N\boldsymbol{R}}^M \Psi = \Psi$, where N is large integer and $\boldsymbol{R}$ an arbitrary lattice vector. The periodic condition implies $[\hat{T}_{N\boldsymbol{R}}^M, \hat{T}_{\boldsymbol{R}'}^M] = 0$ and can be equally written as a rationality condition on magnetic field flux through the elementary unit cell

$$\Phi = B|\boldsymbol{R}_1 \times \boldsymbol{R}_2| = B\frac{(2\pi)^2}{|\boldsymbol{b}_1 \times \boldsymbol{b}_2|} = \frac{q}{p}\frac{2\pi\hbar c}{e} = \frac{q}{p}\Phi_0, \qquad (5.54)$$

where numbers q, p are co-prime integers, p is divisor of N, and $\Phi_0 = \frac{2\pi e}{c}$ is a flux quantum. Later on we shall concentrate on the case of $q = 1$ for which magnetic field values form a dense set for large p and small magnetic fields. Other values of q can be analyzed in a similar manner.

For the set of magnetic translation operator to form a group, we need to adjust

its definition by adding a phase factor [118]

$$\hat{T}_{m,\boldsymbol{R}}^{M} = e^{i\pi(2m-jk)/p}\hat{T}_{\boldsymbol{R}}^{M}; \quad \boldsymbol{R} = j\boldsymbol{R}_1 + k\boldsymbol{R}_2, \tag{5.55}$$

where R_1, R_2 are elementary unit vectors. This group has N^2 p-dimensional irreducible representations, classified by quasimomenta eigenvalues $\boldsymbol{q} = \frac{1}{N}(n_1\boldsymbol{b}_1 + n_2\boldsymbol{b}_2), n_1, n_2 = 0, ..., \frac{N}{p} - 1$ and corresponding eigenstates $\Psi_{\alpha qs}$ as follows [118]

$$H\Psi_{\alpha qs} = \mathcal{E}_\alpha(\boldsymbol{q})\Psi_{\alpha qs}; \quad \hat{T}_{m,\boldsymbol{R}}^{M}\Psi_{\alpha qs} = e^{i(\boldsymbol{q}+\frac{s}{p}\boldsymbol{b}_1)\boldsymbol{R}}\Psi_{\alpha qs}; \quad s = 0, ..., p - 1 \tag{5.56}$$

This relation defines the translational symmetry of the problem and may be considered as an analogy of Bloch's theorem.

5.B.2   The wave function dependence on eigenvalues of the magnetic translation operator

As described in the main text a general structure of the wave function expressed in the gauge invariant space reads [139, 118, 127]

$$\Psi(k_x) = \sum_{l,k,j}^{\infty} \alpha_j e^{i(p_l l + p_k k)} e^{il_B^2[k_x l b_{2,y} - \frac{l^2}{2}b_{2,x}b_{2,y}]}\Psi_{ZF}^j(k_x - kb_{1,x} - lb_{2,x}), \tag{5.57}$$

where indices (l, k) enumerate cells in the extended Brillouin zone scheme, j identifies different branches of the wave function in the single cell, and $\Psi_{ZF}^{E,j}(k_x)$ stands for ZF function, defined in the $(0, 0)$-cell.

Phase factor $e^{i(p_l l + p_k k)}$ defines the translational symmetry of the system and therefore must be expressed in terms of quasimomenta eigenvalues of magnetic translational operator $\boldsymbol{q}$. To find the connection between p_l, p_k and $\boldsymbol{q}$ we project the solution on the representation space of magnetic translation group using a projection operator $P^{\boldsymbol{q}}$ [118]:

$$\Psi_{\mathbf{q}}(k_x) = P^{\mathbf{q}}\Psi(k_x), \ P^{\mathbf{q}} = C_{\boldsymbol{q}} \sum_{k',l'=-\infty}^{\infty} e^{-i\boldsymbol{q}\cdot(\boldsymbol{b}\times\boldsymbol{\lambda})} e^{i\pi pk'l' + i(\boldsymbol{k}-\frac{e}{c}\boldsymbol{A})\cdot(\boldsymbol{b}\times\boldsymbol{\lambda})},$$

$$\boldsymbol{b} = k'\boldsymbol{b}_1 + l'\boldsymbol{b}_2 \tag{5.58}$$

where $C_{\boldsymbol{q}}$ is a normalization constant and $\boldsymbol{\lambda} = (0, 0, l_B^2)$ is a vector oriented along magnetic field . It is convenient to choose a system of coordinates where

$\boldsymbol{b}_1 = (b_{1,x}, 0, 0)$ and $\boldsymbol{b}_2 = (b_{2,x}, b_{2,y}, 0)$ where the projection operator expressed in the gauge invariant space $k_x = (\boldsymbol{p} + \frac{e}{c}\boldsymbol{A})_x, -\frac{i}{l_B^2}\partial_{k_x} = (\boldsymbol{p} + \frac{e}{c}\boldsymbol{A})_y$ reads

$$P^{\boldsymbol{q}} = C_{\boldsymbol{q}} \sum_{k',l'} e^{-il_B^2 l'(q_1 b_{2,y} - q_2 b_{2,x})} e^{il_B^2 l'(b_{2,y}k_x + i\frac{b_{2,x}}{l_B^2}\partial_{k_x})} e^{il_B^2 k' q_2 b_{1,x}} e^{-k' b_{1,x}\partial_{k_x}}$$

$$(5.59)$$

First, we calculate the projection part depending on k'

$$e^{il_B^2 k' q_2 b_{1,x}} e^{-k' b_{1,x}\partial_{k_x}} \sum_{l,k,j}^{\infty} \alpha_j e^{i(p_l l + p_k k)} e^{il_B^2 [k_x l b_{2,y} - \frac{l^2}{2}b_{2,x}b_{2,y}]}$$

$$\times \Psi_{ZF}^j(k_x - k b_{1,x} - l b_{2,x})$$

$$= e^{il_B^2 k' q_2 b_{1,x}} \sum_{l,k,j}^{\infty} \alpha_j e^{i(p_l l + p_k k)} e^{il_B^2 [(k_x - k' b_{1,x})l b_{2,y} - \frac{l^2}{2}b_{2,x}b_{2,y}]}$$

$$\times \Psi_{ZF}^j(k_x - (k + k')b_{1,x} - l b_{2,x})$$

$$= e^{ik'[l_B^2 q_2 b_{1,x} - p_k]} \sum_{l,k,j}^{\infty} \alpha_j e^{i(p_l l + p_k k)} e^{il_B^2 [k_x l b_{2,y} - \frac{l^2}{2}b_{2,x}b_{2,y}]}$$

$$\times \Psi_{ZF}^j(k_x - k b_{1,x} - l b_{2,x}), \qquad (5.60)$$

where in the second line we used $e^{a\partial_{k_x}} f(k_x) = f(k_x + a)$ and in the last line we renamed $k \to k + k'$ and used $e^{il_B^2 b_{1,x}b_{2,y}} = e^{il_B^2 |\boldsymbol{b}_1 \times \boldsymbol{b}_2|} = e^{i2\pi p} = 1$. Now, we

calculate the second part of projection depending on l'

$$e^{-il_B^2 l'(q_1 b_{2,y} - q_2 b_{2,x})} e^{il_B^2 l'(b_{2,y} k_x + i\frac{b_{2,x}}{l_B^2}\partial_{k_x})}$$

$$\times \sum_{l,k,j}^{\infty} \alpha_j e^{i(p_l l + p_k k)} e^{il_B^2[k_x l b_{2,y} - \frac{l^2}{2}b_{2,x}b_{2,y}]} \Psi_{ZF}^j(k_x - kb_{1,x} - lb_{2,x})$$

$$= e^{-il_B^2(l'(q_1 b_{2,y} - q_2 b_{2,x}) + \frac{l'^2}{2}b_{2,x}b_{2,y} - l'b_{2,y}k_x)} e^{-l'b_{2,x}\partial_{k_x}}$$

$$\times \sum_{l,k,j}^{\infty} \alpha_j e^{i(p_l l + p_k k)} e^{il_B^2[k_x l b_{2,y} - \frac{l^2}{2}b_{2,x}b_{2,y}]} \Psi_{ZF}^j(k_x - kb_{1,x} - lb_{2,x})$$

$$= e^{il_B^2(l'b_{2,y}k_x - l'(q_1 b_{2,y} - q_2 b_{2,x}) - \frac{l'^2}{2}b_{2,x}b_{2,y})}$$

$$\times \sum_{l,k,j}^{\infty} \alpha_j e^{i(p_l l + p_k k)} e^{il_B^2[(k_x - l'b_{2,x})lb_{2,y} - \frac{l^2}{2}b_{2,x}b_{2,y}]} \Psi_{ZF}^j(k_x - kb_{1,x} - (l + l')b_{2,x})$$

$$= e^{-il'[l_B^2(q_1 b_{2,y} - q_2 b_{2,x}) - p_l]}$$

$$\times \sum_{l,k,j}^{\infty} \alpha_j e^{i(p_l l + p_k k)} e^{il_B^2[k_x l b_{2,y} - \frac{l^2}{2}b_{2,x}b_{2,y}]} \Psi_{ZF}^j(k_x - kb_{1,x} - lb_{2,x})$$

$$\tag{5.61}$$

Finally we see that the projecting results in

$$\Psi_{\mathbf{q}}(k_x) = C_{\mathbf{q}} \sum_{k',l'=-\infty}^{\infty} e^{-il'[l_B^2(q_1 b_{2,y} - q_2 b_{2,x}) + p_l]} e^{ik'[l_B^2 q_2 b_{1,x} - p_k]} \Psi(k_x). \tag{5.62}$$

The summation over k', l' establishes the connection between p_k, p_l and $\mathbf{q}$ as $p_k = l_B^2 q_2 b_{1,x}$ and $p_l = l_B^2 (q_2 b_{2,x} - q_1 b_{2,y})$. Utilizing this relation, we find a general form of the wave function as a eigenfunction of the magnetic translation operator

$$\Psi_{\mathbf{q}}(k_x) = \sum_{l,k,j}^{\infty} \alpha_j e^{il_B^2([q_2 b_{2,x} - q_1 b_{2,y}]l + q_2 b_{1,x}k)} e^{il_B^2[k_x l b_{2,y} - \frac{l^2}{2}b_{2,x}b_{2,y}]}$$

$$\times \Psi_{ZF}^j(k_x - kb_{1,x} - lb_{2,x}) \tag{5.63}$$

To define α_i coefficients and allowed energy values, we need to connect pieces of the wave function in neighbouring cells of the Brillouin zone as well as pieces corresponding to the different parts of the orbit in the single cell. In the following sections, we perform this for the cases of square and triangular lattices by solving a scattering problem near the van Hove singularities.
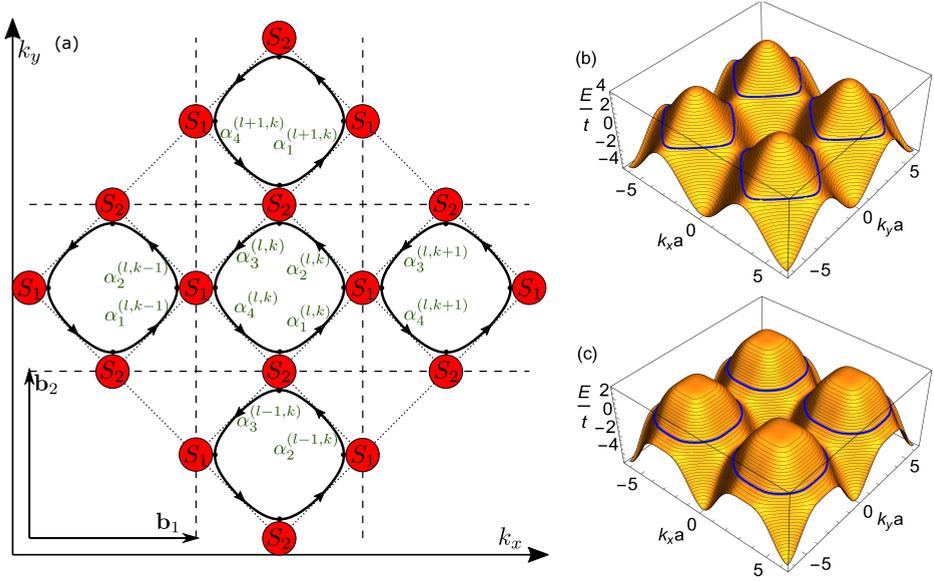
Figure 5.8. Panel (a): schematic geometry of the orbit network from Eq.5.68 in the square lattice. Panel (b): tight binding energy dispersion of the square lattice with only nearest neighbor hoppings t involved; constant energy contours and schematicly represented orbits at a particular fixed energy (blue lines) are highlighted. Panel (c): spectrum of the same square lattice as in (b) but with third nearest neighbor hoppings $t_3 = 1/4t$ taken into account.

5.B.3 Square lattice: derivation of spectral equation for orbit network

In this section, we present the technical details of derivation of the orbit network spectral equation for the simplest case of square lattice. The Brillouin zone of the square lattice contains saddle points at the X-points. The tight-binding Hamiltonian in the case where only nearest neighbor hopping is taken into account reads

$$H_{sq} = -2t(\cos(k_x a) + \cos(k_y a)), \tag{5.64}$$

with a being a lattice constant and t is hopping parameter. This Hamiltonian exhibits the saddle points at X-points in Brillouin zone

$$E_{\pi/a,0}(\boldsymbol{k}) \approx -a^2 t[(k_x - \pi/a)^2 - k_y^2], \quad E_{0,\pi/a}(\boldsymbol{k}) \approx a^2 t[k_x^2 - (k_y - \pi/a)^2]. \tag{5.65}$$

They result in usual logarithmic van Hove singularities in the density of states. One can modify Eq. (5.64) by taking hopping t_3 to the third nearest neighbor into account

$$H_{sq,2} = -2t \left(\cos k_x a + \cos k_y a \right) - 2t_3 \left(\cos 2k_x a + \cos 2k_y a \right), \qquad (5.66)$$

and obtain high-order saddle points of cusp type A_3 [109] at each X-point for $t_3 = 1/4t$:

$$E_{\pi/a,0} \approx -\frac{1}{4}a^4 t q_x^4 - \frac{5}{12}a^4 t q_y^4 + 2a^2 t q_y^2 - t,$$

$$E_{0,\pi/a} \approx -\frac{5}{12}a^4 t q_x^4 + 2a^2 t q_x^2 - \frac{1}{4}a^4 t q_y^4 - t. \qquad (5.67)$$

Such saddle points result in high-order van Hove singularities with divergence exponent 1/4. Recently, a slightly different version of this model with nearest-neighbor (NN), next NN and third NN hoppings was analyzed in Ref. [155] with relation to enhanced nematicity effects.

While we keep the hopping parameters isotropic (equal along x- and y-directions), the qualitative geometry of the coherent orbit network does not change due to saddle point type. It is schematically shown in Fig. 5.8 together with tight-binding dispersion plots with highlighted equi-energy contours.

To derive a solution for the orbit network, we note that each unit cell of the network in Fig. 5.8 can be separated into four quasiclassical regions which can be described by WKB-type Zilberman-Fischbeck (ZF) wave functions, and four scattering regions of magnetic breakdown with corresponding scattering matrices $S_{1,2}$.

$$\Psi_{\boldsymbol{q}}(k_x) = \sum_{l,k=-\infty}^{\infty} e^{i(p_k k + p_l l)} e^{i l_B^2 l b_{2,y} k_x}$$

$$\times \begin{cases} \alpha_1 h_1(k_x) e^{i l_B^2 \int_{kb_{1,x}}^{k_x} dk_x k_y^{E,b}(k_x)} + \alpha_2 h_2(k_x) e^{i l_B^2 \int_{kb_{1,x}}^{k_x} dk_x k_y^{E,t}(k_x)}, \\ \qquad\qquad \text{when } kb_{1,x} < k_x < (k + \frac{1}{2})b_{1,x}, \\ \alpha_3 h_3(k_x) e^{i l_B^2 \int_{kb_{1,x}}^{k_y} dk_x k_y^{E,t}(k_x)} + \alpha_4 h_4(k_x) e^{i l_B^2 \int_{kb_{1,x}}^{k_x} dk_x k_y^{E,b}(k_x)}, \\ \qquad\qquad \text{when } (k - \frac{1}{2})b_{1,x} < k_x < kb_{1,x}, \end{cases} \qquad (5.68)$$

where $h_i(k_x) = \left(\left| \frac{\partial E(\boldsymbol{k})}{\partial k_y} \right| \right)^{-\frac{1}{2}}$. We choose zero of k_x as point in the middle of single Brillouin zone. In each cell of reciprocal lattice, we have two solutions for

$k_y^E(k_x)$ at constant energy which we call "top" $k_y^{E,t}(k_x)$ and "bottom" $k_y^{E,b}(k_x)$.
The functional dependence $k_y^{E,t(b)}(k_x)$ is found directly from exact dispersion
relation at a given energy. For example, in the case of Eq. (5.64), we find

$$k_y^{E,t(b)}(k_x, E) = \pm \frac{1}{a} \arccos \left[-\frac{E + 2t \cos(k_y a)}{2t} \right], \qquad (5.69)$$

while in most other cases the numerical evaluation has to be used.

To build the closed system of equations for coefficients α_j, we use the mag-
netic breakdown S-matrix that couples two neighboring cells of the network.
For the case of isotropic square lattice all S-matrices are identical, so the only
difference comes from the geometric arrangement of cyclotron orbits coming to
each magnetic breakdown region. We thus write the corresponding equations as
'horizontal' scattering with S_1 matrix and 'vertical' scattering with S_2 referring
to the notation from Fig. 5.8(a). For the 'horizontal' MB region we obtain:

$$\begin{pmatrix} \alpha_2 e^{i \int_{kb_{1,x}}^{(k+\frac{1}{2})b_{1,x}} dk_x k_y^{E,t}(k_x)} \\ \alpha_4 e^{ip_k - i \int_{kb_{1,x}}^{(k+\frac{1}{2})b_{1,x}} dk_x k_y^{E,b}(k_x)} \end{pmatrix} = S_1 \begin{pmatrix} \alpha_1 e^{i \int_{kb_{1,x}}^{(k+\frac{1}{2})b_{1,x}} dk_x k_y^{E,b}(k_x)} \\ \alpha_3 e^{ip_k - i \int_{kb_{1,x}}^{(k+\frac{1}{2})b_{1,x}} dk_x k_y^{E,t}(k_x)} \end{pmatrix}, \qquad (5.70)$$

where we used that $h_i(k_x)$ are equal for all i at scattering points. Similarly for
the 'vertical' MB region we write:

$$\begin{pmatrix} \alpha_1 e^{ip_l} \\ \alpha_3 \end{pmatrix} = S_2 \begin{pmatrix} \alpha_2 \\ \alpha_4 e^{ip_l} \end{pmatrix}. \qquad (5.71)$$

Note that here, we used the relation $l_B^2 b_{1,x} b_{2,y} = 2\pi p$.

Now, taking into account the series decomposition of dispersion around
saddle point in the case of isotropic square lattice (e.g. Eq. (5.65) or Eq. (5.67))
and the geometry of the orbits in Fig. 5.8, we obtain the rotation rules for the
S-matrix ($\mathcal{R}$ and $\mathcal{T}$ are absolute values of reflection and transmission coefficients
along the k_x direction for S_1):

$$S_1 = \begin{pmatrix} -i\mathcal{R}e^{i\varphi_r} & \mathcal{T}e^{i\varphi_t} \\ \mathcal{T}e^{i\varphi_t} & -i\mathcal{R}e^{i\varphi_r} \end{pmatrix}, \quad S_2 = \begin{pmatrix} i\mathcal{T}e^{i\varphi_t} & \mathcal{R}e^{i\varphi_r} \\ \mathcal{R}e^{i\varphi_r} & i\mathcal{T}e^{i\varphi_t} \end{pmatrix}. \qquad (5.72)$$

These relations are obtained by noting that absolute values of transitions between
part of trajectories $1 \rightarrow 2$ and $3 \rightarrow 4$ at point S_1 should be equal to $2 \rightarrow 3$ and

$4 \rightarrow 1$ at point S_2. The unitarity of S-matrix implies the following restrictions on S-matrix:

$$\mathcal{R}^2 + \mathcal{T}^2 = 1, \quad i\mathcal{R}\mathcal{T}e^{-i(\varphi_r - \varphi_t)} - i\mathcal{R}\mathcal{T}e^{-i(\varphi_t - \varphi_r)} = 2\mathcal{R}\mathcal{T}\sin(\varphi_r - \varphi_t) = 0. \quad (5.73)$$

The second relation implies that either $\varphi_r = \varphi_t + 0$, π, ... or one of r or t is equal to zero. Indeed, we find that both cases are realized for the A_3 saddle point, which is an example of perfect transmission along the semiclassical orbit. We note that the relation $\det(S) = e^{i\varphi_{sc}} = e^{2i\varphi_r} = e^{2i\varphi_r}$ also follows from the unitarity.

Combining (5.70) and (5.71) into system of equations for $\alpha_{1,...4}^{l,k}$ parameters, we find

$$\begin{pmatrix} -i\mathcal{R}e^{i\varphi_r}e^{i\Phi_b} & -e^{i\Phi_t} & \mathcal{T}e^{i\varphi_t}e^{i(p_k-\Phi_t)} & 0 \\ \mathcal{T}e^{i\varphi_t}e^{i\Phi_b} & 0 & -i\mathcal{R}e^{i\varphi_r}e^{i(p_k-\Phi_t)} & -e^{i(p_k-\Phi_b)} \\ -e^{ip_l} & i\mathcal{T}e^{i\varphi_t} & 0 & \mathcal{R}e^{i\varphi_r}e^{ip_l} \\ 0 & \mathcal{R}e^{i\varphi_r} & -1 & i\mathcal{T}e^{i\varphi_t}e^{ip_l} \end{pmatrix} \alpha = 0, \quad (5.74)$$

where we used the short-hand notation

$$\Phi_{b(t)} = l_B^2 \int_{kb_{1,x}}^{(k+\frac{1}{2})b_{1,x}} dk_x k_y^{E,b(t)}(k_x). \quad (5.75)$$

The condition of existence of nontrivial solution gives the spectral equation:

$$([\mathcal{R}e^{i\varphi_r}]^2 + [\mathcal{T}e^{i\varphi_t}]^2)^2 e^{i(\Phi_b - \Phi_t)} + e^{-i(\Phi_b - \Phi_t)}$$

$$-\mathcal{R}e^{i\varphi_r}\mathcal{T}e^{i\varphi_t}\left(e^{ip_l} + e^{-ip_l} + e^{i(p_k-\Phi_b-\Phi_t)}e^{-ip_l} + e^{-i(p_k-\Phi_b-\Phi_t)}\right) = 0 \quad (5.76)$$

Using that $([\mathcal{R}e^{i\varphi_r}]^2 + [\mathcal{T}e^{i\varphi_t}]^2)^2 = \det S_1^2 = e^{2i\varphi_{sc}}$, $\Phi_b = l_B^2 b_{1,x}b_{2,y} - \Phi_t = 2p\pi - \Phi_e$ (see Fig. 5.8) and the area inside the orbit is $l_B^2 \mathcal{A}(E) = 2(\Phi_t - \Phi_b)$, and obtain:

$$\cos\left(\frac{l_B^2 \mathcal{A}(E)}{2} - \varphi_{sc}\right) = e^{i(\varphi_r - \varphi_t)}\mathcal{R}\mathcal{T}(\cos(p_k) + \cos(p_l))$$

$$= \pm\mathcal{R}\mathcal{T}(\cos(p_k) + \cos(p_l)), \quad (5.77)$$

where the sign depends on whether $\varphi_r = \varphi_t$ or $\varphi_r = \varphi_t + \pi$. Rewriting this equation in terms of magnetic translation operators eigenvalues, we find:

$$\cos\left(\frac{l_B^2 \mathcal{A}(E)}{2} - \varphi_{sc}\right) = \pm\mathcal{R}\mathcal{T}\left(\cos\left(l_B^2 q_1 b_{2,y}\right) + \cos\left(l_B^2 q_2 b_{1,x}\right)\right). \quad (5.78)$$

The cosine on the left defines the standard Lifshitz-Onsager quantization rule with slightly shifted Landau levels in the vicinity of the energy of van Hove singularity due to nonzero scattering phase. The right-hand side defines mini-band broadening and leads to oscillatory behavior.

5.B.4 Triangular lattice with imaginary hoppings: orbit network connected via Monkey saddle points

In this section, we analyze a case with a more complicated geometry of a triangular lattice with imaginary hopping parameters. The tight-binding Hamiltonian in the nearest neighbor approximation is given by Eq. (18) in the main text. Similar structure of dispersion with Monkey saddle might effectively appear in Moiré materials [152]. We apply a $\pi/2$ clockwise rotation of coordinates $k_y \to k_x, k_x \to -k_y$ to the system in order to have $\boldsymbol{b}_1 = (b_{1,x}, 0, 0)$ as described in the previous sections. A schematic picture of the orbits that constitute a network is shown in Fig. 5.9. The general structure of a solution is described in the main text, in the particular case of triangular lattice the wave function has three different ZF-type terms in each unit cell and for $E > 0$ reads:

$$\Psi_{\boldsymbol{q}}(k_x) = \sum_{l,k} e^{i(p_k k + p_l l)} e^{il_B^2 [k_x l b_{2,y} - \frac{l^2}{2} b_{2,x} b_{2,y}]}$$

$$\times \left[\alpha_3 h_3(k_x) e^{il_B^2 \int\limits_{kb_{1,x}+lb_{2,x}}^{k_x} dk_x k_y^{E,3}(k_x)} \quad , \text{when } kb_{1,x} + lb_{2,x} < k_x < (k+1)b_{1,x} + lb_{2,x} \right.$$

$$+ \left\{ \begin{array}{l} \alpha_2 h_2(k_x) \quad e^{il_B^2 \int\limits_{kb_{1,x}+(l+1)b_{2,x}}^{k_x} dk_x k_y^{E,2}(k_x)} \quad , \\ \qquad \text{when } kb_{1,x} + lb_{2,x} < k_x < kb_{1,x} + (l+1)b_{2,x} \\ \alpha_1 h_1(k_x) \quad e^{il_B^2 \int\limits_{kb_{1,x}+(l+1)b_{2,x}}^{k_x} dk_x k_y^{E,1}(k_x)} \quad , \\ \qquad \text{when } kb_{1,x} + (l+1)b_{2,x} < k_x < (k+1)b_{1,x} + lb_{2,x} \end{array} \right. \left. \vphantom{\begin{array}{l} a \\ b \\ c \\ d \end{array}} \right].$$

$$(5.79)$$

The positions of scattering point are $k_{x,scatt}^{(l,k)} = kb_{1,x} + lb_{2,x}$. The case of $E < 0$ can be analyzed in the same way as $E > 0$ by making use of a symmetry property of the dispersion (3) that stays the same for $E \to -E$ and $\boldsymbol{k} \to -\boldsymbol{k}$ replacement. Therefore, later on we concentrate on the case of $E > 0$.

Now, we perform a derivation of spectral equation from the scattering equations that couple neighboring cells. The scattering equation at point $k_{x,scatt}^{(l,k)}$ has
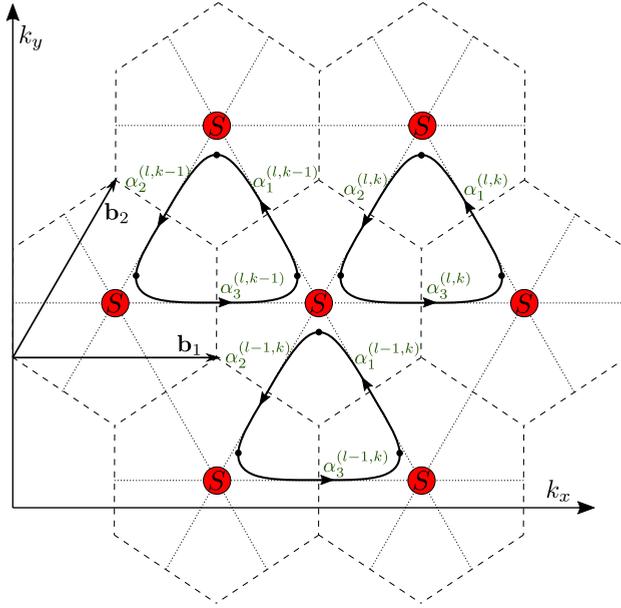
Figure 5.9. Schematic structure of the orbit network for triangular lattice with imaginary hoppings. The $\boldsymbol{b}_i$ vectors denote the basis in reciprocal space, red S circles label the positions of scattering regions with Monkey saddle. The black lines with arrows show example orbits with coefficients $\alpha_i^{l,k}$ that appear in decomposition of the wave function into Zilberman-Fischbeck wave functions between scattering regions. Indices l and k label the elementary unit cell in k-space with its position according to $\boldsymbol{b}_1$ and $\boldsymbol{b}_2$ vectors. Only the case of positive energies is shown as the negative energies can be obtain by using the symmetry of the model $E \rightarrow -E$ with $\boldsymbol{k} \rightarrow -\boldsymbol{k}$.

the form:

$$
\begin{pmatrix} \alpha_1 e^{-ip_k} e^{i\Phi_1} \\ \alpha_2 e^{-ip_l} e^{-il_B^2 \frac{b_{2,x}b_{2,y}}{2}} \\ \alpha_3 \end{pmatrix} = S \begin{pmatrix} \alpha_1 e^{-ip_l} e^{-il_B^2 \frac{b_{2,x}b_{2,y}}{2}} \\ \alpha_2 e^{-i\Phi_2} \\ \alpha_3 e^{-ip_k} e^{i\Phi_3}, \end{pmatrix}, \tag{5.80}
$$

where we used the relation $l_B^2 b_{1,x} b_{2,y} = 2\pi p$ and equality of $h_i(k_x)$ at the scattering point as well as the short-hand notation for Φ_i introduced in the previous section.

Before we insert the numerically calculated S-matrix, there is one subtlety that should be taken into account: the scattering basis of incoming and outgoing modes in numerical approach (5.45) is different from the one used in the orbit network (5.79). The difference between two pictures arises due to the fact that the numerical approach couples the incoming and outgoing modes in quasiclassical region at infinity $|\boldsymbol{k}| \to \infty$, while in the orbital network the modes are coupled at the scattering point itself

$$
\text{Orbit network:} \begin{pmatrix} \Psi_{ZF}^{out,1}(k=0) \\ \Psi_{ZF}^{out,2}(k=0) \\ \Psi_{ZF}^{out,3}(k=0) \end{pmatrix} = S \begin{pmatrix} \Psi_{ZF}^{in,1}(k=0) \\ \Psi_{ZF}^{in,2}(k=0) \\ \Psi_{ZF}^{in,3}(k=0) \end{pmatrix},
$$

$$
\text{Numerical approach:} \begin{pmatrix} \Psi_{ZF}^{out,1}(k \to \infty) \\ \Psi_{ZF}^{out,2}(k \to \infty) \\ \Psi_{ZF}^{out,3}(k \to \infty) \end{pmatrix}' = S' \begin{pmatrix} \Psi_{ZF}^{in,1}(k \to \infty) \\ \Psi_{ZF}^{in,2}(k \to \infty) \\ \Psi_{ZF}^{in,3}(k \to \infty) \end{pmatrix}'. \tag{5.81}
$$

Here, Ψ_{ZF}^{i} and the primed $\Psi_{ZF}^{i,\prime}$ wave functions correspond to the different choices of normalization constant in the bases. Thus we continue with connecting the two types of scattering states in these problems by introducing dynamical phases as well as constant phase shifts that account for selected convention in basis definitions:

$$
\Psi_{ZF}^{in,i}(k_x) = e^{i\delta_i^{in}} \Psi_{ZF}^{\prime in,i}(k_x), \quad \Psi_{ZF}^{in,i}(k_x \to \pm\infty) = e^{i\phi_{dyn}^{in,i}} \Psi_{ZF}^{in,i}(0) \tag{5.82}
$$

$$
\Psi_{ZF}^{out,i}(k_x) = e^{i\delta_i^{out}} \Psi_{ZF}^{\prime out,i}(k_x), \quad \Psi_{ZF}^{out,i}(k_x \to \pm\infty) = e^{i\phi_{dyn}^{out,i}} \Psi_{ZF}^{in,i}(0). \tag{5.83}
$$

The phase factors $e^{i\delta_i^{in}}, e^{i\delta_i^{out}}$ do not depend on energy and represent differences of the basis definitions, while $\phi_{dyn}^{in,i}, \phi_{dyn}^{out,i}$ are dynamical phases that correspond to covered areas in momentum space of ZF wave functions ψ_i^{in} - see Fig. 5.10. There, solid lines represent the real roots of equation

$$
k_y^3 + 3k_y k_x^2 = -E, \tag{5.84}
$$

defining semiclassical trajectory $k_y^E(k_x)$, while the dashed lines correspond to real parts of the complex roots in the intervals of k_x with only one allowed semiclassical trajectory. The relation between phases and the shaded areas is the following:

$$\begin{cases} \phi_{dyn}^{in,3} = -F_1 \\ \phi_{dyn}^{in,1} = -F_3 - F_4 \\ \phi_{dyn}^{in,2} = F_1 + F_2 \end{cases}, \quad \begin{cases} \phi_{dyn}^{out,3} = F_1 \\ \phi_{dyn}^{out,1} = -F_1 - F_2 \\ \phi_{dyn}^{out,2} = F_3 + F_4 \end{cases} \tag{5.85}$$

By using the symmetry of Monkey saddle dispersion $E \to -E$ together with $\mathbf{k} \to -\mathbf{k}$, we notice that $\Psi_{ZF}^{out,i}(k_x, E) = \Psi_{ZF}^{in,i}(-k_x, -E)$ and $\Psi_{ZF}'^{out,i}(k_x, E) = \Psi_{ZF}^{in,i}(-k_x, -E)$, which gives $e^{i\delta_i^{in}} = e^{i\delta_i^{out}} = e^{i\delta_i}$. Hence,

$$S = \begin{pmatrix} e^{-i\left[\phi_{dyn,1}^{out} - \delta_1\right]} & 0 & 0 \\ 0 & e^{-i\left[\phi_{dyn,2}^{out} - \delta_2\right]} & 0 \\ 0 & 0 & e^{-i\left[\phi_{dyn,3}^{out} - \delta_3\right]} \end{pmatrix} S^{num}$$

$$\times \begin{pmatrix} e^{i\left[\phi_{dyn,1}^{in} - \delta_1\right]} & 0 & 0 \\ 0 & e^{i\left[\phi_{dyn,2}^{in} - \delta_2\right]} & 0 \\ 0 & 0 & e^{i\left[\phi_{dyn,3}^{in} - \delta_3\right]} \end{pmatrix}. \tag{5.86}$$

By calculating the areas shown in Fig. 5.10 we find the following relations:

$$F_4 = \text{const}, \quad F_3 = \frac{2}{3}F_1, \quad F_2 + 2F_3 = F_4. \tag{5.87}$$

Next, we change the notation to $\phi_0 = F_1/3$, and obtain

$$\begin{cases} \phi_{dyn,3}^{in} = -3\phi_0 \\ \phi_{dyn,1}^{in} = -F_4 - 2\phi_0 \\ \phi_{dyn,2}^{in} = F_4 - \phi_0 \end{cases}, \quad \begin{cases} \phi_{dyn,3}^{out} = 3\phi_0 \\ \phi_{dyn,1}^{out} = -F_4 + \phi_0 \\ \phi_{dyn,2}^{out} = F_4 + 2\phi_0 \end{cases}. \tag{5.88}$$

At the same time following the numerical procedure described in above section, we find S-matrix:

$$S^{num} = \begin{pmatrix} \mathcal{T}e^{i\varphi_t}e^{i6\phi_0(E)} & \mathcal{R}_2 e^{i\varphi_2}e^{-i\frac{\pi}{3}+i2\phi_0(E)} & \mathcal{R}_1 e^{i\varphi_1}e^{i\frac{\pi}{3}+i4\phi_0(E)} \\ \mathcal{R}_1 e^{i\varphi_1}e^{i\frac{\pi}{3}+i4\phi_0(E)} & \mathcal{T}e^{i\varphi_t}e^{i6\phi_0(E)} & \mathcal{R}_2 e^{i\varphi_2}e^{-i\frac{\pi}{3}+i2\phi_0(E)} \\ \mathcal{R}_2 e^{i\varphi_2}e^{-i\frac{\pi}{3}+i2\phi_0(E)} & \mathcal{R}_1 e^{i\varphi_1}e^{i\frac{\pi}{3}+i4\phi_0(E)} & \mathcal{T}e^{i\varphi_t}e^{i6\phi_0(E)} \end{pmatrix}. \tag{5.89}$$
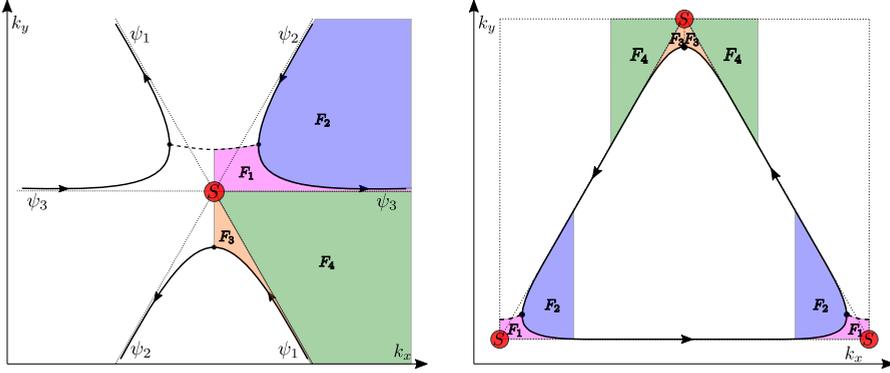
Figure 5.10. Definition of different phases according to the integration in momentum space for the scattering problem geometry around Monkey saddle point. Solid lines represent semiclassical trajectories at fixed energy near Monkey saddle, whereas dashed line depicts the real part of complex roots of Eq. (5.84) and dotted lines correspond to $E = 0$ regime. The shaded areas are related to the constant and dynamical phases according to Eq. (5.85).

Here, $\mathcal{T}, \mathcal{R}_1, \mathcal{R}_2$ are real values. The presence of $e^{i\frac{\pi}{3}}$ and e^{iF_4} phase factors is a consequence uncertainty of the dynamical phases, that are defined only up to an offset parameter. This arbitrariness is controlled by $e^{i\delta_i}$ phase factors which transform the numerical basis to the basis of the network model. Phases $e^{\varphi_t}, e^{\varphi_1}$ and e^{φ_2} are scattering phases that decay to zero with $E \rightarrow \infty$. Therefore, we have

$$
S = \begin{pmatrix}
\mathcal{T}e^{i\varphi_t}e^{i3\phi_0(E)} & \mathcal{R}_2e^{i\varphi_2}e^{i\left(\delta_1-\delta_2+2F_4-\frac{\pi}{3}\right)} & \mathcal{R}_1e^{i\varphi_1}e^{i\left(\delta_1-\delta_3+F_4+\frac{\pi}{3}\right)} \\
\mathcal{R}_1e^{i\varphi_1}e^{i\left(\delta_2-\delta_1-2F_4+\frac{\pi}{3}\right)} & \mathcal{T}e^{i\varphi_t}e^{i3\phi_0(E)} & \mathcal{R}_2e^{i\varphi_2}e^{i\left(\delta_2-\delta_3-F_4-\frac{\pi}{3}\right)-i3\phi_0(E)} \\
\mathcal{R}_2e^{i\varphi_2}e^{i\left(\delta_3-\delta_1-F_4-\frac{\pi}{3}\right)-i3\phi_0(E)} & \mathcal{R}_1e^{i\varphi_1}e^{i\left(\delta_3-\delta_2+F_4+\frac{\pi}{3}\right)} & \mathcal{T}e^{i\varphi_t}
\end{pmatrix}.
$$

$$(5.90)$$

To determine the connection between δ_i and F_4, we may use the limiting cases of big energies where the S-matrix written in the network basis must take the form of full reflection scattering matrix for each of the three trajectories with additional factor $-i$ appearing at turning point [127] (see Fig. 5.9):

$$
S(E \gg 0) = \begin{pmatrix}
0 & 0 & -i \\
1 & 0 & 0 \\
0 & -i & 0
\end{pmatrix}.
$$

$$(5.91)$$

From this condition and previously obtained expression (5.90), we find a set of

conditions, which in turn yield

$$\begin{cases} e^{i(\delta_2-\delta_1-2F_4+\pi/3)} = 1 \\ e^{i(\delta_3-\delta_2+F_4+\pi/3)} = -i \end{cases} \Rightarrow e^{i(\delta_1-\delta_3+F_4+\pi/3)}$$

$$= e^{i\pi}e^{-i(\delta_2-\delta_1-2F_4+\pi/3)}e^{-i(\delta_3-\delta_2+F_4+\pi/3)} = -i. \tag{5.92}$$

In such a way we settle all additional constants and obtained the exact form of the network model S-matrix from numerical S^{num}-matrix:

$$S = \begin{pmatrix} \mathcal{T}e^{i\varphi_t}e^{i3\phi_0(E)} & \mathcal{R}_2 e^{i\varphi_2} & -i\mathcal{R}_1 e^{i\varphi_1} \\ \mathcal{R}_1 e^{i\varphi_1} & \mathcal{T}e^{i\varphi_t}e^{i3\phi_0(E)} & i\mathcal{R}_2 e^{i\varphi_2}e^{-i3\phi_0(E)} \\ \mathcal{R}_2 e^{i\varphi_2}e^{-i3\phi_0(E)} & -i\mathcal{R}_1 e^{i\varphi_1} & \mathcal{T}e^{i\varphi_t} \end{pmatrix}. \tag{5.93}$$

Substituting it to (5.80) that couples solutions on neighboring orbits, we find:

$$\begin{pmatrix} \alpha_1 \\ \alpha_2 \\ \alpha_3 \end{pmatrix} = \begin{pmatrix} e^{i(p_k-\Phi_1)} & 0 & 0 \\ 0 & e^{i\left(p_l+l_B^2\frac{b_{2,x}b_{2,y}}{2}\right)} & 0 \\ 0 & 0 & 1 \end{pmatrix}$$

$$\times \begin{pmatrix} \mathcal{T}e^{i\varphi_t}e^{i3\phi_0(E)} & \mathcal{R}_2 e^{i\varphi_2} & -i\mathcal{R}_1 e^{i\varphi_1} \\ \mathcal{R}_1 e^{i\varphi_1} & \mathcal{T}e^{i\varphi_t}e^{i3\phi_0(E)} & i\mathcal{R}_2 e^{i\varphi_2}e^{-i3\phi_0(E)} \\ \mathcal{R}_2 e^{i\varphi_2}e^{-i3\phi_0(E)} & -i\mathcal{R}_1 e^{i\varphi_1} & \mathcal{T}e^{i\varphi_t} \end{pmatrix}$$

$$\times \begin{pmatrix} e^{-i\left(p_l+l_B^2\frac{b_{2,x}b_{2,y}}{2}\right)} & 0 & 0 \\ 0 & e^{-i\Phi_2} & 0 \\ 0 & 0 & e^{i(\Phi_3-p_k)} \end{pmatrix} \begin{pmatrix} \alpha_1 \\ \alpha_2 \\ \alpha_3 \end{pmatrix}. \tag{5.94}$$

The condition for the existence of nontrivial solution, also known as non-linear eigenvalue problem of the Ho-Chalker operator [140], gives the spectral equation

$$\det S e^{-i(\Phi_1+\Phi_2-\Phi_3)/2} + e^{i(\Phi_1+\Phi_2-\Phi_3)/2} - \left((\mathcal{T}e^{i\varphi_t})^2 e^{i6\phi_0} - \mathcal{R}_1 e^{i\varphi_1}\mathcal{R}_2 e^{i\varphi_2}\right)$$

$$\times \left[e^{-ip_l-i3\phi_0-i(\Phi_1-\Phi_2-\Phi_3+l_B^2 b_{2,x}b_{2,y})/2} + e^{-i(p_k-p_l)-i3\phi_0-i(\Phi_2-\Phi_1-\Phi_3-l_B^2 b_{2,x}b_{2,y})/2} \right.$$

$$\left. + e^{ip_k-i(\Phi_2+\Phi_1+\Phi_3)/2} \right]$$

$$-\mathcal{T}e^{i\varphi_t}\left[e^{ip_l+i3\phi_0+i(\Phi_1-\Phi_2-\Phi_3+l_B^2 b_{2,x}b_{2,y})/2} + e^{i(p_k-p_l)+i3\phi_0+i(\Phi_2-\Phi_1-\Phi_3-l_B^2 b_{2,x}b_{2,y})/2} \right.$$

$$\left. + e^{-ip_k+i(\Phi_2+\Phi_1+\Phi_3)/2} \right] = 0. \tag{5.95}$$

Note that for this kind of problems the spectral equations are a convenient tool to solve eigenvalue problem of Ho-Chalker operator as it reduces to the well-known Lifshitz-Onsager quantization condition in crystals with small corrections coming from nonzero tunneling probabilities.

We note that from unitarity of S-matrix,

$$\mathcal{T} = |(\mathcal{T}e^{i\varphi_t})^2 e^{i6\phi_0} - \mathcal{R}_1 e^{i\varphi_1}\mathcal{R}_2 e^{i\varphi_2}|,$$
$$\arg((\mathcal{T}e^{i\varphi_t})^2 e^{i6\phi_0} - \mathcal{R}_1 e^{i\varphi_1}\mathcal{R}_2 e^{i\varphi_2}) = \varphi_{sc} - \varphi_t, \qquad (5.96)$$

where $\det S = e^{i\varphi_{sc}}$. Therefore, we have

$$e^{i\varphi_{sc}/2 - i(\Phi_1+\Phi_2-\Phi_3)/2} + e^{i(\Phi_1+\Phi_2-\Phi_3)/2 - i\varphi_{sc}/2}$$

$$+\mathcal{T}e^{i(\varphi_{sc}/2-\varphi_t)}\left[e^{-ip_l-i3\phi_0-i(\Phi_1-\Phi_2-\Phi_3+l_B^2 b_{2,x}b_{2,y})/2}\right.$$

$$\left. + e^{-i(p_k-p_l)-i3\phi_0-i(\Phi_2-\Phi_1-\Phi_3-l_B^2 b_{2,x}b_{2,y})/2} + e^{ip_k-i(\Phi_2+\Phi_1+\Phi_3)/2}\right]$$

$$+\mathcal{T}e^{i(\varphi_t-\varphi_{sc}/2)}\left[e^{ip_l+i3\phi_0+i(\Phi_1-\Phi_2-\Phi_3+l_B^2 b_{2,x}b_{2,y})/2}\right.$$

$$\left. + e^{i(p_k-p_l)+i3\phi_0+i(\Phi_2-\Phi_1-\Phi_3-l_B^2 b_{2,x}b_{2,y})/2} + e^{-ip_k+i(\Phi_2+\Phi_1+\Phi_3)/2}\right] = 0. \quad (5.97)$$

Numerical calculations show that for the particular case of Monkey saddle point $\varphi_{sc} = 2\varphi_t$. Using geometry of the problem (see Fig. 5.10), we note that the particular combinations of phases can be expressed via area enclosed by the orbit, $\Phi_1 + \Phi_2 - \Phi_3 = l_B^2 \mathcal{A}(E) = \pi p - 2\Phi_3$ and $\Phi_3 = 2F_1 = 6\phi_0$. In addition, we note that $l_B^2 b_{1,x}b_{2,y} = \pi p$. Thus, we obtain a final form of spectral equation:

$$\cos\left(l_B^2 \mathcal{A}(E)/2 - \varphi_{sc}/2\right) = \mathcal{T}\left[\cos\left(l_B^2[q_1 b_{2,y} - q_2 b_{2,x}] - \frac{\pi p}{2}\right)\right.$$
$$\left. + \cos\left(l_B^2[q_1 b_{2,y} + q_2(b_{1,x} - b_{2,x})] - \frac{\pi p}{2}\right) + \cos\left(l_B^2 q_2 b_{1,x} - \frac{\pi p}{2}\right)\right]. \quad (5.98)$$

These spectral equations appears in the main text. For the sake of completeness, we present a difference in spectral structure with even and odd flux denominator values p in Fig. 5.11. As seen from the plots, for even $p = 200$ spectrum is symmetric, while for odd $p = 201$ spectrum is antisymmetric with momentum. The analytic predictions and numerical tight binding simulations demonstrate excellent agreement.
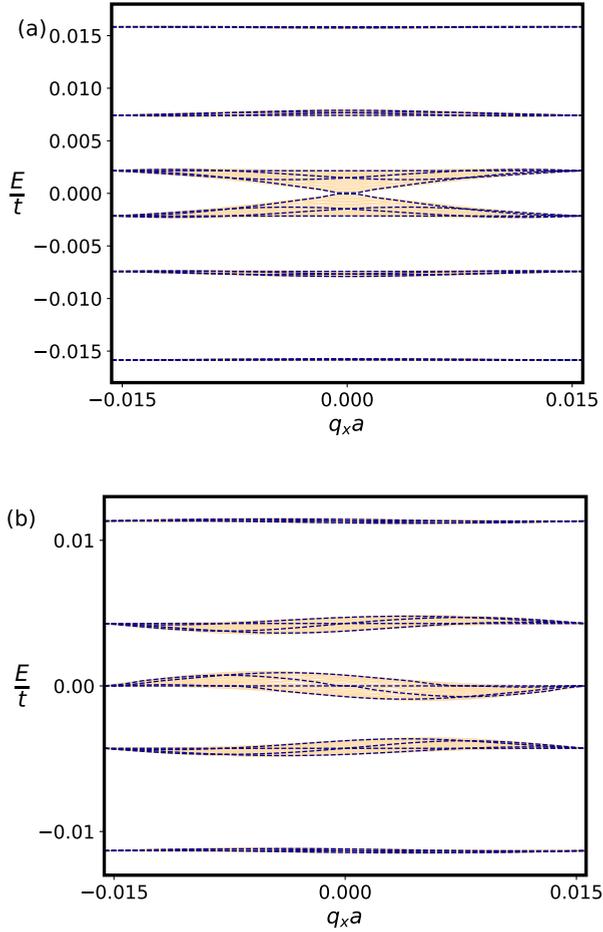
Figure 5.11. Two panels demonstrate comparison of analytic predictions (blue dashed lines) and numerical tight-binding simulations (orange solid lines merging into shaded areas) for the flux $\Phi = \frac{1}{p} \frac{h}{e}$ with (a) even $p = 200$ and (b) odd $p = 201$. The unit cell width of the ribbon with periodic boundary condition is taken to be $W = 20\sqrt{3}pa$.

Bibliography

[1] A. Altland and B. Simons, *Condensed Matter Field Theory* (Cambridge, 2023).

[2] L. D. Landau, *The Theory of a Fermi Liquid*, Sov. Phys. JETP. **3** 920 (1957).

[3] J. M. Luttinger, *An exactly soluble model of a many-fermion system*, J. Math. Phys. **4**, 1154 (1964).

[4] S. I. Tomonaga, *Remarks on Bloch's Method of Sound Waves applied to Many-Fermion Problems*, Progress of Theoretical Physics **5** 544 (1950).

[5] H. B. Nielsen and M. Ninomiya, *A no-go theorem for regularizing chiral fermions*, Phys. Lett. B **105**, 219 (1981).

[6] D. J. Thouless, M. Kohmoto, M. P. Nightingale and M. den Nijs, *Quantized Hall Conductance in a Two-Dimensional Periodic Potential*, Phys. Rev. Lett. **49**, 405 (1982).

[7] J. Maciejko, T. L. Hughes, and S.-C. Zhang, *The quantum spin Hall effect*, Annu. Rev. Condens. Matter Phys. **2**, 31 (2011).

[8] C. L. Kane and E. J. Mele, *Quantum spin Hall effect in graphene*, Phys. Rev. Lett. **95**, 226801 (2005).

[9] I. Bouchoule, R. Citro, T. Duty, T. Giamarchi, R. G. Hulet, M. Klanjsek, E. Orignac, B. Weber, *A glance to Luttinger liquid and its platforms*, arXiv:2501.12097.

[10] T. Senthil, *Symmetry-protected topological phases of quantum matter*, Annu. Rev. Condens. Matter Phys., **6**, 299 (2015).

[11] M. Barkeshli, Y. A. Chen, P. S. Hsin, and N. Manjunath, *Classification of (2+1)D invertible fermionic topological phases with symmetry* Phys. Rev. B **105**, 235143 (2022).

[12] J. Sullivan and M. Cheng, *Interacting edge states of fermionic symmetry-protected topological phases in two dimensions* SciPost Physics **9**, 016 (2020).

[13] T. Giamarchi, *Quantum Physics in One Dimension* (Oxford, 2003).

[14] J. von Delft and H. Schoeller, *Bosonization for beginners — refermionization for experts*, Ann. Physik **510**, 225 (1998).

[15] Z. Wang, F. Assaad, and M. Ulybyshev, *Validity of* SLAC *fermions for the* $(1 + 1)$-*dimensional helical Luttinger liquid*, Phys. Rev. B **108**, 045105 (2023).

[16] R. Stacey, *Eliminating lattice fermion doubling*, Phys. Rev. D **26**, 468 (1982).

[17] C. W. J. Beenakker, A. Donís Vela, G. Lemut, M. J. Pacholski, and J. Tworzydło, *Tangent fermions: Dirac or Majorana fermions on a lattice without fermion doubling*, Annalen der Physik **535**, 2300081 (2023).

[18] For an overview of methods to avoid fermion doubling in lattice gauge theory see: chapter 4 of David Tong's lecture notes: `https://www.damtp.cam.ac.uk/user/tong/gaugetheory.html`; chapter 4 of H. J. Rothe, *Lattice Gauge Theories: an introduction* (World Scientific, 2005).

[19] We are assuming a Hermitian operator. In a non-Hermitian system fermion doubling can be avoided, see M. N. Chernodub, *The Nielsen-Ninomiya theorem, PT-invariant non-Hermiticity and single 8-shaped Dirac cone*, J. Phys. A **50**, 385001 (2017).

[20] F. D. M. Haldane, *Luttinger liquid theory of one-dimensional quantum fluids*, J. Phys. C **14**, 2585 (1981).

[21] G. Giuliani and G. Vignale, *Quantum Theory of the Electron Liquid* (Cambridge, 2008).

[22] D. J. Scalapino and R. L. Sugar, *Method for performing Monte Carlo calculations for systems with fermions*, Phys. Rev. Lett. **46**, 519 (1981).

[23] J. E. Hirsch, *Discrete Hubbard-Stratonovich transformation for fermion lattice models*, Phys. Rev. B **28**, 4059 (1983).

[24] J. E. Hirsch and R. M. Fye, *Monte Carlo Method for Magnetic Impurities in Metals*, Phys. Rev. Lett. **56**, 2521 (1986).

[25] J. Gubernatis, N. Kawashima, and P. Werner, *Quantum Monte Carlo Methods: Algorithms for Lattice Models* (Cambridge, 2016).

[26] F. Becca and S. Sorella, *Quantum Monte Carlo Approaches for Correlated Systems* (Cambridge, 2017).

[27] D. B. Kaplan, *Chiral gauge theory at the boundary between topological phases*, Phys. Rev. Lett. **132**, 141603 (2024).

[28] D. B. Kaplan and S. Sen, *Weyl fermions on a finite lattice*, Phys. Rev. Lett. **132**, 141604 (2024).

[29] M. Hohenadler, T. C. Lang, and F. F. Assaad, *Correlation effects in quantum spin-Hall insulators: A quantum Monte Carlo study*, Phys. Rev. Lett. **106**, 100403 (2011).

[30] Shun-Li Yu, X. C. Xie, and Jian-Xin Li, *Mott physics and topological phase transition in correlated Dirac fermions*, Phys. Rev. Lett. **107**, 010401 (2011).

[31] Dong Zheng, Guang-Ming Zhang, and Congjun Wu, *Particle-hole symmetry and interaction effects in the Kane-Mele-Hubbard model*, Phys. Rev. B **84**, 205121 (2011).

[32] Y. Yamaji and M. Imada, *Mott physics on helical edges of two-dimensional topological insulators*, Phys. Rev. B **83**, 205122 (2011).

[33] In the context of lattice gauge theory, the spatial separation of fermion species is known as the method of domain wall or overlap fermions, see T. Kimura, *Domain-wall, overlap, and topological insulators*, arXiv:1511.08286.

[34] M. Hohenadler and F. F. Assaad, *Luttinger liquid physics and spin-flip scattering on helical edges*, Phys. Rev. B **85**, 081106(R) (2012).

[35] S. D. Drell, M. Weinstein, and S. Yankielowicz, *Strong-coupling field theories. II. Fermions and gauge fields on a lattice*, Phys. Rev. D **14**, 1627 (1976).

[36] Yuan Da Liao, Xiao Yan Xu, Zi Yang Meng, and Yang Qi, *Caution on Gross-Neveu criticality with a single Dirac cone: Violation of locality and its consequence of unexpected finite-temperature transition*, Phys. Rev. B **108**, 195112 (2023).

[37] L. Alvarez-Gaumé, G. Moore, P. Nelson, C. Vafa, and J. B. Bost, *Bosonization in arbitrary genus*, Phys. Lett. B **178**, 41 (1986).

[38] E. Berkowitz, A. Cherman, and T. Jacobson, *Exact lattice chiral symmetry in 2d gauge theory*, arXiv:2310.17539.

[39] F. D. M. Haldane, *Demonstration of the "Luttinger liquid" character of Bethe-Ansatz-soluble models of 1-D quantum fluids*, Phys. Lett. **81**A, 153 (1981).

[40] F. C. Alcaraz and Y. Hatsugai, *String correlation functions in the anisotropic spin-1 Heisenberg chain*, Phys. Rev. B **46**, 13914 (1992).

[41] A. Urichuk, J. Sirker, and A. Klümper, *Analytical results for the low-temperature Drude weight of the XXZ spin chain*, Phys. Rev. B **103**, 245108 (2021).

[42] C. M. Bender, K. A. Milton, and D. H. Sharp, *Consistent formulation of fermions on a Minkowski lattice*, Phys. Rev. Lett. **51**, 1815 (1983).

[43] J. Tworzydło, C. W. Groth, and C. W. J. Beenakker, *Finite difference method for transport properties of massless Dirac fermions*, Phys. Rev. B **78**, 235438 (2008).

[44] M. J. Pacholski, G. Lemut, J. Tworzydło, and C. W. J. Beenakker, *Generalized eigenproblem without fermion doubling for Dirac fermions on a lattice*, SciPost Phys. **11**, 105 (2021).

[45] A. Donís Vela, M. J. Pacholski, G. Lemut, J. Tworzydło, and C. W. J. Beenakker, *Massless Dirac fermions on a space-time lattice with a topologically protected Dirac cone*, Ann. Physik **534**, 2200206 (2022).

[46] J.-C. Budich, Ying Hu, and P. Zoller, *Helical Floquet channels in 1D lattices*, Phys. Rev. Lett. **118**, 105302 (2017).

[47] Xiao-Qi Sun, Meng Xiao, T. Bzdušek, Shou-Cheng Zhang, and Shanhui Fan, *Three-dimensional chiral lattice fermion in Floquet systems*, Phys. Rev. Lett. **121**, 196401 (2018).

[48] G. D. Mahan, *Many-Particle Physics* (Springer, New York, 2000).

[49] J. Ferrer, J. González, and M.-A. Martín-Delgado, *Bosonization on a lattice: The emergence of the higher harmonics*, Phys. Rev. B **51**, 4807 (1995).

[50] In the Appendices we derive the Euclidean action in the tangent discretization; we give details of the quantum Monte Carlo calculation, in particular the check that no sign problem appears; we provide the finite-size corrections to the power law decay of the correlators, following from the bosonization theory [14]. Our computer codes are provided in a Zenodo repository at `https://doi.org/10.5281/zenodo.10566063`.

[51] C. W. J. Beenakker, *Topologically protected Casimir effect for lattice fermions*, Phys. Rev. Res. **6**, 023058 (2024).

[52] J. Haegeman, L. Lootens, Q. Mortier, A. Stottmeister, A. Ueda, and F. Verstraete, *Interacting chiral fermions on the lattice with matrix product operator norms*, arXiv:2405.10285.

[53] X. S. Li, *An overview of SuperLU: Algorithms, implementation, and user interface, ACM Transactions on Mathematical Software*, **31**, 302 (2005).

[54] C.-K. Chiu, J. C. Y. Teo, A. P. Schnyder, and S. Ryu, *Classification of topological quantum matter with symmetries*, Rev. Mod. Phys. **88**, 035005 (2016).

[55] S. R. White, *Density matrix formulation for quantum renormalization groups*, Phys. Rev. Lett. **69**, 2863 (1992).

[56] S. Östlund and S. Rommer, *Thermodynamic limit of density matrix renormalization*, Phys. Rev. Lett. **75**, 3537 (1995).

[57] U. Schollwöck, *The density-matrix renormalization group in the age of matrix product states*, Annals Physics **326**, 96 (2011).

[58] J. I. Cirac, D. Pérez-García, N. Schuch and F. Verstraete, *Matrix product states and projected entangled pair states: Concepts, symmetries, theorems*, Rev. Mod. Phys. **93**, 045003 (2021).

[59] V. A. Zakharov, J. Tworzydło, C. W. J. Beenakker, and M. J. Pacholski, *Helical Luttinger liquid on a space-time lattice*, Phys. Rev. Lett. **133**, 116501 (2024).

[60] F. Verstraete, J. J. Garcia-Ripoll, J. I. Cirac, *Matrix product density operators: Simulation of finite-temperature and dissipative systems*, Phys. Rev. Lett. **93**, 207204 (2004).

[61] M. Zwolak and G. Vidal, *Mixed-state dynamics in one-dimensional quantum lattice systems: A time-dependent superoperator renormalization algorithm*, Phys. Rev. Lett. **93**, 207205 (2004).

[62] I. P. McCulloch, *Infinite size density matrix renormalization group, revisited*, arXiv:0804.2509

[63] G. M. Crosswhite, A. C. Doherty and G. Vidal, *Applying matrix product operators to model systems with long-range interactions*, Phys. Rev. B **78**, 035116 (2008).

[64] B. Pirvu, V. Murg, J. I. Cirac and F. Verstraete, *Matrix product operator representations*, New J. Phys. **12**, 025012 (2010).

[65] F. Fröwis, V. Nebendahl, and W. Dür, *Tensor operators: constructions and applications for long-range interaction systems*, Phys. Rev. A **81**, 062337 (2010).

[66] J. Hauschild and F. Pollmann *Efficient numerical simulations with Tensor Networks: Tensor Network Python (TeNPy)*, SciPost Phys. Lect. Notes **5** (2018).

[67] Meng Zeng, Zheng Zhu, Juven Wang, and Yi-Zhuang You, *Symmetric mass generation in the 1+1 dimensional chiral fermion 3-4-5-0 model*, Phys. Rev. Lett. **128**, 185301 (2022).

[68] F. Verstraete and I. Cirac, *Matrix product states represent ground states faithfully*, Phys. Rev. B **73**, 094423 (2006).

[69] C. Kallin and J. Berlinsky, *Chiral superconductors*, Rep. Prog. Phys. **79**, 054502 (2016).

[70] T. Senthil and M. P. A. Fisher, *Quasiparticle localization in superconductors with spin-orbit scattering*, Phys. Rev. B **61**, 9690 (2000).

[71] F. Evers and A. D. Mirlin, *Anderson transitions*, Rev. Mod. Phys. **80**, 1355 (2008).

[72] C. W. J. Beenakker and L. P. Kouwenhoven, *A road to reality with topological superconductors*, Nature Phys. **12**, 618 (2016).

[73] J. T. Chalker, N. Read, V. Kagalovsky, B. Horovitz, Y. Avishai, and A. W. W. Ludwig, *Thermal metal in network models of a disordered two-dimensional superconductor*, Phys. Rev. B **65**, 012506 (2001).

[74] A. Mildenberger, F. Evers, A.D. Mirlin, and J. T. Chalker, *Density of quasiparticle states for a two-dimensional disordered system: Metallic, insulating, and critical behavior in the class-D thermal quantum Hall effect*, Phys. Rev. B **75**, 245321 (2007).

[75] M. Wimmer, A. R. Akhmerov, M. V. Medvedyeva, J. Tworzydło, and C. W. J. Beenakker, *Majorana bound states without vortices in topological superconductors with electrostatic defects*, Phys. Rev. Lett. **105**, 046803 (2010).

[76] V. Kagalovsky and D. Nemirovsky, *Critical fixed points in class D superconductors*, Phys. Rev. B **81**, 033406 (2010).

[77] M. V. Medvedyeva, J. Tworzydło, and C. W. J. Beenakker, *Effective mass and tricritical point for lattice fermions localized by a random mass*, Phys. Rev. B **81**, 214203 (2010).

[78] C. R. Laumann, A. W. W. Ludwig, D. A. Huse, and S. Trebst, *Disorder-induced Majorana metal in interacting non-Abelian anyon systems*, Phys. Rev. B **85**, 161301(R) (2012).

[79] B. Pekerten, A. Mert Bozkurt, and I. Adagideli, *Fermion parity switches of the ground state of Majorana billiards*, Phys. Rev. B **100**, 235455 (2019).

[80] T. Wang, Z. Pan, T. Ohtsuki, I. A. Gruzberg, and R. Shindou, *Multicriticality of two-dimensional class-D disordered topological superconductors*, Phys. Rev. B **104**, 184201 (2021).

[81] C. Caroli, P.-G. de Gennes, and J. Matricon, *Bound fermion states on a vortex line in a type II superconductor*, J. Phys. Lett. **9**, 307 (1964).

[82] G. E. Volovik, *Fermion zero modes on vortices in chiral superconductors*, JETP Lett. **70** , 609 (1999).

[83] N. Read and D. Green, *Paired states of fermions in two dimensions with breaking of parity and time-reversal symmetries, and the fractional quantum Hall effect*, Phys. Rev. B **61**, 10267 (2000).

[84] C. W. J. Beenakker, *Search for Majorana fermions in superconductors*, Annu. Rev. Con. Mat. Phys. **4**, 113 (2013).

[85] R. M. Lutchyn, E. P. A. M. Bakkers, L. P. Kouwenhoven, P. Krogstrup, C. M. Marcus, and Y. Oreg, *Majorana zero modes in superconductor–semiconductor heterostructures*, Nature Rev. Materials **3**, 52 (2018).

[86] K. Flensberg, F. von Oppen, and A. Stern, *Engineered platforms for topological superconductivity and Majorana zero modes*, Nature Rev. Materials **6**, 944 (2021).

[87] T. A. Loring, *K-theory and pseudospectra for topological insulators*, Annals Physics **356**, 383 (2015).

[88] I. C. Fulga, D. I. Pikulin, and T. A. Loring, *Aperiodic weak topological superconductors*, Phys. Rev. Lett. **116**, 257002 (2016).

[89] T. Loring and H. Schulz-Baldes, *Finite volume calculation of K-theory invariants*, New York J. Math. **22**, 1111 (2017).

[90] E. Lozano Viesca, J. Schober, and H. Schulz-Baldes, *Chern numbers as half-signature of the spectral localizer*, J. Math. Phys. **60**, 072101 (2019).

[91] T. Loring and H. Schulz-Baldes, *The spectral localizer for even index pairings*, J. Noncommutative Geometry **14**, 1 (2020).

[92] A. Cerjan and T. A. Loring, *Local invariants identify topology in metals and gapless systems*, Phys. Rev. B **106**, 064109 (2022).

[93] H. Schulz-Baldes, *Topological indices in condensed matter*, arXiv:2403.18948.

[94] N. Doll, T. Loring, and H. Schulz-Baldes, *Local topology for periodic Hamiltonians and fuzzy tori*, arXiv:2403.18931.

[95] S. Franca and A. G. Grushin, *Topological zero-modes of the spectral localizer of trivial metals*, Phys. Rev. B **109**, 195107 (2024).

[96] Zihao Qi, Ilyoun Na, Gil Refael, and Yang Peng, *Real-space topological invariant for time-quasiperiodic Majoranas*, Phys. Rev. B **110**, 014309 (2024).

[97] G. E. Volovik, *Topology of a ^{3}He-A film on a corrugated graphene substrate*, JETP Lett. **107**, 115 (2018).

[98] A. Altland and M. R. Zirnbauer, *Nonstandard symmetry classes in mesoscopic normal-superconducting hybrid structures*, Phys. Rev. B **55**, 1142 (1997).

[99] C. W. Groth, M. Wimmer, A. R. Akhmerov, and X. Waintal, *Kwant: A software package for quantum transport*, New J. Phys. **16**, 063065 (2014).

[100] G. Lemut, M. J. Pacholski, O. Ovdat, A. Grabsch, J. Tworzydło, and C. W. J. Beenakker, *Localization landscape for Dirac fermions*, Phys. Rev. B **101**, 081405(R) (2020).

[101] L. Herviou and J. H. Bardarson, $\mathcal{L}^2$ *localization landscape for highly excited states*, Phys. Rev. B **101**, 220201(R) (2020).

[102] M. Filoche and S. Mayboroda, *Universal mechanism for Anderson and weak localization*, Proc. Natl Acad. Sci. USA **109**, 14761 (2012).

[103] D. N. Arnold, G. David, D. Jerison, S. Mayboroda, and M. Filoche, *Effective confining potential of quantum states in disordered media*, Phys. Rev. Lett. **116**, 056602 (2016).

[104] M. Filoche, M. Piccardo, Y.-R. Wu, C.-K. Li, C. Weisbuch, and S. Mayboroda, *Localization landscape theory of disorder in semiconductors*, Phys. Rev. B **95**, 144204 (2017).

[105] M. Filoche, P. Pelletier, D. Delande, and S. Mayboroda, *Anderson mobility edge as a percolation transition*, Phys. Rev. B **109**, L220202 (2024).

[106] The simulation code for the spectral localizer calculations is available in the Zenodo repository at `https://doi.org/10.5281/zenodo.14782907`.

[107] L. Van Hove, *The occurrence of singularities in the elastic frequency distribution of a crystal*, Physical Review **89**, 1189 (1953).

[108] N. F. Q. Yuan, H. Isobe, and L. Fu, *Magic of high-order van Hove singularity*, Nature Communications **10**, 5769 (2019).

[109] A. Chandrasekaran, A. Shtyk, J. J. Betouras, and C. Chamon, *Catastrophe theory classification of fermi surface topological transitions in two dimensions*, Phys. Rev. Research **2**, 013355 (2020).

[110] N. F. Q. Yuan and L. Fu, *Classification of critical points in energy bands based on topology, scaling, and symmetry*, Physical Review B **101**, 125120 (2020).

[111] A. B. Pippard, *Quantization of coupled orbits in metals*, Proceedings of the Royal Society of London. Series A. Mathematical and Physical Sciences **270**, 1 (1962).

[112] A. B. Pippard, *Quantization of coupled orbits in metals II. the two-dimensional network, with special reference to the properties of zinc*, Philosophical Transactions of the Royal Society of London. Series A, Mathematical and Physical Sciences **256**, 317 (1964).

[113] A. B. Pippard, *Magnetic breakdown in a dislocated lattice*, Proceedings of the Royal Society of London. Series A. Mathematical and Physical Sciences **287**, 165 (1965).

[114] W. G. Chambers, *Linear-network model for magnetic breakdown in two dimensions*, Physical Review **140**, A135 (1965).

[115] W. G. Chambers, *Magnetic breakdown: Effective Hamiltonian and de Haas-Van Alphen effect*, Phys. Rev. **149**, 493 (1966).

[116] W. G. Chambers, *Magnetic breakdown and oscillatory magnetoresistance by a Kubo formula*, Phys. Rev. **165**, 799 (1968).

[117] W. G. Chambers, *Oscillatory magnetoconductivity in a linear chain of orbits coupled by magnetic breakdown*, Journal of Physics F: Metal Physics **3**, 1216 (1973).

[118] H. J. Fischbeck, *Theory of Bloch electrons in a magnetic field*, Physica Status Solidi (b) **38**, 11 (1970).

[119] W. G. Chambers, *Linear-network model for magnetic breakdown in two dimensions*, Phys. Rev. **140**, A135 (1965).

[120] K. S. Novoselov, A. K. Geim, S. V. Morozov, D. Jiang, Y. Zhang, S. V. Dubonos, I. V. Grigorieva, and A. A. Firsov, *Electric field effect in atomically thin carbon films*, Science **306**, 666 (2004).

[121] K. S. Novoselov, D. Jiang, F. Schedin, T. J. Booth, V. V. Khotkevich, S. V. Morozov, and A. K. Geim, T*wo-dimensional atomic crystals*, Proceedings of the National Academy of Sciences **102**, 10451 (2005).

[122] K. S. Novoselov, A. Mishchenko, A. Carvalho, and A. H. Castro Neto, *2D materials and van der Waals heterostructures*, Science *353*, aac9439 (2016).

[123] S. Manzeli, D. Ovchinnikov, D. Pasquier, O. V. Yazyev, and A. Kis, *2D transition metal dichalcogenides*, Nature Reviews Materials **2**, 17033 (2017).

[124] S. M. G. Richard E. Prange, *The Quantum Hall Effect*, Springer New York, (1990).

[125] M. Y. Azbel, *Quasiclassical quantization in the neighborhood of singular classical trajectories*, Sov. Phys. JETP **12**, 891 (1961).

[126] M. Y. Azbel, *Energy spectrum of a conduction electron in a magnetic field*, Sov. Phys. JETP **19**, 634 (1964).

[127] A. Alexandradinata and L. Glazman, *Semiclassical theory of Landau levels and magnetic breakdown in topological metals*, Physical Review B **97**, 144422 (2018).

[128] B. Göbel, A. Mook, J. Henk, and I. Mertig, *Signatures of lattice geometry in quantum and topological Hall effect*, New Journal of Physics **19**, 063042 (2017).

[129] N. Paul, P. J. D. Crowley, T. Devakul, and L. Fu, *Moiré Landau fans and magic zeros*, Phys. Rev. Lett. **129**, 116804 (2022).

[130] G. Lemut, A. Donís Vela, M. J. Pacholski, J. Tworzydlo, and C. W. J. Beenakker, *Magnetic breakdown spectrum of a Kramers–Weyl semimetal*, New Journal of Physics **22**, 093022 (2020).

[131] C.-K. Lu and H. A. Fertig, *Magnetic breakdown in twisted bilayer graphene*, Physical Review B **89**, 085408 (2014).

[132] V. M. Gvozdikov and M. Taut, *Magnetic quantum oscillations of electrons on a two-dimensional lattice: Numerical simulations and the magnetic breakdown approach*, Phys. Rev. B **75**, 155436 (2007).

[133] A. Nikolaev and M. Zhuravlev, *Anomalous broadening of Landau levels at the saddle point energy of two dimensional square lattice*, Journal of Magnetism and Magnetic Materials **560**, 169674 (2022).

[134] A. V. Nikolaev, *Saddle point anomaly of Landau levels in graphene-like structures*, Physical Review B **104**, 035419 (2021).

[135] A. B. Pippard, *Experimental analysis of the electronic structure of metals*, Reports on Progress in Physics **23**, 176 (1960).

[136] I. M. Lifshitz and M. I. Kaganov, *Some problems of the electron theory of metals I. Classical and quantum mechanics of electrons in metals*, Soviet Physics Uspekhi **2**, 831 (1960).

[137] R. Stark and L. Falicov, *Magnetic breakdown in metals*, Progress in Low Temperature Physics **6**, 235 (1967).

[138] V. Zakharov, A. M. Bozkurt, A. R. Akhmerov, and D. O. Oriekhov, *Code for "Landau quantization near generalized van Hove singularities: magnetic breakdown and orbit networks"* 10.5281/zenodo.7707909 (2023).

[139] G. E. Zil'berman, *Behavior of an electron in a periodic electric and a uniform magnetic field*, Soviet Phys. JETP **5** (1957).

[140] C.-M. Ho and J. T. Chalker, *Models for the integer quantum Hall effect: The network model, the Dirac equation, and a tight-binding Hamiltonian*, Phys. Rev. B **54**, 8708 (1996).

[141] R. R. Gerhardts, D. Weiss, and K. v. Klitzing, *Novel magnetoresistance oscillations in a periodically modulated two-dimensional electron gas*, Physical Review Letters **62**, 1173 (1989).

[142] R. W. Winkler, J. P. Kotthaus, and K. Ploog, *Landau band conductivity in a two-dimensional electron system modulated by an artificial one-dimensional superlattice potential*, Physical Review Letters **62**, 1177 (1989).

[143] C. W. J. Beenakker, *Guiding-center-drift resonance in a periodically modulated two-dimensional electron gas*, Physical Review Letters **62**, 2020 (1989).

[144] P. Streda and A. H. MacDonald, *Magnetic breakdown and magnetoresistance oscillations in a periodically modulated two-dimensional electron gas*, Physical Review B **41**, 11892 (1990).

[145] V. M. Gvozdikov, *Magnetoresistance oscillations in a periodically modulated two-dimensional electron gas: The magnetic-breakdown approach*, Physical Review B **75**, 115106 (2007).

[146] J. Finney, A. L. Sharpe, E. J. Fox, C. L. Hsueh, D. E. Parker, M. Yankowitz, S. Chen, K. Watanabe, T. Taniguchi, C. R. Dean, A. Vishwanath, M. A. Kastner, and D. Goldhaber-Gordon, *Unusual magnetotransport in twisted bilayer graphene*, Proceedings of the National Academy of Sciences **119**, 119 (2022).

[147] P. Rosenzweig, H. Karakachian, D. Marchenko, K. Küster, and U. Starke, *Overdoping graphene beyond the Van Hove singularity*, Phys. Rev. Lett. **125**, 176403 (2020).

[148] M. R. Slot, T. S. Gardenier, P. H. Jacobse, G. C. P. van Miert, S. N. Kempkes, S. J. M. Zevenhuizen, C. M. Smith, D. Vanmaekelbergh, and I. Swart, *Experimental realization and characterization of an electronic Lieb lattice*, Nature Physics **13**, 672 (2017).

[149] K. Kim, A. DaSilva, S. Huang, B. Fallahazad, S. Larentis, T. Taniguchi, K. Watanabe, B. J. LeRoy, A. H. MacDonald, and E. Tutuc, *Tunable moiré bands and strong correlations in small-twist-angle bilayer graphene*, Proceedings of the National Academy of Sciences **114**, 3364 (2017).

[150] Y. Cao, V. Fatemi, S. Fang, K. Watanabe, T. Taniguchi, E. Kaxiras, and P. Jarillo-Herrero, *Unconventional superconductivity in magic-angle graphene superlattices*, Nature **556**, 43 (2018).

[151] Y. Kim, P. Moon, K. Watanabe, T. Taniguchi, and J. H. Smet, *Odd integer quantum Hall states with interlayer coherence in twisted bilayer graphene*, Nano Letters **21**, 4249 (2021).

[152] Y.-T. Hsu, F. Wu, and S. Das Sarma, *Spin-valley locked instabilities in moiré transition metal dichalcogenides with conventional and higher-order Van Hove singularities*, Phys. Rev. B **104**, 195134 (2021).

[153] E. Y. Andrei, G. Li, and X. Du, *Electronic properties of graphene: a perspective from scanning tunneling microscopy and magnetotransport*, Reports on Progress in Physics **75**, 056501 (2012).

[154] Y. Xie, B. Lian, B. Jäck, X. Liu, C.-L. Chiu, K. Watanabe, T. Taniguchi, B. A. Bernevig, and A. Yazdani, *Spectroscopic signatures of many-body correlations in magicangle twisted bilayer graphene*, Nature **572**, 101 (2019).

[155] Xinloong Han, Andreas P. Schnyder and Xianxin Wu, *Enhanced nematicity emerging from higher-order Van Hove singularities*, Phys. Rev. B **107**, 184504 (2023)

Summary

Understanding interactions in quantum many-body systems remains one of the most profound and difficult challenges in condensed matter physics. While free particle systems can be solved through single-particle techniques, the introduction of interactions turns the problem essentially many-body and quickly intractable. The Hilbert space grows exponentially, and traditional approaches become useless.

To deal with this, one typically turns to numerical methods by discretizing the system on a lattice. This approach generally works well for many 1D problems, including those described by Schrödinger equation. However, when it comes to massless Dirac fermions with protected chirality, the situation becomes more complicated. Any naive discretization inevitably runs into the fermion doubling problem, formalized by the Nielsen–Ninomiya theorem, which forbids a straightforward lattice realization of a single chiral mode without either breaking symmetry or introducing unphysical degrees of freedom.

My thesis is motivated by this problem: the need to describe 1D interacting systems, and the difficulty of doing so numerically due to these fundamental obstacles. The main focus of this work is to develop and explore lattice-based numerical methods for strongly correlated chiral fermions in one dimension, with the Luttinger liquid as a central case study.

The first part of the thesis introduces and validates a novel numerical approach based on tangent fermions. In Chapter 2 we use its local action formulation in the discretized space-time, allowing for simulations via quantum Monte Carlo that are sign-problem-free at half-filling. It successfully reproduces continuum results for the helical Luttinger liquid without adjustable parameters, marking the first faithful lattice simulation of this system.

Building on that, Chapter 3 extends the tangent fermion approach to tensor network methods, particularly DMRG. This allows us to move beyond the limitations of QMC and investigate broader settings, inclusive of static potentials and non-trivial interactions, away of half-filling. We show that tangent fermions sup-

port a compact and efficient tensor network representation, accurately matching the bosonization results of the Luttinger liquid. This confirms the versatility and consistency of the method.

The second half of the thesis shifts focus to two-dimensional single-particle physics, tackling two distinct problems. Chapter 4 concerns Majorana thermal metals in disordered chiral superconductors. We use the spectral localizer, as real-space topological tools landscape function, to show that the metal–insulator transition proceeds through percolation of topological domain walls.

Finally, Chapter 5 investigates Landau quantization in systems with generalized Van Hove singularities. We develop a general method for computing magnetic breakdown in these materials, uncovering how coherent orbit networks can form minibands that enable bulk conductance under a magnetic field — potentially exceeding edge channel transport. These features offer experimentally testable signatures linked to the underlying saddle-point structure.

Samenvatting

Het begrijpen van wisselwerkingen in quantum-veeldeeltjessystemen blijft een van de diepgaandste en moeilijkste uitdagingen in de theorie van de geconden- seerde materie. Terwijl systemen zonder wisselwerkingen met één-deeltjesmethodes exact kunnen worden opgelost, maakt de introductie van interacties het probleem snel onhandelbaar. De Hilbertruimte groeit exponentieel, buiten het bereik van exacte methodes.

Om dit aan te pakken, grijpt men meestal naar numerieke methodes door het systeem op een rooster te discretiseren. Deze aanpak werkt over het algemeen goed voor één-dimensionale problemen, waaronder de problemen die worden beschreven door de Schrödinger-vergelijking. De Dirac-vergelijking voor relati- vistische, massaloze deeltjes is ingewikkelder. Een naïeve discretisatie stuit op het probleem van fermion-duplicatie, geformaliseerd in de Nielsen-Ninomiya- stelling, die in de weg staat van een discretisatie die de fundamentele symmetrie van het probleem behoudt.

Het eerste deel van mijn proefschrift is gemotiveerd door dit probleem: de noodzaak om één-dimensionale, sterk wisselwerkende systemen numeriek te beschrijven en de moeilijkheid om dit op een rooster te doen in het geval van massaloze relativistische deeltjes. Het Luttinger-model is een paradigma voor dit probleem en staat centraal in het proefschrift.

We introduceren en valideren een nieuwe numerieke aanpak gebaseerd op tangens-fermionen (zo genaamd omdat de dispersie-relatie door een tangens beschreven wordt). In Hoofdstuk 2 discretiseren we ruimte en tijd in het quantum Monte Carlo algorithme. Voor het eerst slagen we er zo in om het Luttinger- model op een rooster uit te rekenen, met resultaten die goed overeenkomen met de bestaande bosonisatie theorie in het continuum.

In Hoofdstuk 3 wordt de tangens-fermion aanpak uitgebreid naar tensor- netwerk-methoden. Dit stelt ons in staat de beperkingen van quantum Monte Carlo te overstijgen en meer algemene situaties te onderzoeken. We tonen aan dat tangens-fermionen een compacte en efficiënte tensor-netwerkrepresentatie

ondersteunen, die de bosonisatie-resultaten van de Luttinger-model nauwkeurig benaderen. Dit bevestigt de veelzijdigheid en consistentie van de methode.

Het tweede deel van het proefschrift heeft een ander thema, het richt zich op twee-dimensionale systemen zonder sterke wisselwerkingen. Hoofdstuk 4 behandelt de metaal-isolator overgang in supergeleiders met Majorana deeltjes. We tonen aan dat deze overgang verloopt via de percolatie van topologische domeinwanden.

Tenslotte onderzoekt hoofdstuk 5 de Landau-quantisatie in systemen met generaliseerde Van Hove-singulariteiten. We ontwikkelen een algemene methode om magnetische breakdown in deze materialen te berekenen en ontdekken hoe coherente netwerken minibanden kunnen vormen die bulkgeleiding onder een magnetisch veld mogelijk maken — soms zelfs sterker dan de randgeleiding. Deze kenmerken bieden experimenteel toetsbare effecten die gekoppeld zijn aan de onderliggende zadelpuntenstructuur.

Резюме

Описание взаимодействий в квантовых многочастичных системах оста-
ётся одной из самых глубоких и сложных задач физики конденсиро-
ванного состояния. Если проблему системы свободных частиц мож-
но решить с помощью одночастичных методов, то добавление взаимо-
действий делает задачу поистине многочастичной и быстро неразре-
шимой. Размер гильбертова пространства растёт экспоненциально, и
стандартные подходы становятся неприменимыми.

Обычно, для решение таких задач, прибегают к численным мето-
дам, дискретизируя систему на решётке. Такой подход хорошо рабо-
тает для многих одномерных задач, в том числе описываемых уравне-
нием Шрёдингера. Однако, при рассмотрении проблемы безмассовых
фермионов Дирака с защищённой хиральностью, ситуация усложняет-
ся. Любой прямолиный метод дискретизации неизбежно сталкивается
с проблемой удвоения фермионов, которая была формально описанна
теоремой Нильсена—Ниномии, запрещающей локальную реализацию
одного хирального фермиона на пространственной решётке без нару-
шения симметрии или введения нефизических степеней свободы.

Главная мотивация моей диссертации заключается в необходимости
описания одномерных сильно коррелированных систем и сложности
реализации численного подхода, вызванной фундаментальными огра-
ничениями. Основной фокус этой работы – это разработка и исследо-
вание численных методов на решётке для сильно взаимодействующих
одномерных хиральных фермионов, с жидкостью Латтинджера, вы-
ступающей в качестве основного примера.

В первой части диссертации выдвигается и валидируется новый
численный подход, основанный на тангенсных фермионах. Во второй
главе мы используем его в форме локального евклидова действия на
дискретном пространстве-времени, что позволяет нам применить ме-
тод квантового Монте-Карло (QMC) без проблемы знака при усло-

вии наполовину заполненной зоны. Этот метод точно воспроизводит результаты континуальной теории для геликальной жидкости Латтинджера без подгоночных параметров и представляет собой первую успешную численную реализацию этой системы на решетке.

В третьей главе мы расширяем подход тангенсных фермионов на методы тензорных сетей, в частности DMRG. Что позволяет нам преодолеть ограничения QMC и исследовать более общие ситуации, с наличием потенциального поля и нестандартных взаимодействий, в том числе вне половинного заполнения. Продемонстрированно, что тангенсные фермионы допускают компактное и эффективное представление в терминах тензорных сетей, и хорошо согласуются с результатами бозонизации жидкости Латтинджера. Это подтверждает универсальность и согласованность нашего метода.

Во второй части диссертации фокус иследовательской работы смещается на двумерную одночастичную физику, охватывая два различных направления. Глава 4 посвящена тепловым Майорана-металлам в беспорядочных хиральных сверхпроводниках. Мы применяем спектральный локализатор как инструмент топологического ландшафта в координатном пространстве и показываем, что переход в металл из изолятора происходит в следствие перколяции границ топологических доменов.

Наконец, Глава 5 исследует квантование Ландау в системах с обобщёнными особенностями Ван Хова. Мы разрабатываем общий метод расчёта магнитного пробоя в таких материалах и показываем, как когерентные орбитальные сети формируют минизоны, которые обеспечивают объёмную проводимость в магнитном поле — порой даже превышающую краевую. Эти особенности позволяют установить экспериментально различимые сигналы, связанные со структурой седловых точек в зоне Бриллюэна.

Curriculum Vitæ

I was born on the 11th of August in Saint Petersburg, Russia, where I spent my entire childhood and adolescence, and first emerged as an independent adult. During that time, I studied and successfully graduated from Physics and Mathematics Lyceum №366, completing my general education there between 2004 and 2015. I fell in love with physics when I was first introduced to it in the 7th grade by my teacher Aleksey V. Stepanov. My passion for it remained strong throughout my school years. I participated in several physics competitions, reaching the regional finals as my highest achievement. Driven by my dream of becoming a physicist, I passed the national exam in physics with the highest possible grade, which allowed me to be successfully admitted to Saint Petersburg Academic University in 2015.

At Academic University, I enrolled in a novel bachelor's program in physics that had been launched just a year prior to my admission. The program was designed for a small amount of 30 students and was taught by highly professional researchers from various academic institutions in Saint Petersburg. I chose to specialise in theoretical physics and applied for a bachelor's thesis project in the Sector of Theory of Quantum Coherent Phenomena in Solids at the Ioffe Institute. After passing the admission exams to join the group, I began working under the supervision of Alexander N. Poddubny, which led to my first scientific publication two years later. I graduated from Academic University in 2019 with honors (cum laude). Unfortunately, shortly after my graduation, both the university in general and the bachelor's program in physics in particular collapsed and ceased to exist in their original form.

I continued my studies in theoretical physics at Skoltech, a newly established international technological university in Moscow. After passing the admission exams, I was accepted into the Theoretical Physics program, curated by researchers from the Department of Quantum Microscopic Theory at the Landau Institute. At Skoltech, I further advanced my technical skills in theoretical physics and continued the research work. I completed my Master's thesis under the supervision of Igor S. Burmistrov and graduated in 2021 cum laude. Sadly, a year after my

graduation, the Theoretical Physics program at Skoltech was closed.

Pursuing my goal of becoming a theoretical physicist, I obtained a Ph.D. position in 2021 in the group of Carlo Beenakker at the Lorentz Institute of Leiden University. During my Ph.D., I was given the freedom of working on topics and participating in projects, that I found interesting. This allowed me to explore a few research directions and collaborate with several research groups, including Quantum Tinkerer at TU Delft, the Applied Quantum Algorithms (aQa) group at Leiden University, and the group of Frank Verstraete at Ghent University. I have participated in many schools and several conferences, continuously learning new aspects of theoretical physics and presenting my own work.

After finishing my Ph.D., I will stay in the group of Carlo Beenakker as a postdoctoral researcher, where I will continue working on topological and strongly correlated matter.

List of Publications

[1] V. A. Zakharov and A. N. Poddubny, *Transverse magneto-optical Kerr effect enhanced at the bound states in the continuum*, Physical Review A **101**, 043848 (2020).

[2] V. A. Zakharov and I. S. Burmistrov, *Residual bulk viscosity of a disordered two-dimensional electron gas*, Physical Review B **103**, 235305 (2021).

[3] V. A. Zakharov, A. M. Bozkurt, A. R. Akhmerov and D. O. Oriekhov, *Landau quantization near generalized Van Hove singularities: Magnetic breakdown and orbit networks*, Physical Review B **109**, L081103 (2024).
[Chapter 5 is based on this publication.]

[4] V. A. Zakharov, J. Tworzydło, C. W. J. Beenakker and M. J. Pacholski, Physical Review Letters **133**, 116501 (2024).
[Chapter 2 is based on this publication.]

[5] V. A. Zakharov, S. Polla, A. Donís Vela, P. Emonts, M. J. Pacholski, J. Tworzydło, and C. W. J. Beenakker, *Luttinger liquid tensor network: Sine versus tangent dispersion of massless Dirac fermions* Physical Review Research **6**, 043059 (2024).
[Chapter 3 is based on this publication.]

[6] V. A. Zakharov, I. C. Fulga, G. Lemut, J. Tworzydło, C. W. J. Beenakker, *Majorana-metal transition in a disordered superconductor: percolation in a landscape of topological domain walls* , New Journal of Physics **27**, 033002 (2025).
[Chapter 4 is based on this publication.]

[7] C. W. J. Beenakker and V. A. Zakharov, *Bimodal distribution of delay times and splitting of the zero-bias conductance peak in a double-barrier normal-superconductor junction*, arXiv:2506.18515 (2025).